Numerical Study on Unstable Combustion: Combustion Instability and Combustion Noise

Jun Nagao

Numerical Study on Unstable Combustion: Combustion Instability and Combustion Noise

Jun Nagao

A thesis submitted to Kyoto University
for the degree of Doctor of Philosophy in Engineering

2024

Acknowledgments

The research described in this thesis was carried out in the Department of Mechanical Engineering and Science at Kyoto University Graduate School of Engineering under the supervision of Professor Ryoichi Kurose. The author would like to express his most heartfelt gratitude to the professor for all the helpful suggestions for his study and constant encouragement.

The author gives his thanks to Professor Koji Nagata and Professor Hiroshi Iwai for their valuable and critical comments on his study.

The author shows his appreciation to Associate Professor Mitsuhiro Matsumoto, Assistant Professor Abhishek Lashman Pillai, and Assistant Professor Hidenobu Wakabayashi from the bottom of his heart for many useful discussions and comments on his research, and for the top-notch education.

The author is grateful to Dr. Shigeru Tachibana and Dr. Takeshi Shoji of Japan Aerospace Exploration Agency (JAXA) for many useful discussions.

The author feels grateful to Professor Takeshi Yokomori of Keio University for the helpful suggestions.

The author deeply appreciates Mr. Hideyo Negishi of Japan Aerospace Exploration Agency (JAXA)'s wonderful advice on life and research planning.

The author thanks Dr. Reo Kai and the past and present members of the Thermal Science and Engineering Laboratory.

This work was partially supported by MEXT as "Program for Promoting Researches on the Supercomputer Fugaku" (Digital Twins of Real World's Clean Energy Systems with Integrated Utilization of Super-simulation and AI) (Development of the Smart de-

sign system on the supercomputer “Fugaku” in the era of Society 5.0) and by JSPS KAKENHI Grant Number 19H02076, 22H00192.

Finally, the author would like to express the deepest appreciation to his parents for their infinite support and constant affection.

Contents

Chapter 1

Introduction

1.1 Background and purpose of this study

Combustion is a redox reaction involving fuels and oxidants that continuously yields heat energy from chemical energy. For this reason, combustion has been used as a source of light and heat since ancient times. In modern times, it is still used in propulsion systems and as a source of electrical energy owing to the easy acquisition and storage of fuel and the ability to obtain vast amounts of energy in a short period of time. However, CO_2 and NOx produced during combustion are considered to cause global warming and air pollution, and solutions to these problems are urgent issues to be addressed.

CO_2 emissions from fossil fuels and industrial sources are estimated to account for 65 % of global greenhouse gas emissions, and among these, power generation, transportation, and industry account for 60 % of global greenhouse gas emissions [1]. Among these applications, gas turbines have achieved high system efficiency by using a combined cycle that increases the temperature and pressure of the incoming air [2, 3] and utilizes high-temperature waste heat gas energy. Furthermore, through the development of advanced capturing technologies for CO_2, emissions have been reduced [4]. In addition to these technological developments, hydrogen and ammonia are attracting attention as next-generation fuels. Since these fuels do not contain carbon in their composition, they do not emit CO_2 during combustion and are expected to reduce CO_2 emissions further.

NOx is also emitted into the atmosphere, causing respiratory problems in humans and acid rain and coastal water pollution when dissolved in atmospheric moisture. NOx can be produced by various natural phenomena such as volcanic eruptions [5], thunder [6], and emissions from soils [7]. However, these natural sources are minimal, and most NOx emissions are from anthropogenic activities such as the combustion of fossil fuels [8].

There are three main types of combustion NOx emissions: thermal NOx (Zel'dovich mechanism), prompt NOx (Fenimore mechanism), and fuel NOx. The main difference is that thermal NOx and prompt NOx are derived from nitrogen in the air, while fuel NOx is derived from nitrogen in the fuel composition. The detailed differences are as follows. Thermal NOx is formed by the reaction between nitrogen in air and oxygen produced by the reaction under high-temperature conditions and accounts for the majority of NOx production derived from nitrogen in the air. Thermal NOx has a strong temperature dependence, and is more actively formed close to the stoichiometric equivalence ratio, where the flame temperature is almost at its maximum. Prompt NOx is known to be caused by intermediate products such as hydrocarbon radicals, which are produced in much smaller amounts than thermal NOx. However, the production of prompt NOx is not negligible at low temperatures, high fuel concentration, and low residence time of combustion, where thermal NOx emissions are low, and prompt NOx emissions are relatively high.

There are mainly two NOx emission reduction measures: Rich Quench Lean (RQL) combustion [9, 10] and Lean (e.g., Lean Premixed Prevaporized (LPP)) combustion [11, 12]. Both methods aim to reduce the flame temperature, thereby reducing the emission of NOx. In RQL combustion, the combustor is first fed with a higher equivalence ratio (more fuel, less air) in the first stage of a combustor. Afterward, air is introduced through the sidewalls, and the equivalence ratio is reduced to below the stoichiometric ratio for re-combustion. This RQL combustion method is currently employed in many gas turbine engines, but has the disadvantage of limited NOx reduction because the equivalence ratio transits to a lean equivalence ratio from a rich equivalence ratio, and the gas experiences the stoichiometric equivalence ratio.

Conversely, lean combustion uses less fuel, and more air enters the combustor to react in a lean state, thus reducing NOx emissions further. However, lean combustion is known to cause unstable combustion characterized by combustion instability [13–26], combustion noise [27–30], flashback [31–34], and blow-off [35–37]. Combustion instability is a phenomenon in which large amplitude pressure oscillations are sustained inside the enclosed combustor due to the correlation of pressure and heat release rate. Once the pressure oscillation coincides with the resonant mode of the combustor structure, it causes catastrophic damage. Combustion noise refers to the sound wave (pressure wave) generated by unsteady flow and flame oscillations, which is not only noisy, but also damaging to sensitive equipment. Flashback is a phenomenon in which the flame propagates upstream beyond the design assumptions due to changes in the fuel/oxidizer mixing and inflow rate. When the flame reaches the upstream inlet system, the components that are not equipped with a cooling mechanism are exposed to high temperatures and high pressures, which may result in explosions. Blow-off is a phenomenon in which the flame extinguishes, and mainly, two factors cause this. The first is that the flame is blown away, which is caused by a too-high inflow velocity, resulting in the flame being swept downstream. The second is the inability to sustain the flame. This is caused by a too-high strain rate and insufficient heat release to sustain combustion due to an equivalence ratio that is too low or too high; that is, the combustion limit is exceeded.

The unstable combustion described above is a combustion phenomenon in unsteady flow, and the conditions under which it occurs and the flame behavior vary significantly depending on the combustion conditions and other factors. In addition, a detailed theory of unstable combustion has not been fully established due to the complicated interactions among turbulence, mixing, chemical reactions, and other factors such as evaporation when liquid fuel is used. All types of unstable combustion need to be controlled; however, this study focuses on combustion instability and combustion noise among these phenomena, and discusses local unsteady phenomena that are difficult to include in experiments via numerical simulations.

The reasons for the incomplete understanding of combustion instability are the com-

plicated phenomena involved and the complex geometries of actual combustors. In real combustors, several factors, such as the interaction of the flame with a wall surface, fuel characteristics, and the shape of the combustor, affect each other. Therefore, to elucidate the factors affecting combustion instability, various combustion instability studies have been conducted [13–26], and two of them are noteworthy. Two of these are the combustion instability in a back-step combustor fueled by kerosene and a low-swirl combustor fueled by lean gaseous hydrogen. Concerning the former configuration, kerosene is a liquid fuel commonly used as aviation fuel, and its oscillation phenomena are very complicated due to the movement and evaporation of fuel droplets. Using a back-step combustor makes it possible to consider only oscillation phenomena at the back-step, which exists in almost all combustors, while excluding the effects of swirling flow, which also exists in commercial combustors. In previous studies, the effects of droplet diameter [22] and fuel inflow conditions [25] have been studied for this back-step combustor using Large-eddy simulation (LES), but these studies fixed the equivalent ratio to unity and did not consider oscillation phenomena under lean conditions at which the emission of NOx is reduced. Concerning the latter configuration, as mentioned above, hydrogen fuel is a promising alternative fuel, and the low-swirl combustor is being studied for application to gas turbine combustors because of its superior low-emission performance. This low-swirl combustor was originally developed by a Lawrence Berkeley National Laboratory group for basic turbulent combustion research [38, 39]. However, there have not been many studies on its unstable combustion, and a study by Shoji et al. [17, 18] observed a unique oscillation phenomenon that has not been observed in other studies.

Regarding combustion noise, the main source elements of jet engine noise are considered to be fans, compressors, turbine blades, combustors, and jet exhaust. Through the ongoing efforts of researchers and engineers, noises emitted from elements other than the combustor have been reduced significantly by modifying geometry or developing effective acoustic liners. However, the noise generation mechanism from combustors is not fully understood, and its relative contribution to engine noise has increased. In particular, the adoption of lean premixed combustion to suppress NOx emissions could induce com-

bustion instability in a combustor [11, 12], increasing the combustion noise. Research aimed at elucidating combustion noise is being undertaken both experimentally and numerically at home and abroad. For instance, experimental studies for combustion noise generated by an open turbulent premixed flame [40] have been conducted, and experimental studies of combustion noise with confined configurations, which often consist of thermo-acoustic instabilities, have also been conducted [41]. In an actual combustor, it is expected that the combustor walls affect the combustion noise, but the effects of the walls on the acoustics or flame oscillations have not been elucidated yet.

Therefore, in this study, three topics are focused on and numerically investigated in detail. They are the combustion instability in the back-step combustor, the combustion instability in the confined low-swirl combustor, and the combustion noise in the unconfined low-swirl combustor. Firstly, in order to examine the combustion instability behavior in lean combustion with liquid fuel, the equivalent ratio is varied from 0.6, 0.8, to 1.0 in a kerosene-fueled back-step combustor, and its effect on the combustion instability is investigated. Secondly, a numerical simulation is also performed on a hydrogen-fueled low-swirl combustor to study in detail the peculiar oscillation phenomenon that Shoji et al. discovered in the combustor's combustion instability [17, 18]. Finally, to examine the effect of wall surfaces alone on combustion noise, a wall is placed near the flame in a hydrogen-fueled low-swirl combustor, which is identical to the combustor of combustion instability described above. All of these studies are performed using LES using turbulent combustion models.

1.2 Thesis outline

This thesis comprises six chapters.

Chapter 1, the present chapter, describes the background, purpose of the study, and outline of this thesis.

Chapter 2 describes the fundamental theory of combustion instability that helps readers understand the basic physics and the background of each analysis conducted in this thesis.

Chapter 3 explores the combustion instability in a back-step flow. The liquid fuel, kerosene, is used as the fuel. LES is performed for different equivalence ratios, and the effects of the equivalence ratio on the combustion instability are investigated. For the calculations of the reactions, the two-step global reaction model [20] is used with the dynamically thickened flame model [42, 43] to resolve the flame surface on the coarser LES grid.

Chapter 4 explores the combustion instability in a low-swirl combustor. Lean hydrogen is used as the gas fuel. LES is performed, and the unique phenomena that are observed in the experiment for the first time are investigated in detail. For the calculations of the reactions, the detailed reaction model [44] (9 species and 20 reactions) is used with the dynamically thickened flame model [42, 43] to resolve the flame surface on the coarser LES grid.

Chapter 5 explores the combustion noise in a low-swirl combustor with a wall plate close to the lean-hydrogen flame. A LES/APE-RF (Acoustic perturbation equations - reacting flow) approach is adopted, and the effect of the wall plate on the combustion noise in a far field is investigated. As a combustion model, the flamelet generated manifold (FGM) is used.

Chapter 6 summarizes this study and suggests future related areas of research.

Among the contents in this thesis, parts of Chapter 3 were originally reported in Journal of Thermal Science and Technology (JTST) [45], parts of Chapter 4 were originally reported in Physics of Fluids [46], and parts of Chapter 5 were originally reported in Physics of Fluids [47], and they are used with the permission of AIP Publishing.

References

[1] O. Edenhofer, R. Pichs-Madruga, Y. Sokona, F. C. Minx, E. Farahani, S. Kadner, K. Seyboth, A. Adler, I. Baum, S. Brunner, P. Eickemeier, B. Kriemann, J. Savolainen, S. Schlömer, C. Stechow, and T. Zwickel. Working group iii contribution to the fifth assessment report of the intergovernmental panel on climate change. *Climate Change 2014 Mitigation of Climate Change*, 30:1783–1790, 2014.

[2] A. Gupta. Thermal characteristics of gaseous fuel flames using high temperature air. *Journal of Engineering for Gas Turbines and Power*, 126:9–19, 2004.

[3] R. Pavri and G. D. Moore. Gas turbine emissions and control. *GE Energy Services*, 2001.

[4] Q. Zhu. Developments on CO_2-utilization technologies. *Clean Energy*, 3:85–100, 2019.

[5] B. Huebert, P. Vitousek, J. Sutton, T. Elias, J. Heath, S. Coeppicus, S. Howell, and B. Blomquist. Volcano fixes nitrogen into plant-available forms. *Biogeochemistry*, 47:111–118, 1999.

[6] U. Schumann and H. Huntrieser. The global lightning-induced nitrogen oxides source. *Atmospheric Chemistry and Physics*, 7:3823–3907, 2007.

[7] B. Seok, D. Helmig, L. Ganzeveld, M. W. Williams, and C. S. Vogel. Dynamics of nitrogen oxides and ozone above and within a mixed hardwood forest in northern michigan. *Atmospheric Chemistry and Physics*, 13:7301–2013, 2013.

[8] A. A. Almetwally, M. Bin-Jumah, and A. A. Allam. Ambient air pollution and its influence on human health and welfare: an overview. *Environmental Science and Pollution Research*, 27:24815–24830, 2020.

[9] S. M. Correa. Power generation and aeropropulsion gas turbines: From combustion science to combustion technology. *Symposium (International) on Combustion*, 27:1793–1807, 1998.

[10] A. S. Feitelberg and M. A. Lacey. The ge rich-quench-lean gas turbine combustor. *Journal of Engineering for Gas Turbines and Power*, 120:502–508, 1998.

[11] T. Lieuwen and K. McManus. Introduction: Combustion dynamics in lean-premixed prevaporized (LPP) gas turbines. *Journal of Propulsion and Power*, 19:721–721, 2003.

[12] D. G. Nicol, R. C. Steele, N. M. Marinov, and P. C. Malte. The importance of the nitrous oxide pathway to NOx in lean-premixed combustion. *Journal of Engineering for Gas Turbines and Power*, 117:100–111, 1995.

[13] F. Culick, M. Heitor, and J. Whitelaw. *Unsteady combustion*. Springer Science & Business Media, 1996.

[14] M. Zhu, A. Dowling, and K. Bray. Self-excited oscillations in combustors with spray atomizers. *Journal of Engineering for Gas Turbines and Power*, 123:779–786, 2001.

[15] J.-Y. Lee, E. Lubarsky, and B. Zinn. "Slow" active control of combustion instabilities by modification of liquid fuel spray properties. *Proceedings of the Combustion Institute*, 30:1757–1764, 2005.

[16] M. de la Cruz García, E. Mastorakos, and A. Dowling. Investigations on the self-excited oscillations in a kerosene spray flame. *Combustion and Flame*, 156:374–384, 2009.

[17] T. Shoji, S.Tachibana, T. Suzuki, Y. Nakazumi, and T. Yokomori. A new pattern of flame/flow dynamics for lean-premixed, low-swirl hydrogen turbulent jet flames under thermoacoustic instability. *Proceedings of the Combustion Institute*, 38:2835–2843, 2021.

[18] T. Shoji, S.Tachibana, Y. Nakazumi, R. Fujii, J. Masugi, and T. Yokomori. Detailed unsteady dynamics of flame-flow interactions during combustion instability and its transition scenario for lean-premixed low-swirl hydrogen turbulent flames. *Proceedings of the Combustion Institute*, 39:4741–4750, 2022.

[19] K. Moon, Y. Choi, and K. Kim. Experimental investigation of lean-premixed hydrogen combustion instabilities in a can-annular combustion system. *Combustion and Flame*, 235:111697, 2022.

[20] B. Franzelli, E. Riber, L. Gicquel, and T. Poinsot. Large eddy simulation of combustion instabilities in a lean partially premixed swirled flame. *Combustion and Flame*, 159(2):621–637, 2012.

[21] S. Tachibana, K. Saito, T. Yamamoto, M. Makida, T. Kitano, and R. Kurose. Experimental and numerical investigation of thermo-acoustic instability in a liquid-fuel aero-engine combustor at elevated pressure: Validity of large-eddy simulation of spray combustion. *Combustion and Flame*, 162(6):2621–2637, 2015.

[22] T. Kitano, K. Kaneko, R. Kurose, and S. Komori. Large-eddy simulations of gas- and liquid-fueled combustion instabilities in back-step flows. *Combustion and Flame*, 170:63–78, 2016.

[23] J. Li, Y. Xia, A. S. Morgans, and X. Hanc. Numerical prediction of combustion instability limit cycle oscillations for a combustor with a long flame. *Combustion and Flame*, 185:28–43, 2017.

[24] C. Kraus, L. Selle, and T. Poinsot. Coupling heat transfer and large eddy simulation for combustion instability prediction in a swirl burner. *Combustion and Flame*, 191:239–251, 2018.

[25] A. Pillai, J. Nagao, R. Awane, and R. Kurose. Influences of liquid fuel atomization and flow rate fluctuations on spray combustion instabilities in a backward-facing step combustor. *Combustion and Flame*, 220:337–356, 2020.

[26] L. Yuanzhe, L. P. nad W. Zhuopu, A. Wen, and G. Yu. Large eddy simulation of combustion instability in a subcritical hydrogen peroxide/kerosene liquid rocket engine: Intermittency route to period-2 thermoacoustic instability. *Physics of Fluids*, 35, 2023.

[27] W. C. Strahle and B. N. Shivashankara. A rational correlation of combustion noise results from open turbulent premixed flames. *Proceedings of the Combustion Institute*, 15:1379–1385, 1975.

[28] S. Kotake and K. Takamoto. Combustion noise: Effects of the shape and size of burner nozzle. *Journal of Sound and Vibration*, 112:345–354, 1987.

[29] M. Merk, W. Polifke, R. Gaudron, M. Gatti, C. Mirat, and T. Schuller. Measurement and simulation of combustion noise and dynamics of a confined swirl flame. *AIAA J.*, 56, 2018.

[30] M. Merk, R. Gaudron, M. Gatti, C. Mirat, T. Schuller, and W. Polifke. Prediction of combustion noise of an enclosed flame by simultaneous identification of noise source and flame dynamics. *Proceedings of the Combustion Institute*, 37:5263–5270, 2019.

[31] C. Eichler, G. Baumgartner, and T. Sattelmayer. Experimental investigation of turbulent boundary layer flashback limits for premixed hydrogen-air flames confined in ducts. *Journal of Engineering for Gas Turbines and Power*, 134:011502, 2012.

[32] A. Gruber, J. Chen, D. Valiev, and C. Law. Direct numerical simulation of premixed flame boundary layer flashback in turbulent channel flow. *Journal of Fluid Mechanics*, 709:516–542, 2012.

[33] T. Kitano, T. Tsuji, R. Kurose, and S. Komori. Effect of pressure oscillations on flashback characteristics in a turbulent channel flow. *Energy & Fuel*, 29:6815–6822, 2015.

[34] D. Ebi, R. Bombach, and P. Jansohn. Swirl flame boundary layer flashback at elevated pressure: Modes of propagation and effect of hydrogen addition. *Proceedings of the Combustion Institute*, 38:6345–6353, 2021.

[35] L. Esclapez, P. Ma, E. Mayhew, R. Xu, S. Stouffer, T. Lee, H. Wang, and M. Ihme. Fuel effects on lean blow-out in a realistic gas turbine combustor. *Combustion and Flame*, 181:82–99, 2017.

[36] L. Zheng, J. Cronly, E. Ubogu, I. Ahmed, Y. Zhang, and B. Khandelwal. Experimental investigation on alternative fuel combustion performance using a gas turbine combustor. *Applied Energy*, 238:1530–1542, 2019.

[37] A. Aniello, T. Poinsot, L. Selle, and T. Schuller. Hydrogen substitution of natural-gas in premixed burners and implications for blow-off and flashback limits. *International Journal of Hydrogen Energy*, 47:33067–33081, 2022.

[38] R. Cheng, D. Yegian, M. Miyasato, G. Samuelsen, C. Benson, R. Pellizzari, and P. Loftus. Scaling and development of low-swirl burners for low-emission furnaces and boilers. *Proceedings of the Combustion Institute*, 28:1305–1313, 2000.

[39] R. Cheng, D. Littlejohn, P. Strakey, and T. Sidwell. Laboratory investigations of a low-swirl injector with H2 and CH4 at gas turbine conditions. *Proceedings of the Combustion Institute*, 32:3001–3009, 2009.

[40] T. Shoji, Y. Iwasaki, K. Kodai, S. Yoshida, S. Tachibana, and T. Yokomori. Effects of flame behaviors on combustion noise from lean-premixed hydrogen low-swirl flames. *AIAA J.*, 58:4505–4521, 2020.

[41] K. Pausch, S. Herff, and W. Schröder. Noise sources of an unconfined and a confined swirl burner. *Journal of Sound and Vibration*, 475:115293, 2020.

[42] F. Charlette, C. Meneveau, and D. Veynante. A power-law flame wrinkling model for LES of premixed turbulent combustion Part I: non-dynamic formulation and initial tests. *Combustion and Flame*, 131(1):159–180, 2002.

[43] J.-P. Légier, T. Poinsot, and D. Veynante. Dynamically thickened flame LES model for premixed and non-premixed turbulent combustion. *Proceedings of the summer program*, 157–168, 2000.

[44] J. A. Miller and C. T. Bowman. Mechanism and modeling of nitrogen chemistry in combustion. *Progress in Energy and Combustion Science*, 15:287–338, 1989.

[45] J. Nagao, A. Pillai, and R. Kurose. Investigation of temporal variation of combustion instability intensity in a back step combustor using les. *Journal of Thermal Science and Technology*, 15:JTST0036–JTST0036, 2020.

[46] J. Nagao, A. Pillai, T. Shoji, S.Tachibana, T. Yokomori, and R. Kurose. Large-eddy simulation of a lean-premixed hydrogen flame in a low-swirl combustor under combustion instability. *Physics of Fluids*, 35:105124, 2023.

[47] J. Nagao, A. Pillai, T. Shoji, S.Tachibana, T. Yokomori, and R. Kurose. Numerical investigation of wall effects on combustion noise from a lean-premixed hydrogen/air low-swirl flame. *Physics of Fluids*, 35:014109, 2023.

Chapter 2

Theory of combustion instability

2.1 Thermoacoustic modes

Combustion instability is a phenomenon in which pressure oscillations in a combustor and its characteristics, such as the frequency and intensity, are affected by the oscillation modes, which are determined by the combustor's shape and combustion type. Therefore, organizing and understanding these oscillation modes in the combustor is beneficial in understanding combustion instability phenomena.

These modes consist of an enormous amount of different modes, including higher-order modes. Here, only the fundamental modes are organized: Longitudinal mode [1, 2], Tangential mode [3, 4], Radial mode [5], and Helmholtz mode [6, 7]. Figure 2.1 shows the pressure distributions for the Longitudinal, Tangential, and Radial modes, and Fig. 2.2 shows a conceptual diagram of the Helmholtz mode. The combustor shown here has a wall at the bottom of the injector and an open end at the combustor outlet (top surface).

The first commonly observed mode is the longitudinal mode, which is column resonance, and here, the 3/4 wavelength of the length of the combustor in the main flow direction is shown. The antinodes of the oscillation sit around the wall surface at the bottom of the injector and the position where the flame exists just downstream of the combustor entrance. The oscillation nodes exist inside the injector and the combustor

exit. Note that, in reality, the wavelength deviates due to temperature distribution and open-end correction. The oscillation frequency can be roughly estimated from the wavelength and sound velocity using $f = c/\lambda$. Here, f is the frequency, c is the sound speed, and λ is the wavelength, which is predictable from the mode type.

The tangential mode (1st standing) is also like a column resonance with walls at both ends in the tangential direction. Therefore, the antinode of the oscillation is located near the side wall, and the center of the combustor is the position of the oscillation node. The tangential mode (1st standing) is characterized by the fact that the position of the antinode and the node of pressure oscillation do not change.

In contrast, the Tangential mode (1st spinning) is a mode in which the antinode and the node of the oscillation move and spin in the tangential direction and the direction of the spinning changes depending on the acoustic conditions.

The radial mode (1st mode) also resembles a column resonance between the outer and inner walls of the combustor, and the antinode is located near the inner and outer walls of the combustor.

The Helmholtz mode is a different oscillation mechanism compared to the column resonance, in which, as an analogy, the gas inside the combustor is compared to a spring, and the gas flowing in and out of the combustor to a mass attached to the spring. When the inflow gas fluctuates, the air inside the combustor is compressed and acts as a spring, and the outflow gas resonates in tune. The main difference between this mechanism and column resonance is that column resonance has antinodes and nodes of pressure oscillation in the combustor, whereas in the Helmholtz mode, the pressure of the entire combustor changes at the same phase and does not have antinodes or nodes.

As mentioned above, the oscillation can be organized into various types of oscillation modes, but in actual oscillation phenomena, various oscillation modes, including higher orders, coexist, and the frequency may be affected by other modes. For example, when longitudinal and radial modes coexist, and the amplitude of the longitudinal mode is large, the frequency of the radial mode may coincide with the longitudinal mode. When these modes coexist and have complicated interactions, it is difficult to identify each

mode only by investigating the time variation of the pressure distribution. In this situation, the mode of pressure oscillation can be decomposed by frequency using Dynamic Mode Decomposition (DMD). However, it is essential to note that, in order to understand how each mode of pressure oscillation contributes to the velocity and heat release rate fluctuations, it is necessary to examine each mode in a combined manner.

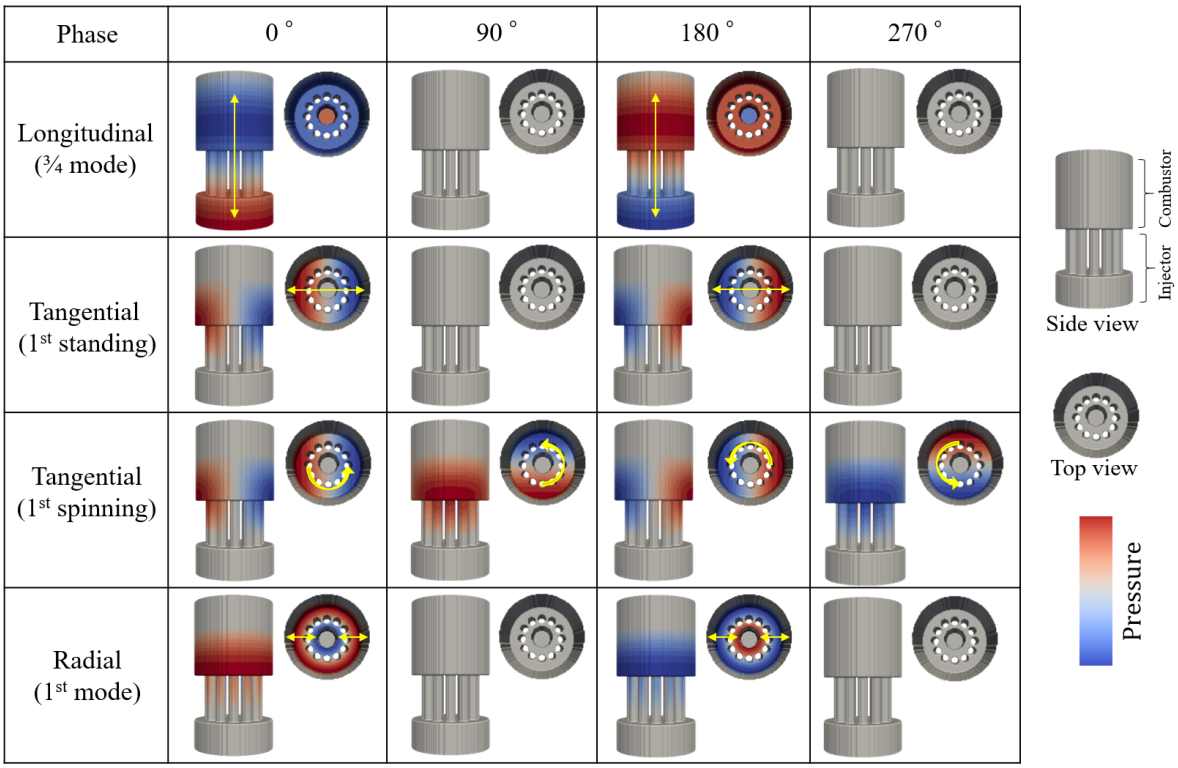

Figure 2.1: Comparison of pressure oscillation modes, longitudinal (3/4 mode), tangential (1st standing), tangential (1st spinning), and radial (1st mode).

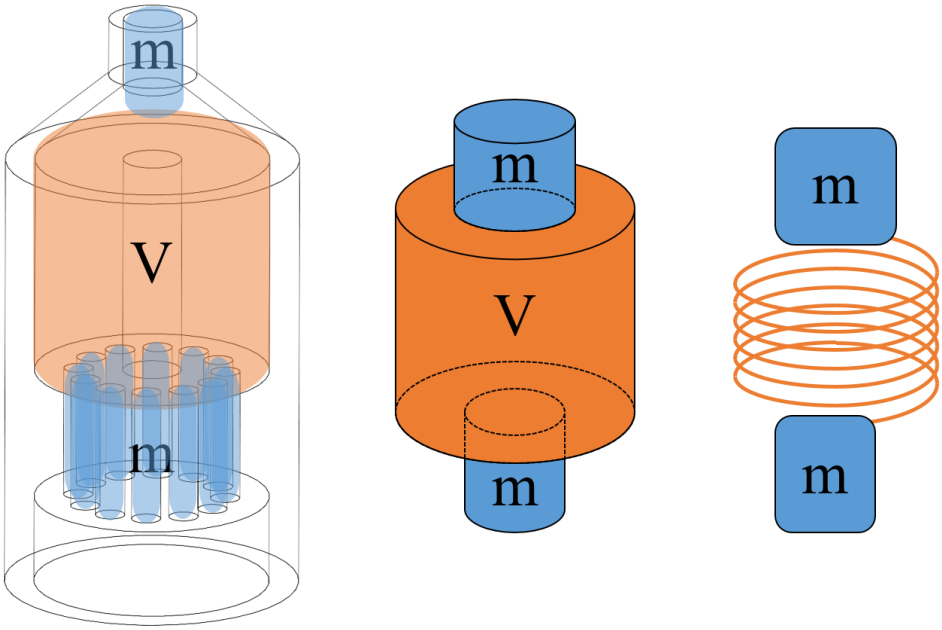

Figure 2.2: Schematic of the Helmholtz oscillation mode.

2.2 Rayleigh criterion

In the history of combustion instability research, the Rayleigh criterion was developed by Rayleigh et al. in 1878 [8] as an indicator of combustion stability. This criterion has been used in many combustion instability studies and has provided some valuable insights into combustion instability phenomena.

The classical Rayleigh criterion states that combustion instability is driven when the following conditions are satisfied: P' for pressure oscillation and q' for heat release rate fluctuation, and

$$\int_V P'q'dV > 0. \tag{2.1}$$

In order to understand the physical meaning of this condition, the fundamental equations of fluid dynamics are transformed as follows. The fundamental equations are the conservation equations of mass, momentum, and energy and the equation of state.

$$\frac{\partial \rho}{\partial t} + \rho \nabla \cdot \boldsymbol{u} = 0 \tag{2.2}$$

$$\rho \frac{D\boldsymbol{u}}{Dt} = -\nabla P + \nabla \cdot \boldsymbol{\tau} \tag{2.3}$$

$$\rho c_p \frac{DT}{Dt} = \frac{DP}{Dt} + \nabla \cdot (\lambda_T \nabla T) + \dot{\omega}_T \tag{2.4}$$

$$P = \rho RT \tag{2.5}$$

For the simplification of derivation, the assumptions listed below are introduced. The viscous term $\nabla \cdot \boldsymbol{\tau}$ in Eq. (2.3) is neglected, and the isentropic flow is assumed, then the heat transfer term $\nabla \cdot (\lambda_T \nabla T)$ in Eq. (2.4) is neglected. Also, zero Mach assumption is assumed, which means time-averaged velocity is zero, $\boldsymbol{u_0} = 0$. After all, by dividing each value into time-averaged value and the fluctuations, density ρ, velocity $\boldsymbol{u}$, pressure P, temperature T, and reaction rates $\dot{\omega}_T$ can be written as, $\rho = \rho_0 + \rho'$, $\boldsymbol{u} = \boldsymbol{u_0} + \boldsymbol{u'} = \boldsymbol{u'}$, $P = P_0 + P'$, $T = T_0 + T'$, and $\dot{\omega}_T = \dot{\omega}_{T,0} + \dot{\omega}'_T$ respectively.

First, the mass conservation equation is modified as,

$$\frac{\partial(\rho_0 + \rho')}{\partial t} + (\rho_0 + \rho')\nabla \cdot \boldsymbol{u'} = 0. \tag{2.6}$$

Then it becomes,

$$\frac{\partial \rho_0}{\partial t} + \frac{\partial \rho'}{\partial t} + \rho_0 \nabla \cdot \boldsymbol{u'} + \rho' \nabla \cdot \boldsymbol{u'} = 0. \tag{2.7}$$

ρ_0 is the time-averaged value, so the 1st term is zero as, $\frac{\partial \rho_0}{\partial t} = 0$, and the 4th term of second order is neglected as $\rho' \nabla \cdot \boldsymbol{u'} \approx 0$, and it reads,

$$\frac{\partial \rho'}{\partial t} + \rho_0 \nabla \cdot \boldsymbol{u'} = 0. \tag{2.8}$$

Second, the momentum conservation equation is modified as,

$$(\rho_0 + \rho') \frac{D\boldsymbol{u'}}{Dt} = -\nabla (P_0 + P'). \tag{2.9}$$

Then it becomes,

$$\rho_0 \frac{D\boldsymbol{u'}}{Dt} + \rho' \frac{D\boldsymbol{u'}}{Dt} = -\nabla P_0 - \nabla P'. \tag{2.10}$$

The 2nd term of LHS of second order, $\rho' \frac{D\boldsymbol{u'}}{Dt}$, is neglected. The 1st term is devided into $\rho_0 \frac{\partial \boldsymbol{u'}}{\partial t} + \rho_0 \boldsymbol{u'} \cdot \nabla \boldsymbol{u'}$, and the 2nd term of this, $\rho_0 \boldsymbol{u'} \cdot \nabla \boldsymbol{u'}$ is also neglected due to its 2nd order. Also, the momentum conservation equation should be satisfied for the time-averaged flow field,

$$\rho_0 \frac{D\boldsymbol{u_0}}{Dt} = -\nabla P_0. \tag{2.11}$$

Here, zero Mach condition is assumed as $\boldsymbol{u_0} = 0$, so it yields,

$$\nabla P_0 = 0. \tag{2.12}$$

Then, by using Eq. (2.12), Eq. (2.10) is rewritten as,

$$\rho_0 \frac{\partial \boldsymbol{u'}}{\partial t} = -\nabla P'. \tag{2.13}$$

Third, the energy conservation equation is modified as,

$$(\rho_0 + \rho') c_p \frac{D(T_0 + T')}{Dt} = \frac{D(P_0 + P')}{Dt} + \dot{\omega}_{T,0} + \dot{\omega}'_T. \tag{2.14}$$

Analogous to the discussion of the momentum equation, the energy equation should also be satisfied for the time-averaged flow field.

$$\rho_0 c_p \frac{DT_0}{Dt} = \frac{DP_0}{Dt} + \dot{\omega}_{T,0}. \tag{2.15}$$

By neglecting 2nd order term of LHS of Eq. (2.14), $\rho' c_p \frac{DT'}{Dt}$, and deducting Eq. (2.15) from Eq. (2.14), Eq. (2.14) becomes

$$\rho_0 c_p \frac{DT'}{Dt} + \rho' c_p \frac{DT_0}{Dt} = \frac{DP'}{Dt} + \dot{\omega}'_T. \tag{2.16}$$

Then we obtain,

$$\begin{aligned} \rho_0 c_p \frac{\partial T'}{\partial t} + \rho_0 c_p \boldsymbol{u'} \cdot \nabla T' + \rho' c_p \frac{\partial T_0}{\partial t} + \rho' c_p \boldsymbol{u'} \cdot \nabla T_0 \\ = \frac{\partial P'}{\partial t} + \boldsymbol{u'} \cdot \nabla P' + \dot{\omega}'_T. \end{aligned} \tag{2.17}$$

Here, the 2nd term of LHS, $\rho_0 c_p \boldsymbol{u'} \cdot \nabla T'$, the 4th term of LHS, $\rho' c_p \boldsymbol{u'} \cdot \nabla T_0$, and the 2nd term of RHS, $\boldsymbol{u'} \cdot \nabla P'$ are neglected. Moreover the time derivative of time-averaged value is zero as $\frac{\partial T_0}{\partial t} = 0$, so the energy equation finally becomes,

$$\rho_0 c_p \frac{\partial T'}{\partial t} = \frac{\partial P'}{\partial t} + \dot{\omega}'_T. \tag{2.18}$$

Finally, by taking the logarithm of the equation of state,

$$log(P) = log(\rho) + log(R) + log(T). \tag{2.19}$$

Then, the time derivative of Eq. (2.19) is

$$\frac{1}{P}\frac{\partial P}{\partial t} = \frac{1}{\rho}\frac{\partial \rho}{\partial t} + \frac{1}{T}\frac{\partial T}{\partial t}. \tag{2.20}$$

By dividing each value into averaged values and fluctuations,

$$\frac{1}{P_0 + P'}\frac{\partial (P_0 + P')}{\partial t} = \frac{1}{\rho_0 + \rho'}\frac{\partial (\rho_0 + \rho')}{\partial t} + \frac{1}{T_0 + T'}\frac{\partial (T_0 + T')}{\partial t}. \tag{2.21}$$

Here, time derivative of time-averaged values, $\frac{\partial P_0}{\partial t}$, $\frac{\partial \rho_0}{\partial t}$, and $\frac{\partial T_0}{\partial t}$ are zero, and by using the assumption of time-averaged values are big enough compared with fluctuations as, $\frac{1}{P_0+P'} \approx \frac{1}{P_0}$, $\frac{1}{\rho_0+\rho'} \approx \frac{1}{\rho_0}$, and $\frac{1}{T_0+T'} \approx \frac{1}{T_0}$, Eq. (2.21) becomes,

$$\frac{1}{P_0}\frac{\partial P'}{\partial t} = \frac{1}{\rho_0}\frac{\partial \rho'}{\partial t} + \frac{1}{T_0}\frac{\partial T'}{\partial t}. \tag{2.22}$$

By combining, Eq. (2.18) and Eq. (2.22),

$$\frac{1}{\rho_0}\frac{\partial \rho'}{\partial t} = \frac{1}{P_0}\frac{\partial P'}{\partial t} - \frac{1}{T_0}\frac{\partial T'}{\partial t} = \frac{1}{P_0}\frac{\partial P'}{\partial t} - \frac{1}{T_0}\frac{1}{\rho_0 c_p}\left(\frac{\partial P'}{\partial t} + \dot{\omega}'_T\right). \tag{2.23}$$

Then, by multiplying Eq. (2.23) by ρ_0, and using the relation $\frac{1}{T_0} = \frac{\rho_0 R}{P_0}$ derived from the equation of state, it becomes

$$\frac{\partial \rho'}{\partial t} = \frac{\rho_0}{P_0}\left(1 - \frac{R}{c_p}\right)\frac{\partial P'}{\partial t} - \frac{1}{T_0 c_p}\dot{\omega}'_T. \tag{2.24}$$

By considering the relation, $R = c_p - c_v$, and the sound speed, c, which is calculated as $c^2 = \frac{\kappa p_0}{\rho_0}$ (κ is the heat capacity ratio), Eq. (2.24) becomes as below.

$$\frac{\partial \rho'}{\partial t} = \frac{1}{c^2}\frac{\partial P'}{\partial t} - \frac{1}{T_0 c_p}\dot{\omega}'_T. \tag{2.25}$$

Furthermore, by combining Eq. (2.25) and Eq. (2.8), it yields

$$\frac{1}{c^2}\frac{\partial P'}{\partial t} + \rho_0 \nabla \cdot \boldsymbol{u'} = \frac{1}{T_0 c_p}\dot{\omega}'_T. \tag{2.26}$$

By multiplying Eq. (2.26) by $\frac{P'}{\rho_0}$, we acquire

$$\frac{P'}{\rho_0 c^2}\frac{\partial P'}{\partial t} + P' \nabla \cdot \boldsymbol{u'} = \frac{1}{\rho_0 T_0 c_p} P' \dot{\omega}'_T. \tag{2.27}$$

Also by multiplying Eq. (2.13) by $\boldsymbol{u'}$, we acquire

$$\rho_0 \boldsymbol{u'}\frac{\partial \boldsymbol{u'}}{\partial t} = -\boldsymbol{u'}\nabla P'. \tag{2.28}$$

The summation of Eq. (2.27) and Eq. (2.28) becomes

$$\frac{\partial}{\partial t}\left(\frac{1}{2}\rho_0 \boldsymbol{u'}^2 + \frac{1}{2}\frac{P'^2}{\rho_0 c^2}\right) + \boldsymbol{u'}\nabla P' + P' \nabla \cdot \boldsymbol{u'} = \frac{1}{\rho_0 T_0 c_p} P' \dot{\omega}'_T. \tag{2.29}$$

Eventually, Eq. (2.29) is rewritten as

$$\frac{\partial}{\partial t}\left(\frac{1}{2}\rho_0 \boldsymbol{u'}^2 + \frac{1}{2}\frac{P'^2}{\rho_0 c^2}\right) + \nabla \cdot \boldsymbol{u'} P' = \frac{\kappa - 1}{\kappa P_0} P' \dot{\omega}'_T. \tag{2.30}$$

Since the energy balance of the system as a whole is in the interest, Eq. (2.30) is spatially integrated.

$$\frac{\partial}{\partial t}\int_V \left(\frac{1}{2}\rho_0 \boldsymbol{u'}^2 + \frac{1}{2}\frac{P'^2}{\rho_0 c^2}\right) dV + \int_S \boldsymbol{u'} P' \cdot d\boldsymbol{S} = \int_V \frac{\kappa - 1}{\kappa P_0} P' \dot{\omega}'_T dV \tag{2.31}$$

The first term of the LHS, $\int_V \frac{1}{2}\rho_0 \boldsymbol{u'}^2 + \frac{1}{2}\frac{P'^2}{\rho_0 c^2} dV (:= E)$, is called acoustic energy which represents the energy of oscillation. The second term of the LHS, $\int_S \boldsymbol{u'} P' \cdot d\boldsymbol{S} (:= F)$, is

called acoustic flux, which means the energy flux into and out of the combustor through the boundaries of the domain. The first term of RHS, $\int_V \frac{\kappa-1}{\kappa P_0} P' \dot{\omega}'_T dV (:= RI)$, is called the Rayleigh term and indicates the degree of correlation between pressure oscillations and heat release rate fluctuations, and the contribution of this correlation to the pressure acoustic energy.

$$\frac{\partial}{\partial t} E + F = RI \tag{2.32}$$

In the classical Rayleigh criterion, only the Rayleigh term, RI, is considered, but based on the discussion and derivation above, the effect of acoustic flux, F, should also be included, and the criterion becomes,

$$F \leqq RI. \tag{2.33}$$

When this criterion is satisfied, the combustion instability is considered to have a limit cycle of pressure oscillation ($F = RI$) or be in the driven condition ($F < RI$).

However, these arguments ignore energy loss due to viscosity and heat loss and assume isentropic flow, but such conditions are unrealistic. Therefore, even if the criterion of Eq. (2.33) is satisfied, it does not necessarily mean that combustion instability is driven in a real situation. There is also a criterion by Chu et al. [9], which is derived without assuming isentropic flow, but it is not discussed in detail here.

As described above, the Rayleigh criterion is sometimes questionable in its ability to accurately describe physical phenomena in practical use, but there is a derivative of this criterion called local Rayleigh Index (RI) that does not perform spatial integration but only time integration. This index shows the position of the flame in relation to the pressure phase and is a useful index for indicating where and how much the flame oscillates in relation to the pressure oscillation. This index is used in the following discussion of combustion instability.

2.3 Feedback process

As discussed in the previous section, combustion instability is theoretically known to be driven by the correlation of pressure and heat release rate. However, the actual oscillation phenomena inside a combustor are very complicated and are a feedback system where a cause-and-effect chain of each phenomenon forms a loop. A schematic of the feedback system in combustion instability is shown in Fig. 2.3. For simplicity, only the pressure oscillation, heat release rate fluctuation, velocity fluctuation, and concentration fluctuation are considered here. In the discussion of a feedback system, it does not make sense to discuss "which factor is the cause," but in order to describe the process of physical phenomena, the pressure oscillation is chosen as a starting point for the description of each cause-and-effect.

Once the pressure fluctuates inside the combustor, the pressure gradient also fluctuates, and it causes a velocity fluctuation. This velocity fluctuation causes a fluctuation in the fuel supply into diffusion flame and partially premixed flame, which eventually causes a concentration fluctuation. Then, the transformations of flame shape due to the velocity and concentration fluctuations increase the heat release rate fluctuation. This heat release rate fluctuation is accompanied by a fluctuation of thermal expansion, which induces pressure oscillations. These factors are the primary feedback mechanism of combustion instability. In the actual feedback mechanism, the oscillation energy dissipates during the oscillation, so the oscillation is balanced by the factor that drives the combustion instability and reaches a limit cycle.

Therefore, in discussing the characteristics of combustion instability, it is vital to organize and understand the factors that drive and dampen combustion instability [10, 11]. Figure 2.4 shows the conceptual diagram of the flow and flame processes that drive or dampen combustion instability.

The driving factors that are related to the velocity fluctuation are mainly (d1) air inflow fluctuation, (d2) fuel inflow fluctuation, (d3) swirling flow fluctuation, and (d4) vortex shedding fluctuation. The factors related to the concentration fluctuation are (d5) mixing fluctuation and (d6) concentration fluctuation itself. The factors related

to the heat release rate fluctuation are (d7) fluctuation of the flame area and (d8) fluctuation of reaction rate due to pressure oscillation. A more detailed description of each factor is as follows. (d1) Air inflow fluctuation and (d2) fuel inflow fluctuation are caused by the oscillation of pressure and its gradient in the inlet channel, which alters the velocity of air and fuel entering the combustor. For example, when the pressure in the inlet channel increases and the air and fuel discharge pressure is constant, the inflow velocity decreases, and when the positive pressure gradient becomes stronger, the fluid deceleration effect becomes more substantial, and the inflow velocity decreases, and vice versa. (d3) The swirling flow fluctuation refers to the fact that the intensity of the swirling flow created by the swirler changes with the pressure oscillation and inflow velocity fluctuation in the inlet channel, although the geometrical swirl number of the swirler does not change. (d4) The vortex shedding fluctuation is the phenomenon of scale fluctuation of circulating flow behind the backstep. A prominent circulating flow is generated downstream of the backstep with a high inflow velocity, but when the inflow velocity is slow, the circulating flow becomes weak. Concerning (d5) mixing fluctuation, the turbulence intensity fluctuation is induced by the velocity fluctuation. When the turbulence intensity becomes weak, the mixing of air and fuel is suppressed, and when the turbulence intensity becomes strong, the mixing of them is accelerated. Regarding (d6) concentration fluctuation, it is induced by (d1) air inflow fluctuation and (d2) fuel inflow fluctuation, both of which occur at different locations in the inlet channel and in different phases, resulting in a fluctuation of the equivalence ratio flowing into the combustor. For (d7) fluctuation of flame area, the flame shape is mainly changed by (d3) swirling flow fluctuation and (d4) vortex shedding fluctuation, and these factors eventually change the flame surface area. If the combustion conditions are the same, the heat release rate per unit surface area can be assumed to be constant, so that the total heat release rate affected by the fluctuation in flame surface area will oscillate significantly. Concerning (d8) fluctuation of reaction due to pressure oscillation, the reaction rate, k, is calculated by an equation called the Arrhenius equation ($k = Aexp(-E/RT)$). Here, A, E, and R are constants, and T is the temperature. Since the temperature varies with pressure, the

reaction rate varies with pressure oscillation. These eight factors are the main factors driving combustion instability.

The damping factors are mainly (D1) viscous dissipation, (D2) heat loss, (D3) acoustic flux to the outside of the system, and (D4) frequency transfer from resonant frequency to other frequencies. The following discussion provides a detailed explanation of each. (D1) Viscous dissipation: the kinetic energy of the flow fluctuation, $1/2\rho_0 \boldsymbol{u'}^2$, which is a term in the acoustic energy, is converted to thermal energy by viscosity, resulting in a decrease in acoustic energy. (D2) Heat loss has a damping effect, mainly when walls or droplets exist. As described above, the acoustic energy is converted into thermal energy, and the thermal energy decreases due to heat loss at the wall and droplet. Although conversion from thermal energy to acoustic energy can also occur, the amount of conversion to acoustic energy decreases as the gas's thermal energy in the combustor decreases due to heat loss. For (D3) acoustic flux to the outside of the system, the acoustic energy is advected, which is considered by the term F in Eq. (2.32). There are two types of acoustic fluxes, incoming and outgoing, and the acoustic energy decreases on the condition that the outgoing flux is more eminent than the incoming flux. Finally, (D4) one of the factors that provoke frequency transfer from resonant frequency to others is explained. First, it is assumed that there is a single resonant frequency in pressure oscillation and that a turbulent flame with random fluctuations exists inside the combustor. Then, the pressure oscillations are subjected to random Doppler shift by the turbulence and flame, eventually generating random frequency pressure oscillations. Since these random frequency pressure oscillations are not resonance modes, there is no driving factor, and they will continue to decay. These are the main factors that dampen combustion instability.

Note, however, that even the driving factor can be a damping factor depending on conditions such as the phase difference with pressure oscillation. Therefore, when trying to suppress combustion instability, it is adequate to weaken the factors that drive combustion instability, shift the phase of driving factors, and strengthen the factor that damps combustion instability.

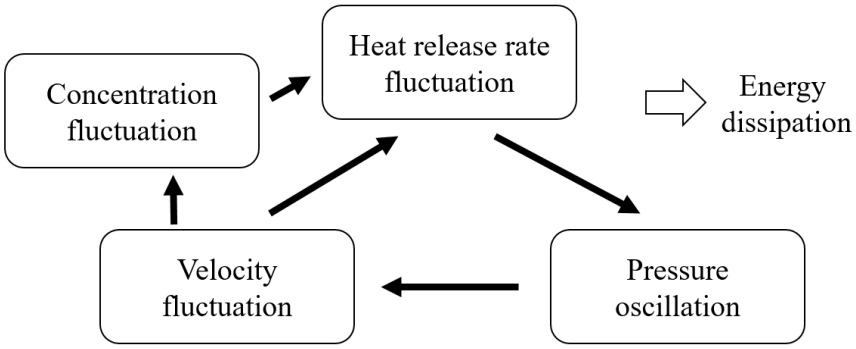

Figure 2.3: Conceptual diagram of the feedback system in combustion instability.

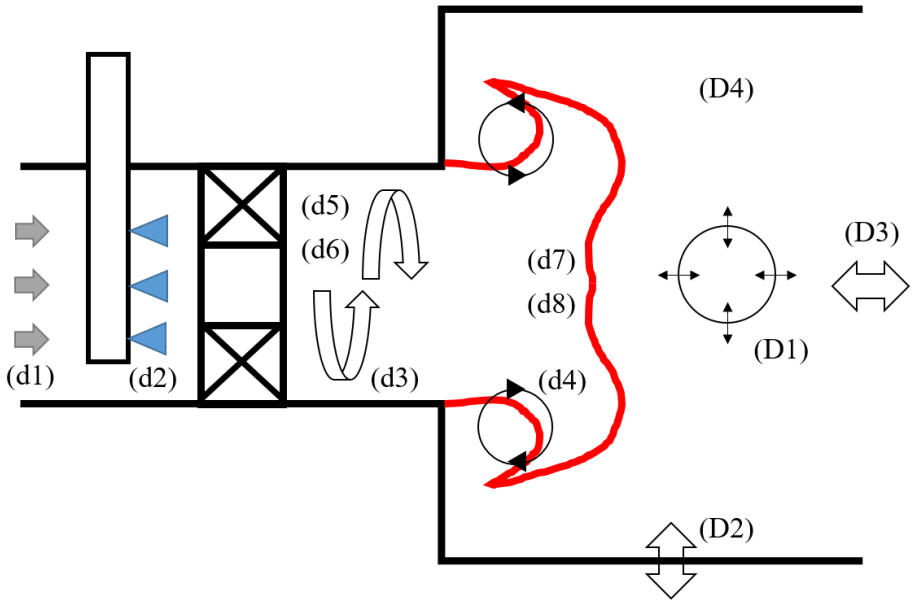

Figure 2.4: Conceptual diagram of flow and flame processes that drive or dampen combustion instability.

References

[1] A. Ghoniem, S. Park, A. Wachsman, A. Annaswamy, D. Wee, and H. Altay. Mechanism of combustion dynamics in a backward-facing step stabilized premixed flame. *Proceedings of the Combustion Institute*, 30:1783–1790, 2005.

[2] T. Shoji, S.Tachibana, T. Suzuki, Y. Nakazumi, and T. Yokomori. A new pattern of flame/flow dynamics for lean-premixed, low-swirl hydrogen turbulent jet flames under thermoacoustic instability. *Proceedings of the Combustion Institute*, 38:2835–2843, 2021.

[3] S. Xue, W. Yang, L. Zhou, and H. Liu. Experimental investigation of self-excited combustion instabilities in a small earth storable bipropellant rocket combustor. *Aerospace Science and Technology*, 105:106008, 2020.

[4] W. Chu, K. Guo, Y. Tong, and W. N. X. Li. Numerical analysis of self-excited tangential combustion instability for an MMH/NTO rocket combustor. *Proceedings of the Combustion Institute*, 39:5053–5061, 2023.

[5] A. Urbano, L. Selle, G. Staffelbach, B. Cuenot, T. Schmitt, S. Ducruix, and S. Candel. Exploration of combustion instability triggering using large eddy simulation of a multiple injector liquid rocket engine. *Combustion and Flame*, 169:129–140, 2016.

[6] J. E. Temme, P. M. Allison, and J. F. Driscoll. Combustion instability of a lean premixed prevaporized gas turbine combustor studied using phase-averaged PIV. *Combustion and Flame*, 161:958–970, 2014.

[7] B. Ahn, J. Lee, S. Jung, and K. Kim. Low-frequency combustion instabilities of an airblast swirl injector in a liquid-fuel combustor. *Combustion and Flame*, 196:424–438, 2018.

[8] L. Rayleigh. The explanation of certain acoustical phenomena. *Nature*, 18:319–321, 1878.

[9] B. Chu. *On the energy transfer to small disturbances in fluid flow (Part I).* Acta Mechanica, 1965.

[10] F. Culick, M. Heitor, and J. Whitelaw. *Unsteady combustion.* Springer Science & Business Media, 1996.

[11] T. Lieuwen and V. Yang. *Combustion instabilities in gas turbine engines: Operational experience, fundamental mechanisms and modeling.* American Institute of Aeronautics and Astronautics, Inc., 2005.

Nomenclature

c	: Sound speed [m/s]	RI	: Rayleigh term [kg m^2/s^3]
c_p	: Specific heat capacity [J/(K kg)]	ρ	: Density [kg/m^3]
E	: Acoustic energy [kg m^2/s^3]	t	: Time [s]
f	: Frequency [Hz]	T	: Temperature [K]
F	: Acoustic flux [kg m^2/s^3]	$\boldsymbol{\tau}$	: Viscous stress tensor [N/m^2]
λ	: Wave length [m]	$\boldsymbol{u}$	: Velocity [m/s]
λ_T	: Thermal conductivity [W/(m K)]	V	: Volume of cell [m^3]
ω_T	: Reaction rate [kg/m s^3]	**Subscripts**	
P	: Pressure [Pa]	0	: time-averaged
q	: Heat release rate [J/s]	**Superscripts**	
R	: Gas constant [J/(K mol)]	‘	: fluctuations

Chapter 3

LES of combustion instability in a back-step flow

3.1 Introduction

In this chapter, the effects of equivalence ratio on combustion instability in a back-step combustor are investigated using LES. The fuel in the combustor is liquid kerosene.

Combustion instability is caused by the interaction of pressure oscillation and heat release rate fluctuation [1]. However, there are many components that affect or induce combustion instability, such as turbulent flow, fuel particle movement, evaporation, and interaction with walls; hence, the detailed mechanisms are not fully understood. Therefore, to elucidate the mechanism of combustion instability in more detail, many experiments and numerical simulations have been conducted [2–5].

Experimental studies have suggested some solutions and characteristics of combustion instability; however, they have not fully elucidated its mechanism yet because of the limitation of data sampling. In contrast, numerical simulations have investigated abundant data in detail owing to the development of the scheme to calculate the combustion instability precisely [4–8], although spray combustion is complex due to many components that affect the combustion characteristics. In spray combustion, the behavior of injected fuel is affected by the pressure oscillation, and then the atomization process

is also influenced. Moreover, the regions where fuel droplets evaporate are disturbed by complex turbulent flow under combustion instability. Further, proceeding numerical studies [5, 9] investigated the influence of droplet size for spray combustion instability; however, in their study, the equivalence ratio was set as 1.0 for simplification, and the effect of equivalence ratio on combustion instability was not investigated.

Therefore, in this chapter, the equivalence ratio is varied as 0.6, 0.8, and 1.0, and the effect of the equivalence ratio on the combustion instability in turbulent spray combustion is investigated in a combustion chamber with back-step using LES. The dynamically thickened flame model is used as the turbulent combustion model, and a two-step global reaction model is used for kerosene-air flames. The influence of pressure oscillation on fuel atomization behavior is considered using a model that can predict the fuel droplet size with time.

3.2 Numerical methods

3.2.1 Governing equations

The governing equations for the gas phase considering fuel droplet effects are the conservation equations of mass, momentum, energy, and mass fraction of chemical species. These equations are solved with a semi-implicit compressible solver [10] as below.

$$\frac{\partial \overline{\rho}}{\partial t} + \nabla \cdot (\overline{\rho}\widetilde{\boldsymbol{u}}) = S_\rho, \tag{3.1}$$

$$\frac{\partial \overline{\rho}\widetilde{\boldsymbol{u}}}{\partial t} + \nabla \cdot (\overline{\rho}\widetilde{\boldsymbol{u}}\widetilde{\boldsymbol{u}}) = -\nabla \overline{P} + \nabla \cdot \boldsymbol{t} + S_{\rho u}, \tag{3.2}$$

$$\frac{\partial \overline{\rho}\widetilde{h}}{\partial t} + \nabla \cdot (\overline{\rho}\widetilde{h}\widetilde{\boldsymbol{u}}) = \frac{\partial \overline{P}}{\partial t} + \widetilde{\boldsymbol{u}} \cdot \nabla \overline{P} + \nabla \cdot \left[\overline{\rho}\left\{EFD_h + (1-\Omega)D_t\right\}\nabla \widetilde{h}\right] + \boldsymbol{t} \colon \nabla \widetilde{\boldsymbol{u}} + S_{\rho h}, \tag{3.3}$$

$$\frac{\partial \overline{\rho}\widetilde{Y_k}}{\partial t} + \nabla \cdot (\overline{\rho}\widetilde{Y_k}\widetilde{\boldsymbol{u}}) = \nabla \cdot \left[\overline{\rho}\left\{EFD_k + (1-\Omega)D_t\right\}\nabla \widetilde{Y_k}\right] + \frac{E}{F}S_{comb,k} + S_{\rho Y_k}, \tag{3.4}$$

Here, the overbar $\bar{}$ denotes the filtered mean value of the physical quantity in the gird scale for LES, and the tilde $\tilde{}$ denotes the Favre-averaged value. Each value ρ, P, h, Y_k, T is density, pressure, enthalpy, mass fraction of species k, and temperature, respectively. $\boldsymbol{u}$ is velocity, and $\boldsymbol{t}$ is stress tensor considering sub-grid scale (SGS) stress. Each D_h, D_k, and D_t is thermal diffusivity, the mass diffusion coefficient of species k, which is given under the unity Lewis number assumption and turbulence diffusion coefficient, and turbulence diffusion coefficient, respectively. The value D_h and D_k are expressed as $\rho D_h = \lambda / c_p$ and $\rho D_k = \lambda / c_p$, and here, λ is heat conductivity and c_p is specific heat capacity. These SGS terms are calculated using the Dynamic Smagorinsky model [11, 12]. The effect of combustion product is taken into account as $S_{comb,k}$. Ω is the flame sensor [13–15] defined as

$$\Omega = \tanh\left(\alpha \frac{q}{q_{max}}\right). \tag{3.5}$$

Here, q is the heat release rate at each local position, and q_{max} is the maximum heat release rate estimated in the one-dimensional simulation of laminar flame. α is the parameter that controls the thickness of the flame surface and is set to 10. E is the

efficiency function, which adjusts the flame speed considering the effects of SGS turbulence on the reaction, and F is the flame thickening factor, which artificially thickens the flame and makes the flame surface thick enough to resolve it on the LES grid [13–17]. The E and F are calculated based on the following procedure.

$$F = (F_{max} - 1)\Omega + 1, \tag{3.6}$$

$$E = (E_{max} - 1)\Omega + 1, \tag{3.7}$$

$$E_{max} = \left\{ 1 + \min\left(\frac{\Delta}{\delta_l^0} - 1, \Gamma \frac{u'_\Delta}{s_l^0} \right) \right\}, \tag{3.8}$$

$$\Gamma = \left[\left\{ \left(f_u^{-a} + f_\Delta^{-a} \right)^{-1/a} \right\}^{-b} + f_{Re}^{-b} \right]^{-1/b}, \tag{3.9}$$

$$f_u = 4 \left(\frac{27 C_k}{110} \right)^{1/2} \left(\frac{18 C_k}{55} \right) \left(\frac{u'_\Delta}{s_l^0} \right)^2, \tag{3.10}$$

$$f_\Delta = \left[\frac{27 C_k \pi^{4/3}}{110} \left\{ \left(\frac{\Delta}{\delta_l^0} \right)^{4/3} - 1 \right\} \right]^{1/2}, \tag{3.11}$$

$$f_{Re} = \left\{ \frac{9}{55} \exp\left(-\frac{3}{2} C_k \pi^{4/3} Re_\Delta^{-1} \right) \right\}^{1/2} Re_\Delta^{1/2}, \tag{3.12}$$

$$\begin{aligned} a = 0.60 &+ 0.20 \exp\left\{ -0.1 \left(\frac{u'_\Delta}{s_l^0} \right) \right\} \\ &- 0.20 \exp\left\{ -0.01 \left(\frac{\Delta}{\delta_l^0} \right) \right\}, \end{aligned} \tag{3.13}$$

$$b = 1.4\ . \tag{3.14}$$

Here, $F_{max} = 12$ is the maximum flame thickening coefficient and set to be the same as the previous study [5, 9]. Δ, δ_l^0, s_l^0, u'_Δ, Re_Δ, and C_k are the filter size, the laminar flame thickness, the laminar flame speed, the SGS turbulent velocity, SGS Reynolds number, and the Kolmogorov constant respectively [13–17].

The interaction of fuel droplet and gas flow is considered with S_ρ, $S_{\rho u}$, $S_{\rho h}$ and $S_{\rho Y_k}$, and each of them is calculated as

$$S_\rho = -\frac{1}{\Delta V} \sum_N \frac{dm_d}{dt}, \tag{3.15}$$

$$S_{\rho u} = -\frac{1}{\Delta V}\sum_{N}\frac{dm_d \boldsymbol{u}_d}{dt}, \tag{3.16}$$

$$S_{\rho h} = -\frac{1}{\Delta V}\sum_{N}\frac{dm_d h_d}{dt}, \tag{3.17}$$

$$S_{\rho Y_k} = -\frac{1}{\Delta V}\sum_{N}\frac{dm_d}{dt} \quad \text{for} \quad Y_k = Y_F. \tag{3.18}$$

Here, ΔV is the control volume for gas phase calculation, and N is the number of fuel droplets. m_d, $\boldsymbol{u}_d$ and h_d are droplets' mass, droplet velocity, and specific enthalpy of a fuel droplet, respectively.

Concerning the droplet motion, the governing equations for each droplet's position, $\boldsymbol{x}_d$, velocity, $\boldsymbol{u}_d$, temperature, T_d, and mass, m_d are expressed as

$$\frac{d\boldsymbol{x}_d}{dt} = \boldsymbol{u}_d, \tag{3.19}$$

$$\frac{d\boldsymbol{u}_d}{dt} = \frac{f_s}{\tau_d}(\boldsymbol{u} - \boldsymbol{u}_d), \tag{3.20}$$

$$\frac{dT_d}{dt} = \frac{Nu}{3Pr}\left(\frac{c_p}{c_{p,d}}\right)\left(\frac{f_t}{\tau_d}\right)(T - T_d) + \frac{\dot{m}_d}{m_d}\frac{L_V}{c_{p,d}}, \tag{3.21}$$

$$\frac{dm_d}{dt} = \dot{m}_d. \tag{3.22}$$

Here, T is the gas temperature, $c_{p,d}$ is the specific heat capacity of the droplet, and L_V is the latent heat of evaporation at T_d. The particle response time, τ_d, is defined by

$$\tau_d = \frac{\rho_d d^2}{18\mu}. \tag{3.23}$$

Here, ρ_d is the droplet density, μ is the viscosity, and d is the droplet diameter. The Prandtl and Nusselt numbers in the gas phase are given by

$$Pr = \frac{\mu}{\rho D_h}, \quad Nu = 2 + 0.552 Re_{sl}^{1/2} Pr^{1/3}. \tag{3.24}$$

Here, $Re_{sl} = \rho u_{sl} d/\mu$ is the droplet Reynolds number based on the slip velocity, $u_{sl} = |\boldsymbol{u} - \boldsymbol{u}_d|$. The calculation methods of corrections of the Stokes drag, f_s, and heat transfer for an evaporating fuel droplet, f_t, are given in Refs. [18–20].

3.2.2 Reaction model

In this study, kerosene (KERO), which is composed of $C_{10}H_{22}$ (76.7 wt%), C_9H_{12} (13.2 wt%) and C_9H_{18} (10.1 wt%) is used as fuel, and the two-step global reaction model proposed by Franzelli et al. [21] for kerosene flame is employed. The two-step chemical scheme comprises the following two reactions.

$$\mathrm{KERO} + 10\mathrm{O_2} \overset{\dot{\omega}_{f,1}}{\rightarrow} \mathrm{CO} + 10\mathrm{H_2O}, \tag{3.25}$$

$$\mathrm{CO} + \frac{1}{2}\mathrm{O_2} \underset{\dot{\omega}_{r,2}}{\overset{\dot{\omega}_{f,2}}{\rightleftarrows}} \mathrm{CO_2}. \tag{3.26}$$

Here, the forward reaction rate, $\dot{\omega}_{f,1}$, and $\dot{\omega}_{f,2}$, are expressed as

$$\dot{\omega}_{f,1} = A_1 f_1(\phi) \exp\left(-\frac{E_{a,1}}{RT}\right) [\mathrm{KERO}]^{n_{\mathrm{KERO}}} [\mathrm{O_2}]^{n_{\mathrm{O_2},1}}, \tag{3.27}$$

$$\dot{\omega}_{f,2} = A_2 f_2(\phi) \exp\left(-\frac{E_{a,2}}{RT}\right) [\mathrm{CO}]^{n_{\mathrm{CO}}} [\mathrm{O_2}]^{n_{\mathrm{O_2},2}}. \tag{3.28}$$

T is gas temperature, R is gas constant, ϕ is the local equivalence ratio, and [X] is mol concentration of species X. A is the pre-exponential factor, E_a is activation energy of reaction, n_{KERO}, n_{CO}, $n_{\mathrm{O_2}}$ is the reaction exponent for each reaction, and these values used in this study are summarized in Table 3.1. $f\,(\phi)$ is the correction function, in which the variable is local equivalence ratio, ϕ, and expressed as

$$f_1\,(\phi) = \frac{2}{\left[1 + \tanh\left(\frac{\phi_{0,1}-\phi}{\sigma_{0,1}}\right)\right] + B_1\left[1 + \tanh\left(\frac{\phi-\phi_{1,1}}{\sigma_{1,1}}\right)\right] + C_1\left[1 + \tanh\left(\frac{\phi-\phi_{2,1}}{\sigma_{2,1}}\right)\right]}, \tag{3.29}$$

$$\begin{aligned} f_2(\phi) \;&= \tfrac{1}{2}\left\{1 + \tanh\left(\tfrac{\phi_{0,2}-\phi}{\sigma_{0,2}}\right)\right\} + \tfrac{B_2}{2}\left\{1 + \tanh\left(\tfrac{\phi-\phi_{1,2}}{\sigma_{1,2}}\right)\right\} \\ &\quad + \tfrac{C_2}{2}\left\{1 + \tanh\left(\tfrac{\phi-\phi_{2,2}}{\sigma_{2,2}}\right)\right\}\left\{1 + \tanh\left(\tfrac{\phi_{3,2}-\phi}{\sigma_{3,2}}\right)\right\}. \end{aligned} \tag{3.30}$$

Each value in Eqs. (3.29) and (3.30) are summaraized in Table 3.2.

The reverse reaction rate, $\dot{\omega}_{r,2}$, is calculated using equilibrium constant, K_c, as

$$\dot{\omega}_{r,2} = A_2 f_2(\phi) \exp\left(-\frac{E_{a,2}}{RT}\right) \frac{1}{K_c} [\mathrm{CO_2}]. \tag{3.31}$$

Here, K_c is calculated as,

$$\frac{1}{K_c} = C^{-\Delta\nu} \exp\left(\frac{\Delta G^\circ}{RT}\right), \tag{3.32}$$

where C is the total mole concentration and $\Delta\nu = 1/2$ is the mole number change. ΔG° is the change in the Gibbs free energy in the reaction calculated as

$$\Delta G^\circ = \Delta H - T\Delta S. \tag{3.33}$$

Here, ΔH and ΔS are the changes in the enthalpy and the entropy in the reaction, respectively.

The source term due to the combustion reaction is described as

$$S_{comb,k} = -W_k \left(\frac{n_{k,1}}{n_{KERO}}\dot{\omega}_{f,1} + \frac{n_{k,2}}{n_{\mathrm{CO}}}(\dot{\omega}_{f,2} - \dot{\omega}_{r,2})\right). \tag{3.34}$$

Here, n_k and n_F are the molar stoichiometric coefficients of the species k and the fuel. W_k is the molecular weight of the species k.

Table 3.1: Pre-exponential factor, A_i, activation energy, $E_{a,i}$, and reaction exponent, n, in Eqs. (3.27) and (3.28).

	$i = 1$	$i = 2$
A_i	8.0×10^{11}	4.5×10^{10}
$E_{a,i}$	4.15×10^4	2.0×10^4
n	$n_{\mathrm{KERO}} = 0.55$	$n_{\mathrm{CO}} = 1.00$
	$n_{\mathrm{O_2},1} = 0.90$	$n_{\mathrm{O_2},2} = 0.50$

Table 3.2: Coefficients for correction functions of f_1 and f_2 in Eqs. (3.29) and (3.30).

	$\phi_{0,j}$	$\sigma_{0,j}$	B_j	$\phi_{1,j}$	$\sigma_{1,j}$	C_j	$\phi_{2,j}$	$\sigma_{2,j}$	$\phi_{3,j}$	$\sigma_{3,j}$
$j=1$	1.173	0.04	0.29	1.2	0.02	7.1	1.8	0.18	-	-
$j=2$	1.146	0.045	1.5×10^{-4}	1.2	0.04	0.035	1.215	0.03	1.32	0.09

3.2.3 Evaporation model

The evaporation of fuel droplets is replicated by a non-equilibrium Langmuir-Knudsen evaporation model [19, 22, 23]. In this study, the effect of the temperature gradient inside the droplet is neglected. The evaporation rate is given as

$$\dot{m}_d = -\frac{m_d}{\tau_d}\left(\frac{Sh}{3Sc}\right)\ln(1+B_M), \tag{3.35}$$

Here, Schmidt number, Sc, Sherwood number, Sh, and mass transfer number, B_M, are given as

$$Sc = \frac{\mu}{\rho D_k}, \quad Sh = 2 + 0.552 Re_{sl}^{1/2} Sc^{1/3}. \tag{3.36}$$

$$B_M = \frac{Y_{F,s} - Y_F}{1 - Y_{F,s}}. \tag{3.37}$$

Here, Y_F is the mass fraction of fuel vapor, and $Y_{F,s}$ is the vapor surface mass fraction, which is given as

$$Y_{F,s} = \frac{X_{F,s}}{X_{F,s} + (1 - X_{F,s})\overline{W}/W_F}, \tag{3.38}$$

$$X_{F,s} = \frac{P_{sat}}{P} - \left(\frac{2L_K}{d}\right)\beta. \tag{3.39}$$

Here, $X_{F,s}$ is the mole fraction of fuel vapor at the droplet surface, P_{sat} is the saturated vapor pressure, P is the ambient pressure, $\overline{W}$ and W_F are the averaged molecular weight of the carrier gas and the molecular weight of the fuel vapor, respectively. L_K and β are Knudsen layer thickness and non-dimensional evaporation parameters, which are given as

$$L_K = \frac{\mu\left\{2\pi T_d (R/W_F)\right\}^{1/2}}{ScP}. \tag{3.40}$$

$$\beta = -\left(\frac{3Pr\tau_d}{2}\right)\frac{\dot{m}_d^2}{m_d}, \tag{3.41}$$

Here, R is the universal gas constant. The saturated vapor pressure, P_{sat}, is given as

$$P_{sat} = P \exp\left\{ \frac{L_V W_F}{R} \left(\frac{1}{T_B} - \frac{1}{T_d} \right) \right\}. \tag{3.42}$$

Here, T_B and L_V are boiling temperature and vaporization heat, and L_V is estimated by using Watson equation [24] as

$$L_V = L_{V,B,atm} \left(\frac{T_c - T_d}{T_c - T_{B,atm}} \right)^{0.38}. \tag{3.43}$$

Here $L_{V,B,atm}$ is the latent heat at normal boiling temperature, $T_{B,atm}$ is normal boiling temperature, and T_c is the critical temperature.

3.2.4 Atomization model

Under the condition of combustion instability, pressure oscillation causes velocity fluctuation, and it could affect the fuel atomization. Therefore, in this study, to consider the effect of the interaction of atomization and combustion instability, the atomization model proposed by Lee et al. [25] is adopted. This model is theoretically derived from the mass and energy equation and is used to calculate the Sauter Mean Diameter (SMD). The definition of SMD is

$$SMD = \frac{\sum_{i=1}^{n} {d_i}^3}{\sum_{i=1}^{n} {d_i}^2}, \tag{3.44}$$

Here, d_i is the diameter of each droplet, and n is the number of droplets. Lee's model is expressed as

$$SMD = \frac{3\sigma + \sqrt{9\sigma^2 + K \frac{\mu_L \overline{u}_{L,2}^2}{\overline{v}_{L,inj}} \left(\frac{1}{2}\rho_L \left(\overline{v}_{L,inj}^2 - \overline{u}_{L,2}^2 \right) + \frac{Ac}{\overline{v}_{L,inj} A_{inj}} \frac{1}{2} \rho_{g,1} \left(\overline{u}_{g,1}^3 - \overline{u}_{g,2}^3 \right) \right)}}{\left(\frac{1}{2}\rho_L \left(\overline{v}_{L,inj}^2 - \overline{u}_{L,2}^2 \right) + \frac{Ac}{\overline{v}_{L,inj} A_{inj}} \frac{1}{2} \rho_{g,1} \left(\overline{u}_{g,1}^3 - \overline{u}_{g,2}^3 \right) \right)}, \tag{3.45}$$

$$Ac = \left[3.44 d_{inj} \sqrt{\frac{\rho_L \overline{v}_{L,inj}^2}{\rho_{g,1} \overline{u}_{g,1}^2}} \right] \times \left[7.86 d_{inj} \left(\frac{\rho_L \overline{v}_{L,inj}^2}{\rho_{g,1} \overline{u}_{g,1}^2} \right)^{0.17} \times 8.06^{0.33} \right], K = 0.1. \tag{3.46}$$

Here, $\rho_{g,1}$ is upstream plane averaged gas density, $\overline{u}_{g,1}$ is upstream plane averaged gas speed, $\overline{u}_{g,2}$ is downstream plane averaged gas speed σ is surface tension of fuel droplet,

μ_L is viscosity coefficient of fuel, ρ_L is fuel density, $\overline{v}_{L,inj}$ is the fuel injection speed, and $\overline{u}_{L,2}$ is the downstream droplet speed. A_{inj} is the cross-section area of injector, d_{inj} is the injector diameter, and K is the fitting parameter.

3.2.5 Computational setup

Figure 3.1 shows the computational domain of only the combustor and conditions for spray combustion, and the computational domain for the whole region, including the inflow region and outflow region, is almost the same as the previous study (refer to Fig.1 in previous study [5]). In the combustor, the mesh has 230 grid points in x direction, 80 grid points in y direction, and 80 grid points in z direction. Moreover, in the whole computational domain, including the inflow and outflow region, the mesh has 1120 grid points in x direction, 160 grid points in y direction, and 120 grid points in z direction. Air is injected from the inlet, and fuel (KERO) is injected into the combustor from positions situated 5 mm upstream of the back step, with a velocity of 2 m/s. The injected droplet size distribution is calculated with a modified Nukiyama-Tanazawa function [26] that requires SMD calculated by the atomization model mentioned above as a parameter. The initial air temperature is set as 760 K, the initial pressure is set to the atmospheric pressure of 0.1 MPa, and the initial temperature of injected fuel droplets is 300 K. The equivalence ratio of the 3 cases investigated in this study varies from 1.0 to 0.6 (i.e., Φ = 1.0, 0.8 and 0.6). The equivalence ratio for each case is defined based on the fuel injection rate and the initial air mass flow rate (which is the same among all 3 cases). The value of pressure under the combustion instability is investigated at 3 mm just above the step at the center plane, and the value of the heat release rate is represented by the integral of the whole domain in the combustor. The LESs are performed using an in-house code FK^3 [5, 27, 28] with the finite difference formulation in the Cartesian coordinate system. There are approximately 2.4 million grid points within the combustor, while the total number of grid points in the entire computational domain is about 21.5 million. The minimum grid size is about 0.1 mm, and the reliability of the grid resolution for pressure and heat release oscillations was

validated by performing LES with double coarser grid resolution. The physical time for each case is about 730 hours for $\Phi = 1.0$ and $\Phi = 0.8$ and 1460 hours for $\Phi = 0.6$ by parallel computation using 1024 cores on a CRAY-XC40 supercomputer at the Academic Centre for Computing and Media Studies (ACCMS), Kyoto University. These computational time differences derive from the unsteady oscillation at $\Phi = 0.6$. For $\Phi = 0.8$ and 1.0, after the amplitude of pressure grows, the amplitude is almost constant, and then the statistical data is collected. However, for $\Phi = 0.6$, after the amplitude grows, the amplitude is not constant but gets smaller sometimes. In order to confirm if this trend is going to be observed repeatedly or not, the simulation is continued to see at least two of the same trend. This is why only the case for $\Phi = 0.6$ takes so long time.

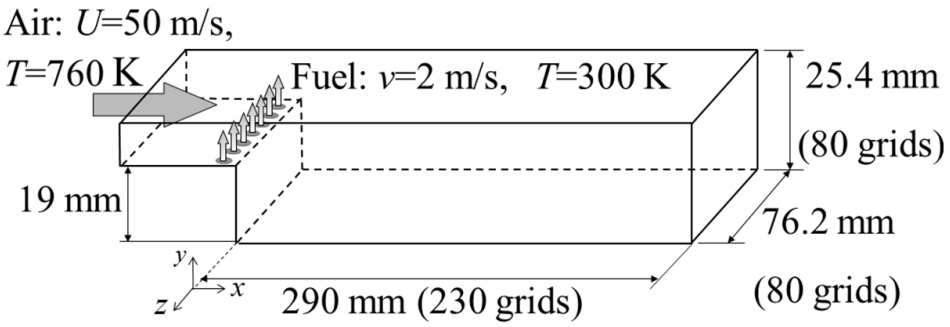

Figure 3.1: Schematic of the computational domain of combustor and conditions

3.3 Results and discussion

3.3.1 Pressure oscillation under combustion instability

This section investigates the effect of the equivalence ratio on the behavior of combustion instability.

Figure 3.2 shows the external view of the combustor under combustion instability at $\Phi = 1.0$. The flame is represented by the red surface, which is the isothermal surface of 1800 K, and fuel droplets are represented by green dots. It is observed that the droplets

flow downstream with air inflow and get burned.

For all equivalence ratios, combustion instability is observed; however, the behavior of pressure oscillation varies among them. The time variations of pressure, P, at each equivalence ratio are shown in Fig. 3.3. "*Time Gap*" in this figure is discussed in the next section. Here, only for $\Phi = 0.6$, the time range is longer than the others, and this is because to capture the peculiar phenomena observed only at $\Phi = 0.6$. In all cases, the pressure oscillates periodically, and the amplitude of pressure oscillation is in the range of approximately 2-10 % of the ambient pressure. At $\Phi = 1.0$, the pressure oscillates stably, and the amplitude is almost constant. At $\Phi = 0.8$, the amplitude varies slightly, but it is almost constant, like $\Phi = 1.0$. However, at $\Phi = 0.6$, the amplitude is not constant and exhibits repeated small and large variations. This unique phenomenon is not observed for other equivalence ratios, and this fluctuating amplitude was also observed in some experimental studies [2, 3]. However, the detailed mechanism for this phenomenon is not still fully elucidated.

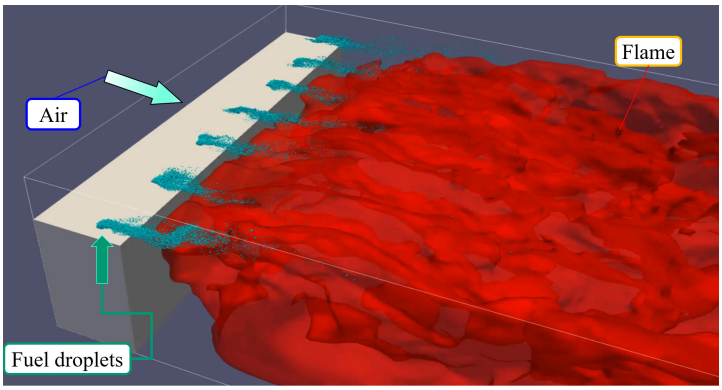

Figure 3.2: External view of combustor under combustion instability at $\Phi = 1.0$

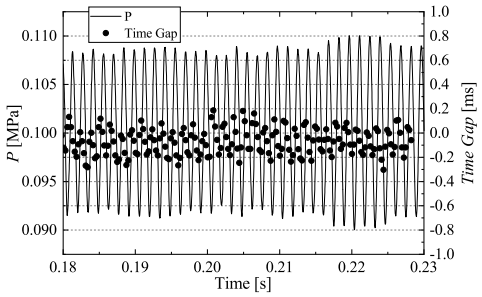

(a) $\Phi = 1.0$

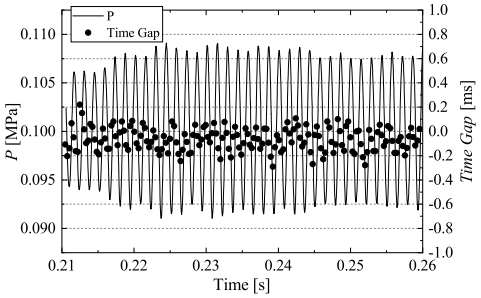

(b) $\Phi = 0.8$

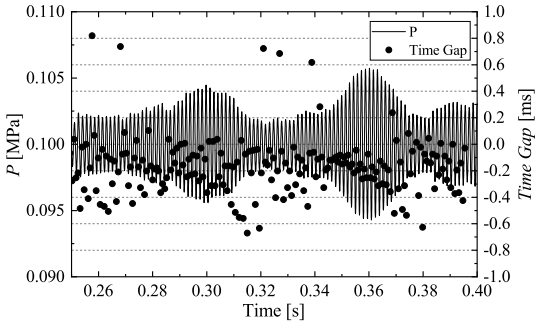

(c) $\Phi = 0.6$

Figure 3.3: Time variation of *Time Gap* and pressure, P, at each equivalence ratio.

3.3.2 Time Gap

As mentioned above, at $\Phi = 0.6$, the amplitude of pressure oscillation fluctuates with a lower frequency than the frequency of pressure oscillation. It is known that the characteristics of combustion instability are mainly determined by pressure, heat release rate, and their correlation. Therefore, as an index to determine the degree of correlation, the Rayleigh Index (RI) is often adopted. This index shows the spatial correlation between pressure and heat release rate, but it is not easy to investigate the time variation of correlation. At $\Phi = 0.6$, the amplitude of pressure oscillation varies with time, and there should be a time variation of correlation between pressure and heat release rate. To understand the time variation of the correlation, the quantity "*Time Gap*" is proposed as an index, and its time variation is analyzed. The *Time Gap* is calculated as follows, and Fig. 3.4 shows the conceptual diagram of *Time Gap* calculation. First, the cross-correlation of the pressure and the heat release rate for a certain time range is calculated as

$$Cross(\tau) = \int_{t_0}^{t_0+t_p} P'(t+\tau)q'(t)dt. \tag{3.47}$$

Here, P' and q' are variations of pressure and heat release rate, respectively, and t_p is the one cycle time of pressure oscillation. τ is the imaginary time delay of pressure from the original pressure, and τ varies from $-t_p/2$ to $t_p/2$ to evaluate at least one cycle time of pressure oscillation. The value of cross-correlation represents to what extent the oscillation of imaginary time delayed pressure and the fluctuation of heat release rate overlap, and this value is changed with varying τ because the phase difference between pressure and heat release rate changes. After the calculation of the cross-correlation, among the τ that provides the maximum value of $Cross(\tau)$, the one closest to zero is defined as the *Time Gap*. Here, maximum $Cross(\tau)$ means that the oscillation of pressure and heat release rate most closely overlap, and τ that gives maximum $Cross(\tau)$ represents how close the phase of original pressure and heat release rate is. Therefore, the smaller τ means the closer phase difference between pressure and heat release rate. The reason to choose the τ closest to zero is to consider only one cycle time. For example,

when the pressure has a maximum value at the phase when the heat release rate has a minimum value, $Cross(\tau)$ could have two maximum values with τ being about $\pm t_p/2$.

By using this technique, the *Time Gap* are calculated, and Fig. 3.3 shows the time variations of the *Time Gaps* and pressure oscillation for each equivalence ratio. At $\Phi = 1.0$ and $\Phi = 0.8$, *Time Gap* does not vary and falls between 0.0 and -0.2 ms.

However, focusing on $\Phi = 0.6$, *Time Gap* varies with time, and when the amplitude of pressure gets the maximum, *Time Gap* lies between 0.0 and -0.2 ms, and when the amplitude gets minimum, *Time Gap* has a wide time range and at maximum it reaches -0.8 ms. Along with the time variation of *Time Gap*, the amplitude of pressure oscillation fluctuates. Moreover, *Time Gap* lies between 0.0 and -0.2 ms before amplitude gets maximum value again. This implies that the pressure oscillation is increased with the concentrated correlation between pressure and heat release rate. Here, the time variation of *Time Gap* proceeds to the time variation of the amplitude of pressure oscillation, so this index could be used to predict the occurrence of combustion instability.

Moreover, the *Time Gap* is approximately between 0.0 and -0.2 ms when it is in the narrower range, which implies that when the phase of pressure slightly delays the phase of heat release rate, the correlation gets stronger, and it is not the time when the phase of pressure completely matches the phase of heat release rate, which means the *Time Gap* is 0.0 ms.

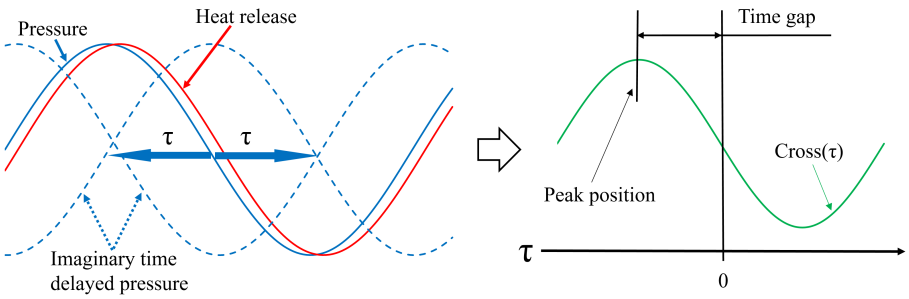

Figure 3.4: Conceptual diagram of *Time Gap* calculation.

3.3.3 Correlation of pressure and heat release rate

The amplitude of pressure oscillation fluctuates for $\Phi = 0.6$, and the characteristics of combustion instability must be different for each amplitude; therefore, based on the amplitude of pressure oscillation, the series of oscillation phenomenon is partitioned into four-time intervals: a, b, c, d, and the characteristics of combustion instability are investigated in detail in each time interval. Here, each time interval is approximately 0.01 s long, as shown in Fig. 3.5.

To investigate the spatial correlation of pressure and heat release rate among different time intervals, RI is shown in Fig. 3.6. RI is calculated as,

$$RI = \frac{1}{t_s} \int \frac{P'q'}{P_{ave}Q_{ave}} \, dt. \tag{3.48}$$

Here, P is pressure, Q is heat release rate, t_s is the sampling time, dash, ‘, represents the variation, and ave represents the averaged value. The region where RI is positive represents the region where combustion instability is encouraged, and vice versa. As the figure shows, the positive area is larger in the time intervals b and d than in the time intervals a and c, and the maximum RI value is also higher. This difference in RI distribution is one reason for the difference in the amplitude of pressure oscillation. At approximately $x = 30$ mm, strong positive regions are distributed for all time intervals, but the positive RI area of time intervals b and d is distributed more upstream than that of time intervals a and c.

To investigate the difference of the RI distribution, firstly, Fig. 3.7 shows the streamwise distributions of time-averaged pressure for each time interval. Here, the values only when the pressure at the measuring point (x = -3 mm) is more than ambient pressure are used for the average to visualize its amplitude at each axial position. The position of transition from low pressure to high pressure is the same for all time intervals; only the magnitudes differ. Around the back step, there is an antinode of pressure oscillation, and around the exit of the combustor, there is a node.

Second, as another factor affecting RI distribution, Fig. 3.8 shows the streamwise distribution of the time interval's averaged and cross-sectional averaged heat release rate.

From this figure, it can be seen that the peaks of the heat release rate of time intervals b and d, i.e., the time intervals with larger amplitudes of pressure oscillation, are bigger than those of the heat release rate of time intervals a and c, i.e., the time intervals with smaller amplitudes of pressure oscillation. Additionally, the peak heat release rate positions of time intervals b and d lie further upstream than those of time intervals a and c, and their second peak lies in the downstream region. Considering the pressure, the upstream region of the combustor is the antinode of pressure oscillation; therefore, when the distributions of heat release rate shift upstream, regions of high pressure and high heat release rate overlap and it increases the RI at the upstream region ($x = 30$ mm).

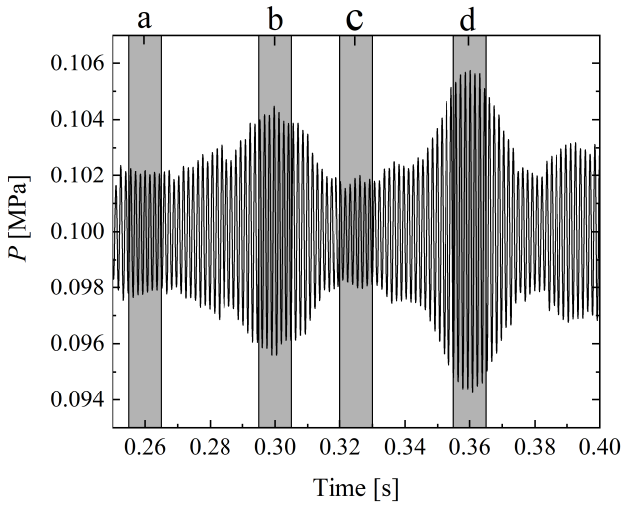

Figure 3.5: The definition of each time interval; a, b, c, d for $\Phi = 0.6$.

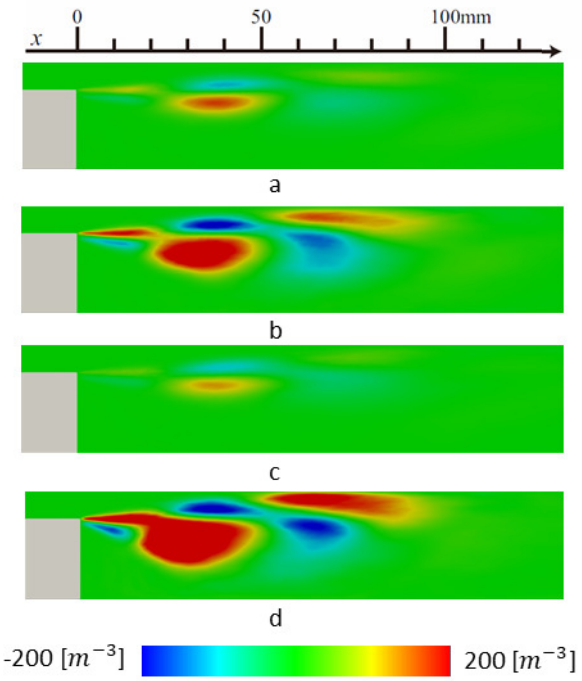

Figure 3.6: Comparison of distributions of spanwise-averaged local Rayleigh Index on the x-y plane among each time interval a, b, c and d for $\Phi = 0.6$.

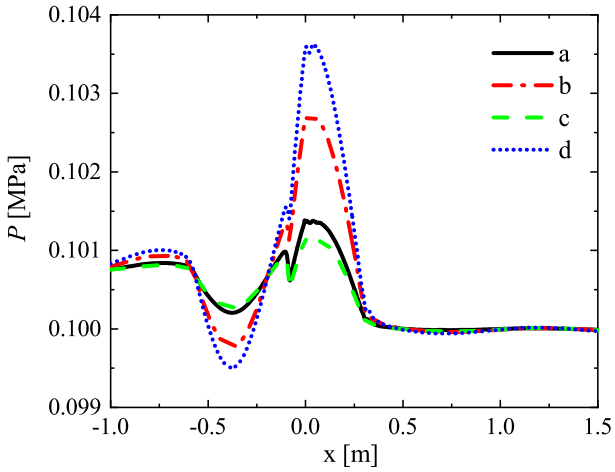

Figure 3.7: Comparison of streamwise distributions of time interval-averaged local pressure, P, among each time interval a, b, c and d for $\Phi = 0.6$.

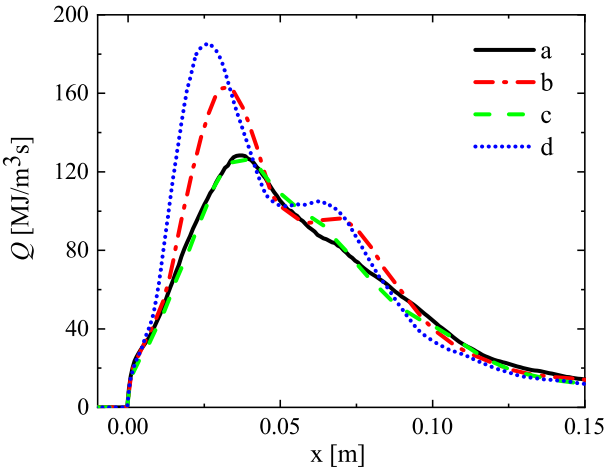

Figure 3.8: Comparison of streamwise distributions of time interval- and cross-sectional (y-z)-averaged local heat release rate, Q, among each time interval a, b, c and d for $\Phi = 0.6$.

3.3.4 Upstream transition of heat release rate

To clarify the reason as to why the heat release rate shifts upstream during time intervals b and d, the streamwise distributions of time-averaged and cross-sectional averaged evaporation rate, and the $x-y$ plane instantaneous distributions of heat release rate at the phase $\phi = 180°$, which is defined as the time instance when pressure has maximum value, are shown in Fig. 3.9 and Fig. 3.10, respectively. Figure 3.9 shows that the distributions of the evaporation rate do not change appreciably among the different time intervals, which implies that the distributions of the evaporation rate do not affect the transition of the heat release rate. The reason why the distributions of evaporation do not change can be explained by the inlet droplet size distribution and the position where droplets get evaporated. Figure 3.11 shows the time-averaged Probability Density Function (PDF) at each time interval. As this figure shows, the inlet droplet size distributions do not change at each time interval. Concerning the position where droplets get evaporated, most droplets evaporate at $x < 20$ mm, and the shapes of the flame at $x < 20$ mm are almost the same at each time interval. Only the flame shapes behind the back step change drastically at $x > 20$ mm at each time interval due to the different vortex fluctuations, as shown in Fig. 3.10. Considering the same inlet droplet size distributions and the same positions of evaporation, it is natural to acquire the same evaporation distributions among each time interval, and based on the discussion above, it is clear that the evaporation does not affect the upstream transition of the heat release rate.

When the flame shapes shown in Fig. 3.10 are compared, during time intervals b and d, the spatial distribution of the heat release rate flaps up and down and is concentrated around $x = 20$ to 30 mm. These different motions of flame shape can affect the upstream shift of the heat release rate. In order to investigate this, $x-y$ plane instantaneous distributions of fuel mass fraction and heat release rate at different phases of time interval d are shown in Fig. 3.12. At the phase $\phi = 0°$, when the pressure has a minimum value, the fuel mass fraction stretches along the downstream direction, and as a result, the heat release rate is distributed in a similar manner to the fuel mass fraction. Subsequently, with increasing pressure, the distribution of fuel mass fraction separates

into two regions, upstream and downstream. Then, at $\phi = 180°$, when the pressure has a maximum value, the upstream fuel is pushed back further upstream, and the downstream fuel diffuses further downstream. Consequently, because the distribution of the fuel mass fraction is shorter than that at $\phi = 0°$, the heat release rate has a high value locally in the upstream region of the chamber. Above $\phi = 180°$, with a decrease in pressure, fuel that was congested upstream expands downstream with swirling and is burned; therefore, considerable heat is released in the entire combustion chamber. This phenomenon, congestion, diffusion, and combustion, which are recognized as heat fluctuation, are hardly observed at time intervals a and c; it is the underlying mechanism of the upstream transition of the heat release rate.

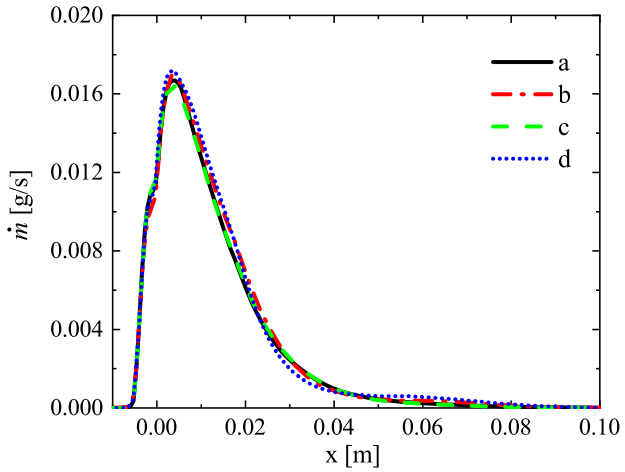

Figure 3.9: Comparison of streamwise distributions of time interval- and cross-sectional (y-z)-averaged local evaporation rate, $\dot{m}$, among each time interval a, b, c and d for $\Phi = 0.6$.

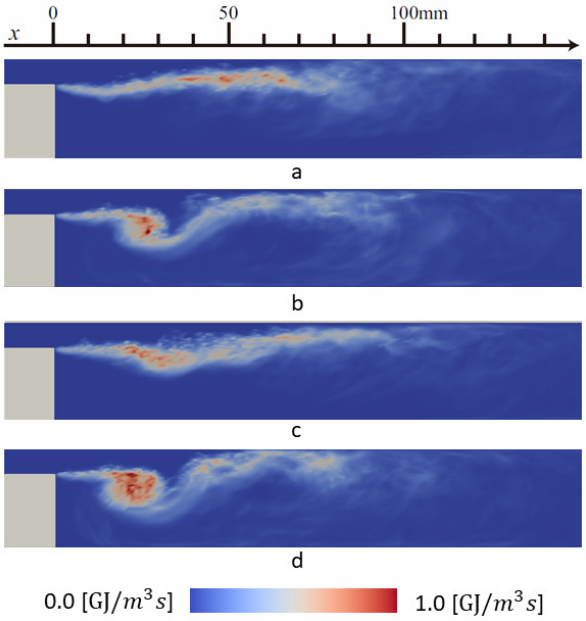

Figure 3.10: Comparison of instantaneous distributions of heat release rate on the x-y plane at the phase of 180°($P = P_{max}$) among each time interval a, b, c and d for $\Phi = 0.6$.

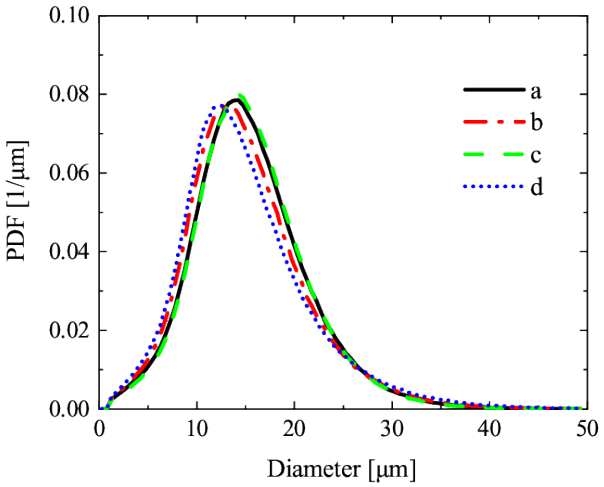

Figure 3.11: Comparison of time interval averaged PDF, among each time interval a, b, c and d for $\Phi = 0.6$.

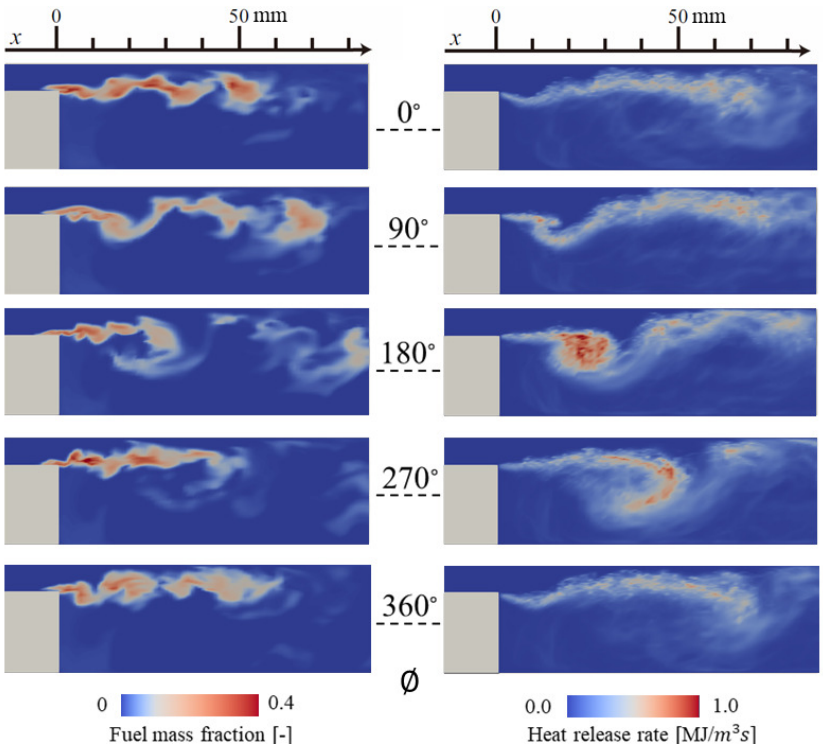

Figure 3.12: Comparison of instantaneous distributions fuel mass fraction and heat release rate on the x-y plane among different phases of time interval d.

3.4 Conclusions

In this study, combustion instability of spray combustion in a combustion chamber with a back-step was investigated using LES employing a dynamic thickened flame model. In this setup, three equivalence ratios (Φ = 1.0, 0.8, and 0.6) were simulated. The combustion instability was observed in all of the cases, and the intensity of combustion instability decreased with a decrease in the equivalence ratio. This is mainly because whole heat energy decreased with the decreasing amount of fuel injected into the combustor, and unstable combustion phenomena such as blow-off did not occur in this setup. However, for the lowest equivalence ratio of Φ = 0.6, the amplitude of the pressure oscillation fluctuated temporally, and its tendency was quite different from that observed under combustion instability, keeping a certain amplitude of pressure oscillation as for Φ = 0.8 and 1.0. In order to investigate the time variations of correlation, a new index "*Time Gap*" was proposed and confirmed useful. With using *Time Gap*, it was elucidated that when the phase difference between pressure and heat release rate got shorter, the pressure oscillation got stronger, and vice versa. In addition, it was also observed that, when the phase difference got longer, the flame structure was stable without fluctuating, and when the phase difference got shorter, the flame structure began to fluctuate and made the spatial distribution of heat release rate vary with time. Because of these temporal and spatial fluctuations of heat release rate, which induced the time variation of the correlation between pressure and heat release rate, the amplitude of pressure oscillation temporally fluctuated.

References

[1] L. Rayleigh. The explanation of certain acoustical phenomena. *Nature*, 18:319–321, 1878.

[2] H. Gotoda, H. Nikimoto, T. Miyano, and S. Tachibana. Dynamic properties of combustion instability in a lean premixed gas-turbine combustors. *Chaos*, 21:013124, 2011.

[3] L. Kabiraj, A. Saurabh, P. Pankaj, and R. I. Sujith. Route to chaos for combustion instability in ducted laminar premixed flame. *Chaos*, 22:023129, 2012.

[4] S. Tachibana, K. Saito, T. Yamamoto, M. Makida, T. Kitano, and R. Kurose. Experimental and numerical investigation of thermo-acoustic instability in a liquid-fuel aero-engine combustor at elevated pressure: Validity of large-eddy simulation of spray combustion. *Combustion and Flame*, 162(6):2621–2637, 2015.

[5] T. Kitano, K. Kaneko, R. Kurose, and S. Komori. Large-eddy simulations of gas- and liquid-fueled combustion instabilities in back-step flows. *Combustion and Flame*, 170:63–78, 2016.

[6] K. Sato, E. Knudsen, and H. Pitsch. Study of combustion instabilities imposed by inlet velocity disturbance in combustor using les. *ASME Turbo Expo 2009: Power for Land, Sea, and Air*, 2:87–99, 2009.

[7] P. Wolf, G. Staffelbach, L. Y. Gicquel, J.-D. Muller, and T. Poinsot. Acoustic and large eddy simulation studies of azimuthal modes in annular combustion chambers. *Combustion and Flame*, 159(11):3398–3413, 2012.

[8] B. Franzelli, E. Riber, L. Gicquel, and T. Poinsot. Large eddy simulation of combustion instabilities in a lean partially premixed swirled flame. *Combustion and Flame*, 159(2):621–637, 2012.

[9] A. Pillai, J. Nagao, R. Awane, and R. Kurose. Influences of liquid fuel atomization and flow rate fluctuations on spray combustion instabilities in a backward-facing step combustor. *Combustion and Flame*, 220:337–356, 2020.

[10] V. Moureau, C. Bérat, and H. Pitsch. An efficient semi-implicit compressible solver for large-eddy simulations. *Journal of Computational Physics*, 226(2):1256–1270, 2007.

[11] P. Moin, K. Squires, W. Cabot, and S. Lee. A dynamic subgrid-scale model for compressible turbulence and scalar transport. *Physics of Fluids*, 3(11):2746–2757, 1991.

[12] C. Pierce and P. Moin. A dynamic model for subgrid-scale variance and dissipation rate of a conserved scalar. *Physics of Fluids*, 10(12):3041–3044, 1998.

[13] P. A. Strakey and G. Eggenspieler. Development and validation of a thickened flame modeling approach for large eddy simulation of premixed combustion. *Journal of Engineering for Gas Turbines and Power*, 132(7):071501, 2010.

[14] F. Charlette, C. Meneveau, and D. Veynante. A power-law flame wrinkling model for LES of premixed turbulent combustion Part I: non-dynamic formulation and initial tests. *Combustion and Flame*, 131(1):159–180, 2002.

[15] J.-P. Légier, T. Poinsot, and D. Veynante. Dynamically thickened flame LES model for premixed and non-premixed turbulent combustion. *Proceedings of the summer program*, 157–168, 2000.

[16] F. Proch and A. M. Kempf. Numerical analysis of the Cambridge stratified flame series using artificial thickened flame LES with tabulated premixed flame chemistry. *Combustion and Flame*, 161(10):2627–2646, 2014.

[17] A. Rittler, F. Proch, and A. M. Kempf. LES of the Sydney piloted spray flame series with the PFGM/ATF approach and different sub-filter models. *Combustion and Flame*, 162(4):1575–1598, 2015.

[18] M. Nakamura, F. Akamatsu, R. Kurose, and M. Katsuki. Combustion mechanism of liquid fuel spray in a gaseous flame. *Physics of Fluids*, 17(12):123301, 2005.

[19] R. S. Miller, K. Harstad, and J. Bellan. Evaluation of equilibrium and non-equilibrium evaporation models for many-droplet gas-liquid flow simulations. *International Journal of Multiphase Flow*, 24(6):1025–1055, 1998.

[20] R. Kurose, H. Makino, S. Komori, M. Nakamura, F. Akamatsu, and M. Katsuki. Effects of outflow from the surface of a sphere on drag, shear lift, and scalar diffusion. *Physics of Fluids*, 15(8):2338–2351, 2003.

[21] B. Franzelli, E. Riber, M. Sanjosé, and T. Poinsot. A two-step chemical scheme for kerosene–air premixed flames. *Combustion and Flame*, 157(7):1364–1373, 2010.

[22] J. Bellan and K. Harstad. Analysis of the convective evaporation of nondilute clusters of drops. *International Journal of Heat and Mass Transfer*, 30(1):125–136, 1987.

[23] R. S. Miller and J. Bellan. Direct numerical simulation of a confined three-dimensional gas mixing layer with one evaporating hydrocarbon-droplet-laden stream. *Journal of Fluid Mechanics*, 384:293–338, 1999.

[24] K. M. Watson. Thermodynamics of the liquid state. *Industrial & Engineering Chemistry*, 35(4):398–406, 1943.

[25] T.-W. Lee, J. Park, and R. Kurose. Determination of the drop size during atomization of liquid jets in cross flows. *Atomization and Sprays*, 28(3):241–254, 2018.

[26] P. González-Tello, F. Camacho, J. Vicaria, and P. González. A modified Nukiyama-Tanasawa distribution function and a Rosin-Rammler model for the particle-size-distribution analysis. *Powder Technology*, 3:278–281, 2008.

[27] T. Kitano, J. Nishio, R. Kurose, and S. Komori. Effects of ambient pressure, gas temperature and combustion reaction on droplet evaporation. *Combustion and Flame*, 161:551–564, 2014.

[28] R. Kurose. In-house code FK^3, available at. http://www.tse.me.kyoto-u.ac.jp/members/kurose/link_e.php, 2022. [accessed 15 May 2023].

Nomenclature

A	: Pre-exponential factor	Sc	: Schmidt number [-]
c_p	: Specific heat capacity [J/(K kg)]	Sh	: Sherwood number [-]
D	: Diffusion coefficient [m^2/s]	SMD	: Sauter Mean Diameter [μm]
d	: Droplet diameter [m]	T	: Temperature [K]
E	: Efficiency function [-]	$\boldsymbol{t}$	: SGS stress tensor [N/m^2]
E_a	: Activation energy [J/mol]	τ_d	: Particle response time [s]
F	: Flame thickening factor [-]	$\boldsymbol{u}$	: Velocity [m/s]
f	: Correction function [-]	W	: Mole weight [kg/mol]
G°	: Gibbs free energy [J/kg]	Y	: Mass fraction [-]
h	: Enthalpy [J/kg]	λ	: Thermal conductivity [W/(m K)]
L_V	: Latent heat of evaporation [J/kg]	ρ	: Density [kg/m^3]
m	: Mass [kg]	Φ	: Equivalence ratio [-]
$\dot{m}$	: Evaporation rate [kg/s]	ϕ	: Phase [$^\circ$]
n	: Reaction exponent [-]	$\dot{\omega}$	: Reaction rate [mol/s]
Nu	: Nusselt number [-]		
Ω	: Flame sensor [-]	**Subscripts**	
P	: Pressure [Pa]	*comb*	: Combustion
Pr	: Prandtl number [-]	d	: Droplet
q	: Heat release rate [J/s]	F	: Fuel
R	: Gas constant [J/(K mol)]	g	: Gas
Re	: Reynolds number [-]	k	: Species k
RI	: Local Rayleigh Index [-]	t	: Turbulent diffusion
S	: Source term		

Chapter 4

LES of combustion instability in a low-swirl combustor

4.1 Introduction

In this chapter, the mechanism of the flame-flow dynamics of a lean-premixed hydrogen flame in a low-swirl combustor (LSC) under combustion instability (CI) is investigated using LES.

Research aimed at elucidating and predicting CI have been undertaken both experimentally (e.g., [1–7]) and numerically (e.g., [8–14]) worldwide. Among these works, an interesting experimental study of CI in lean-premixed low-swirl hydrogen turbulent jet flames was conducted recently at the Japan Aerospace Exploration Agency (JAXA) [5, 6]. The low-swirl flame uses a simple flame-propagation phenomenon to maintain the flame, which has the advantage of maintaining combustion without blowing off over a wide range of turbulence intensity [15, 16]. Further, hydrogen fuel is also attracting interest as an alternative to fossil fuels that can be used in gas turbine engines in the future because of its extremely high heating value per unit mass, and because it does not emit CO_2 when burned. Therefore, although lean-premixed low-swirl hydrogen turbulent jet flames are expected to be an effective combustion method considering the benefits mentioned above, their detailed characteristics, particularly the flame behavior

under CI, are still not fully understood.

In the above-mentioned experiments [5, 6] on CI in lean-premixed low-swirl hydrogen turbulent jet flames, a pattern of flame-flow dynamics, which is considered to be unique to low-swirl hydrogen turbulent jet flames, was observed for the first time. Generally, in the LSCs, an inverted conical flame structure is commonly generated; however, under CI conditions, the flame structure of the lean-premixed hydrogen flame in the experiment [5, 6] periodically switched between a wide flat flame and an inverted conical flame. These flame dynamics are accompanied by the periodic outward and inward deflections of inflow with respect to the streamwise direction. The experimental study [5, 6] suggested that these periodic switching dynamics couple with the pressure oscillations, and occur in the CI. However, further simultaneous examinations using various physical quantities such as inflow velocities, pressure, gas temperature, and reaction rate in three-dimensions in the whole combustor, which are very hard to be obtained only in the experiments, need to be performed to support their investigations. In addition, information on the flow field in an upstream region is required because the periodic outward and inward deflections of the inflow are not only formed in the combustor but also affected by the phenomena in the upstream region from the region close to the swirler assembly to the injector exit.

Therefore, this chapter aims to elucidate the mechanism of the flame-flow dynamics of a lean-premixed hydrogen flame in an LSC under CI using LES, which considers the swirler assembly in the upstream region. The LES employing a dynamically thickened flame model [17–22] with a detailed chemical reaction model that comprises 9 chemical species and 20 reactions [23] is performed for the same configurations of the combustor and injector as those in the experiment [5, 6]. To capture and analyze the pressure oscillation phenomena in the realistic combustor and injector in the experiment [5, 6], long-term time-series data should be stored. To this end, a weakly-compressible scheme [10, 13, 24–27], which makes the LES have relatively a larger time increment, is used here.

4.2 Numerical methods

4.2.1 Governing equations

The governing equations used in this LES employing a dynamically thickened flame model [17–22] are the Favre-filtered form of the conservation equations of mass, momentum, enthalpy, and mass fraction of chemical species, along with the equation of state for ideal gas, and they are expressed as follows.

$$\frac{\partial \overline{\rho}}{\partial t} + \nabla \cdot (\overline{\rho}\widetilde{\boldsymbol{u}}) = 0, \tag{4.1}$$

$$\frac{\partial \overline{\rho}\widetilde{\boldsymbol{u}}}{\partial t} + \nabla \cdot (\overline{\rho}\widetilde{\boldsymbol{u}}\widetilde{\boldsymbol{u}}) = -\nabla \overline{P} + \nabla \cdot \overline{\boldsymbol{\sigma}}, \tag{4.2}$$

$$\begin{aligned} \frac{\partial \overline{\rho}\widetilde{h}}{\partial t} + \nabla \cdot (\overline{\rho}\widetilde{h}\widetilde{\boldsymbol{u}}) =& \frac{D\overline{P}}{Dt} + \nabla \cdot \left[\overline{\rho}\left\{EFD_h + (1-\Omega)D_t\right\}\nabla\widetilde{h}\right] \\ &+ \nabla \cdot \left[\overline{\rho}EF\left\{\sum_k \widetilde{h_k}(D_k - D_h)\nabla\widetilde{Y}_k\right\}\right] + \overline{\boldsymbol{\sigma}} : \nabla\widetilde{\boldsymbol{u}}, \end{aligned} \tag{4.3}$$

$$\frac{\partial \overline{\rho}\widetilde{Y}_k}{\partial t} + \nabla \cdot (\overline{\rho}\widetilde{Y}_k\widetilde{\boldsymbol{u}}) = \nabla \cdot \left[\overline{\rho}\left\{EFD_k + (1-\Omega)D_t\right\}\nabla\widetilde{Y}_k\right] + \frac{E}{F}S_{comb,k}, \tag{4.4}$$

$$\overline{P} = \overline{\rho}R\widetilde{T}. \tag{4.5}$$

Here, the overbar ¯denotes the spatially filtered mean value of the physical quantity in grid scale for LES, and the tilde ˜denotes the Favre-averaged value. ρ, $\boldsymbol{u}$, h, and Y_k are the density, velocity, gas mixture specific enthalpy, and mass fraction of species k, respectively. P, h_k, R, and T are pressure, specific enthalpy of species k, gas constant, and temperature, respectively. $\boldsymbol{\sigma}$ is the stress tensor which includes both the resolved and the subgrid scale (SGS) stress. D_h, D_k, and D_t are the thermal diffusivity, mass diffusion coefficient of species k, and turbulence diffusion coefficient, respectively. Here, D_h is expressed as $\rho D_h = \lambda/c_p$, where λ is the heat conductivity and c_p is the specific heat capacity. D_k is calculated from the equation: $\boldsymbol{V_k}Y_k = -D_k\nabla Y_k$, where $\boldsymbol{V_k}$ is

the diffusion velocity of species k, and the diffusion velocities of the different species are evaluated by solving the system of linear equations [28, 29]. The binary diffusion coefficients required for diffusion calculation are obtained from CHEMKIN [30]. The SGS terms are calculated using the dynamic Smagorinsky model [31, 32]. The consumption or production rate of species k is represented by the term $S_{comb,k}$. In this study, hydrogen combustion is modeled using a detailed chemical reaction model proposed by Miller and Bowman, which comprises 9 chemical species and 20 reactions [23] and shows favorable agreement with measurements of the laminar flame speed, especially at lower equivalence ratios, as depicted in Fig. 1 of Ref [33]. Ω is the flame sensor [17, 20, 21] which is used to detect the flame front position, and varies from zero in the fully burned or unburned regions to unity in the reaction zone, is defined as

$$\Omega = \tanh\left(\alpha \frac{q}{q_{max}}\right). \tag{4.6}$$

Here, q is the local heat release rate, and q_{max} is the maximum heat release rate derived from the calculation of one-dimensional laminar flame. α is the parameter controlling the thickness of the transition layer between thickened and non-thickened zones, and its value in the gas combustion system is defined as $\alpha = 10$ based on the previous study [10]. F is a thickening factor used to thicken the flame, in order to resolve the flame with at least five LES grid points, and E is an efficiency function that accounts for the loss of flame wrinkling owing to artificial thickening of the flame. The thickening factor is calculated as

$$F = (F_{max} - 1)\Omega + 1, \tag{4.7}$$

and the maximum value, F_{max} is estimated using

$$F_{\max} = \max\left(\frac{n\Delta_{\text{mesh}}}{\delta_l^0}, 1\right). \tag{4.8}$$

Here, Δ_{mesh} is the cell size, δ_l^0 is the laminar flame thickness, and n is the parameter to control the grid points inside flame thickness, which is set to 5 based on the previous study [18, 20]. The calculation method of the efficiency function is intricate, so refer to Refs. [17–22].

4.2.2 Computational setup

LES is performed for a LSC. A schematic of the computational domain and conditions for the combustor system is shown in Fig. 4.1, and the entire computational domain and grid distribution are illustrated in Fig. 4.2. The configuration of the combustor is set to recreate the experimental setup employed by Shoji *et al.* [5, 6]. The system has a combustor and an injector. The diameter and length of the combustor are 100 mm and 300 mm, respectively. The injector consists of an 8.2:1 area-ratio contraction section, and the diameter of the injector that contains the swirler assembly is 35 mm. The length of the entire injector is 460 mm. The swirler, whose swirl number is 0.39, is placed approximately 43 mm upstream of the injector exit. The components of the swirler are 12 curved vanes inclined at 37° to the combustor axis, a perforated plate, and a central tube. Additional details of the entire combustor system are available in Ref. [5, 6]. The computational domain is discretized using a non-uniform staggered Cartesian grid, with fine grid-spacing around the swirler, main combustion region, and walls. Initially, the entire region is filled with stationary air at a pressure of 0.1 MPa and a temperature of 300 K. As inflow conditions, the completely premixed gas of air and fuel (hydrogen) is introduced into the combustor system from the bottom. The temperature of the premixed gas is 300 K and the equivalence ratio is 0.39. The inflow velocity is set to maintain a constant incoming mass flow rate of the premixed gas, and is derived as follows. First, the conservation of the mass flow rate is expressed as

$$\rho_{in} A_{bottom} U_{in} = \rho_0 A_{bottom} U_0 \tag{4.9}$$

Here, ρ is the density of premixed gas, A_{bottom} is the inlet area at the bottom of the system from where the premixed gas is introduced, and U is inflow velocity. Subscripts *0* and *in* represent the inflow conditions at $t = 0$ s (i.e, initial condition) and at each time step for $t > 0$ s, respectively. The above equation can be rewritten using the equation of state for ideal gas, and the inflow velocity is expressed as

$$U_{in} = \frac{P_0 T_{in}}{P_{in} T_0} U_0. \tag{4.10}$$

The initial inflow velocity, U_0, is set in accordance with the experimental premixed gas mass flow rate, such that the bulk mixture velocity at the injector exit is 15 m/s [5, 6]. To consider the interaction between the walls and the fluid, no-slip boundary conditions are applied on the wall surfaces, and the wall temperature is maintained at 300 K by adopting an isothermal wall condition. The x- axis points in the streamwise direction, and the y- and z- axes are orthogonal to the x-axis and each other. The origin of the coordinate sits at the center of the injector-exit plane (as represented by a white point, O, in Fig. 4.2). In addition to the injector and combustor region, the grid consists of a buffer region to damp the spurious reflections at the outflow and lateral boundaries, which was confirmed essential settings for the simulation of CI to be accurately predicted in the previous study [9].

The reliability of the grid resolution is confirmed by comparing the LES results obtained with 3 different minimum grid spacings (70 µm, 100 µm, and 200 µm) with the experimental results for an open configuration (i.e., the system without the combustor wall but with the same injector section) without reactions. The experimental measurements of the open configuration flow without reactions (i.e., cold flow) were conducted at JAXA, and the cold flow LESs using the aforementioned 3 different minimum grid spacings were performed for the same conditions as those in the experiment. These conditions for the bulk mixture velocity and ambient pressure and temperature of the cold flow are the same as those mentioned above. The radial distributions of time-averaged axial and radial velocity at $x = 5$ mm and $x = 20$ mm are shown in Fig. 4.3. Figure 4.3(a) shows that the time-averaged radial distributions of axial velocity calculated using 70 µm and 100 µm grid spacings are in an overall favorable agreement with the experimental results, albeit with some minor errors. In contrast, the results calculated using the 200 µm grid spacing have larger velocity errors, particularly around the combustor axis (i.e., $y/D = 0$) at $x = 5$ mm, and the discrepancy is larger at $x = 20$ mm across all radial positions. Furthermore, Fig. 4.3(b) indicates that, at the upstream position of $x = 5$ mm, the time-averaged radial distribution of radial velocity calculated using 70 µm grid spacing agrees with the experimental results better than results with the

other grid spacings. Moreover, around the streamwise position of $x = 20$ mm, where the fuel undergoes combustion in the LES of CI, the results with 70 µm and 100 µm grid spacings show almost similar trends in the distributions in contrast to that with 200 µm. Moreover, the absolute errors from the experiment at the peak values are listed in Table 4.1. Based on the above considerations, a minimum grid spacing of 100 µm is adopted for the region around the swirler and combustion region of the LES of CI in this study.

The pressure and velocity variations used in the following discussion are sampled at the point 35 mm away from the origin in the radial direction (as represented by the green square, P, in Fig. 4.2) and the point 5 mm away from the origin in the axial direction (as represented by the yellow triangle, V, in Fig. 4.2), respectively, which are the same positions used in the experiment [5, 6]. The LES is performed using an in-house code FK^3 [34] that can capture the pressure perturbations by employing a pressure-based semi-implicit algorithm for compressible flows [24]. The KK scheme [35] is employed to calculate the convection term of the momentum equation, and the WENO scheme [36] is used to evaluate the convection terms in the scalar transport equations. The third-order explicit Total Variation Diminishing (TVD) Runge-Kutta method is used for time advancement. The thermophysical properties and transport coefficient are acquired from CHEMKIN [30]. The LES domain is discretized using 614.4 million grid points (1500 grid points in x- direction $\times$ 640 grid points in y- direction $\times$ 640 grid points in z- direction). In this LES, the time interval of approximately 0.25 s is simulated to acquire statistic data, and computational time is about 260 hours by parallel computation using 61440 cores on the supercomputer Fugaku provided by the RIKEN Center for Computational Science.

Table 4.1: Absolute error of peak values of velocity distribution of cold flow.

grid size	u (at $x = 5$ mm)	u (at $x = 20$ mm)	v (at $x = 5$ mm)	v (at $x = 20$ mm)
70µm	0.49 m/s	1.62 m/s	0.87 m/s	1.19 m/s
100µm	1.35 m/s	3.05 m/s	2.36 m/s	1.00 m/s
200µm	1.70 m/s	3.24 m/s	1.95 m/s	1.46 m/s

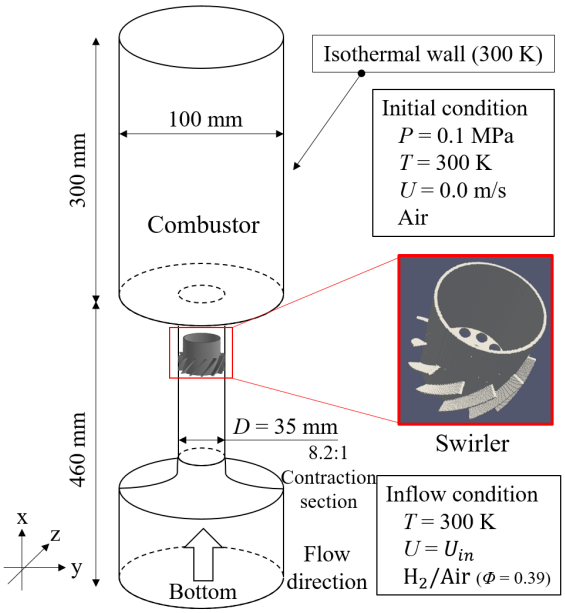

Figure 4.1: Schematic of computational domain and conditions.

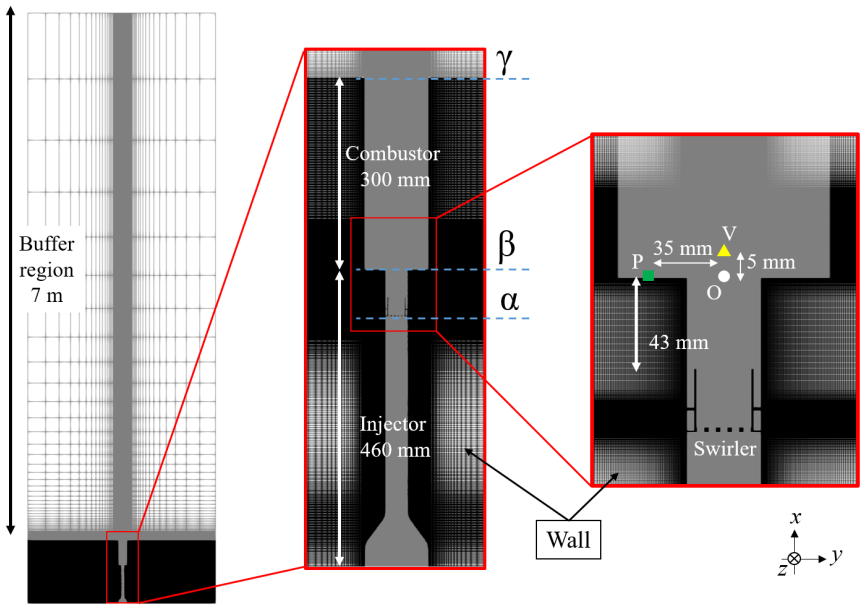

Figure 4.2: Computational grid of LES.

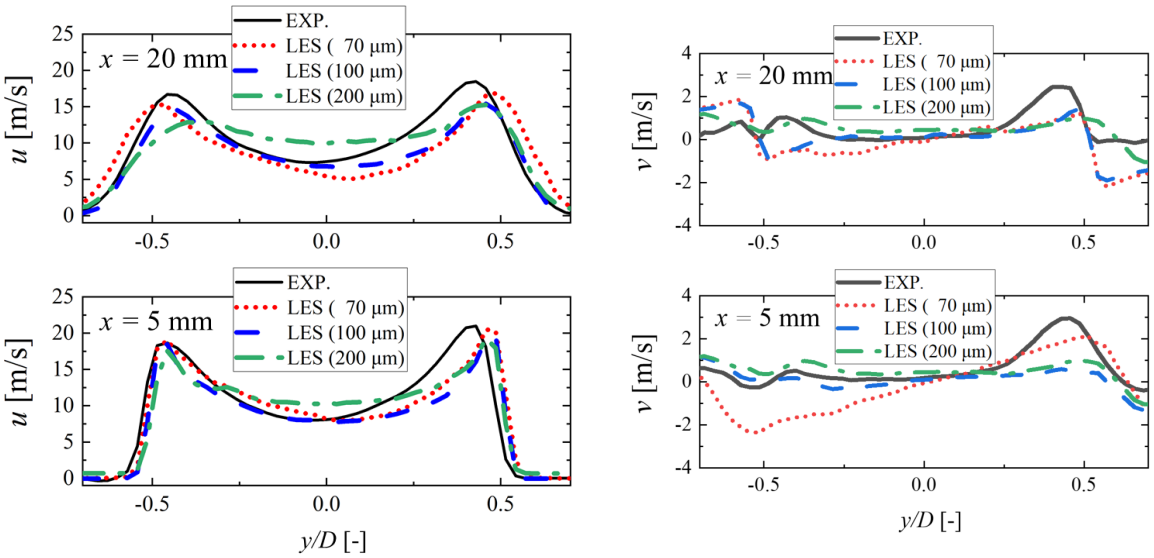

(a) Axial velocity, u

(b) Radial velocity, v

Figure 4.3: Comparison of time-averaged (a) axial and (b) radial velocity between the experimental data and LES predictions using three different grid spacings (70 µm, 100 µm, and 200 µm) for an open configuration without reactions.

4.3 Results and discussion

4.3.1 Characteristics of combustion instability

This section provides an overview of the flame and the flow field and validates this LES by comparing oscillation characteristics.

Figure 4.4 shows the flame obtained from the LES represented by an isosurface of temperature at 1400 K in the LSC, which is colored in blue. The temperature isosurface is not distributed in the vicinity of the injector exit, which gives rise to the form of a lifted flame. Also, in the experiment, a lifted flame was observed, which means that this LES reproduces the basic flame characteristics well. In the outer recirculation zone (ORZ), the temperature of the burnt gas decreases because of the heat loss on the wall surface when the gas flows from downstream to upstream under the influence of the recirculating flow, as depicted in Fig. 4.5(a) which shows the instantaneous distribution of the temperature on the $x - y$ plane obtained from the LES. Thus, coupled with the condition of the balance between the turbulent flame speed and inflow velocity, a lifted flame is formed by the relatively low temperature of the burnt gas near the injector exit in contact with the unburnt gas. Moreover, Fig. 4.5(b) shows the instantaneous distribution of the mass fraction of OH (Y_{OH}) on the $x-y$ plane obtained from the LES, that allows us to observe the combustion characteristics of the lean-premixed hydrogen flame at the flame front. The shape of the lean-premixed hydrogen flame front is more complex than that of hydrocarbon fuels such as methane because of the strong effect of preferential diffusion. For the lean-premixed hydrogen flame, it has been experimentally and numerically confirmed that the convex flame fronts (i.e., with positive curvatures) are more reactive regions and concave flame fronts (i.e., with negative curvatures) are less reactive regions [37]. The Y_{OH} distribution obtained from the LES shows that the flame has a highly complex cellular structure, and combustion occurs more actively on the convex flame front owing to the effect of preferential diffusion.

To explore the effect of preferential diffusion in a more quantitative way, Fig. 4.6 shows the joint probability density function, Joint PDF, of flame surface curvature versus

mass fraction of OH, Y_{OH} obtained from the LES, on the isosurface of temperature at 1000 K which is almost the same temperature used in Ref [37]. Here, the curvature, κ, is defined as $\kappa = \nabla \cdot n$ where $n = -\nabla T/|\nabla T|$, and the positive normal vectors, n point toward the unburnt gas side from downstream. Similar to the previous studies that report the effect of preferential diffusion [37–39], the correlation of the curvature and the Y_{OH} has a positive correlation, and as mentioned above, Y_{OH} is higher at positive curvatures and lower at negative curvatures.

To compare the oscillation characteristics, Fig. 4.7 shows the time variation of pressure measured at point P (green square symbol in Fig. 4.2) obtained from the LES along with the experimental results. The pressure oscillates strongly with a maximum amplitude of about 4 kPa. During CI, pressure oscillations are sporadically weakened a few times as indicated by the black arrows in both the LES and the experiment; however, it does not get fully damped and regains a higher amplitude after a certain period. The underlying mechanisms which cause this phenomenon are described in detail in Section 3.4. Moreover, to confirm the quantitative reproduction accuracy of the pressure oscillations, Fig. 4.8 shows a comparison of the power spectra of the pressure oscillations between the experiment [5, 6] and LES. The peak frequency of the pressure oscillations is 403 Hz in the experiment, while it is 370 Hz in the LES. There is a minor gap of approximately 30 Hz between the experimental result and the LES's result, and this is because of the unavoidable differences between the LES and reality, such as the reproducibility of the complicated wall temperature distribution and complex swirler shape in the LES. In addition, the peak frequency varied in the same order day-by-day depending on the atmospheric conditions even in the experiment. The amplitude at the peak of the oscillations is almost 2 kPa in both the experiment and the LES with approximately 10 % error between them, and it indicates that the present simulation can accurately reproduce not only the frequency but also the amplitude of the pressure oscillations.

These pressure oscillations occur in response to the heat release rate fluctuations, so acoustic flame response analysis using the acoustic flame transfer function is conducted here, which is able to describe the response sensitivity of pressure oscillation from heat

release rate fluctuations. The detailed procedures of calculating the acoustic flame transfer function follow the previous literature [40]. Here, pressure is measured at point P (green square symbol in Fig. 4.2) and the heat release rate is the total value inside the combustor obtained from the LES. Figure 4.9 shows the acoustic flame transfer function, F_{pq}, versus flame Strouhal number, St. At the lower St, the value of F_{pq} is low, and at $St > 3$ (St ≈ 4 corresponds to resonant mode frequency of $f = 370$ Hz), it has a high plateau distribution. This distribution is qualitatively similar to those of the jet flames investigated by Rajaram and Lieuwen [41] and Schlimpert et al. [40] and means that the pressure oscillation does not respond to the heat release rate fluctuation at the lower St conditions, but it responds at $St > 3$. However, at higher St conditions, the amplitude of heat release rate fluctuation was found to be almost negligible compared with that at the resonant mode. Therefore, the higher F_{pq} at higher St does not mean that the flame response at higher St has an eminent impact on combustion instability.

Here, concerning the use of the dynamically thickened flame model, the effect of flame thickening on the correlation of flame and pressure could be non-negligible. For instance, another study [42] investigated the effect of flame thickening on combustion. In particular, since that study targeted combustion noise and the turbulence structure near the flame surface significantly affect noise characteristics, it was essential to investigate the effect of flame thickening. However, this LES studies combustion instability in which a larger vortex has more dominant effects. Moreover, this LES is conducted with a relatively fine computational grid for the lean hydrogen flame. Figure 4.10 shows the instantaneous distribution of the thickening factor, F, on the $x - y$ plane ($z = 0$ mm) obtained from the LES. As this figure shows, the maximum value of F is less than 3, which is small compared with 5 to 30 in the previous study [22]. Therefore, the effect of the thickening factor F is expected not to significantly affect the results.

Also to examine the oscillations of other physical quantities along with the pressure in the combustor during CI in more detail, the time variations of pressure, velocity, global heat release rate, and normalized axial-stretch rate of axial velocity, $a_u = (du/dx)/U_0$, are shown in Fig. 4.11. The velocity shown in this figure is the value at point V (yellow

triangular symbol in Fig. 4.2), the heat release rate is the total value inside the combustor, and the stretch rate is calculated with the data of the axial velocity, u, with a length of approximately 5 mm near the injector exit. In order to compare these LES results with the experimental results, Fig. 4.11 also shows the phase-averaged fluctuations of pressure, velocity, global OH* chemiluminescence intensity, which provide information on heat release rate [43, 44], and normalized axial-stretch rate of axial velocity. Here, the heat release rate is not available in the experiment, and therefore, the heat release rate fluctuation in the LES is compared with the OH* chemiluminescence intensity fluctuation in the experiment. The pressure and velocity oscillate at the same frequency; however, they have a phase difference of about 90°, which is the same as the phase difference observed in the experiment. In addition to the pressure-velocity phase difference, the phase differences between pressure, heat release rate (the OH* chemiluminescence intensity in the experiment), and stretch rate in the LES are almost the same as those in the experiment. Moreover, the stretch rate fluctuates and attains both positive and negative values even though the value remains negative in low-swirl flow with steady conditions. This trend of the stretch rate fluctuation is also confirmed in the experimental study, and it demonstrates the reproduction of the diverging and converging flow fluctuations. Moreover, the phase difference of axial velocity and stretch rate from pressure is also similar to those reported in a previous study of combustion instability in a similar low-swirl combustor [45]. However, in that study [45], the stretch rate oscillates in the negative range, whereas in the present combustion instability, the stretch rate oscillates, ranging from positive to negative values. Some quantitative difference exists in terms of the peak-to-zero amplitude, such that the LES's result of the velocity fluctuation, $|u'| \approx 5$ m/s, is smaller than that of the experiment, $|u'| \approx 8$ m/s, and the LES's result of the stretch rate fluctuation, $|a'_u| \approx 0.03$ mm^{-1}, is smaller than that of the experiment, $|a'_u| \approx 0.04$ mm^{-1}. The difference in the velocity fluctuation from the experiment is considered to be primarily due to the discrepancy in the pressure gradient fluctuation in the inlet channel of LES from the experiment.

To summarize this section, the combustion instability predicted by the LES is val-

idated by comparing the pressure oscillation and fluctuations of velocity, heat release rate, and stretch rate of axial velocity with the experimental results. In addition, the fundamental flame characteristics, such as lifted flame and preferential diffusion effect, are confirmed, and sporadic decay of pressure, which also emerges in the experiment, is observed in this LES study.

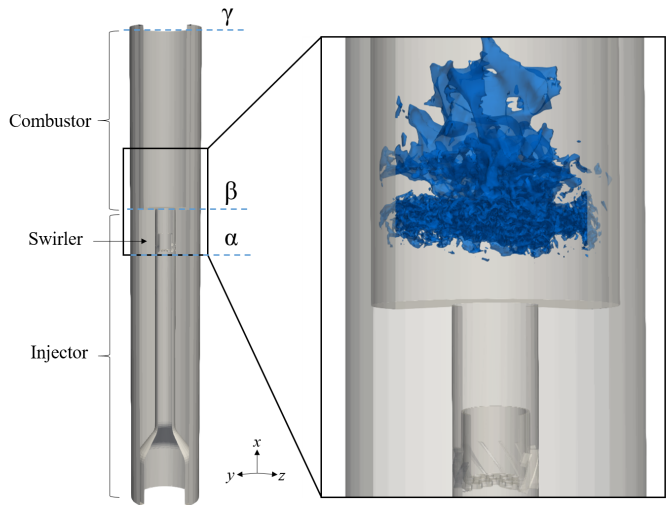

Figure 4.4: Instantaneous 3D distribution of the isosurface of temperature at 1400 K (colored in blue) in the LSC obtained from the LES.

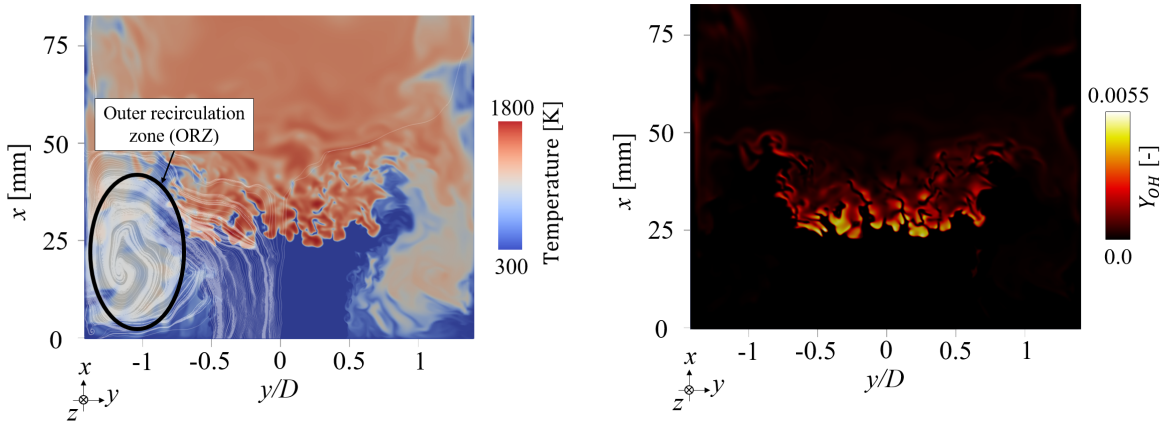

(a) Temperature with streamlines

(b) Mass fraction of OH, Y_{OH}

Figure 4.5: Instantaneous distribution of (a) temperature and (b) mass fraction of OH on the $x - y$ plane ($z = 0$ mm) obtained from the LES.

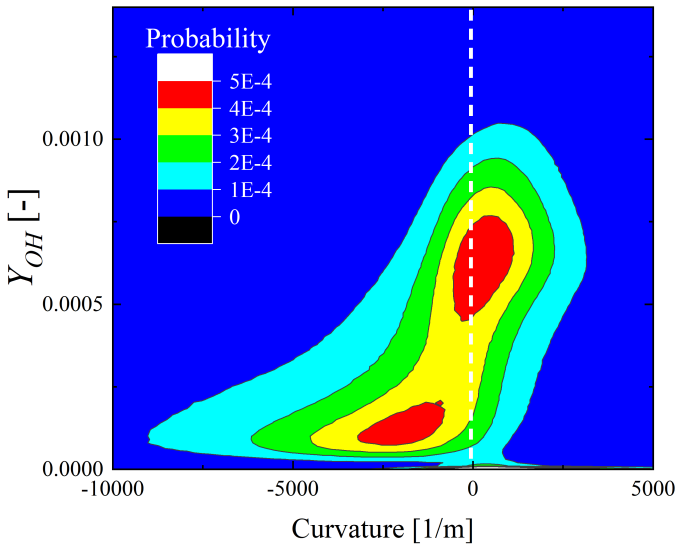

Figure 4.6: Distribution of Joint PDF of curvature versus mass fraction of OH, Y_{OH} obtained from the LES, on the isosurface of temperature at 1000 K. (Preferential diffusion effect)

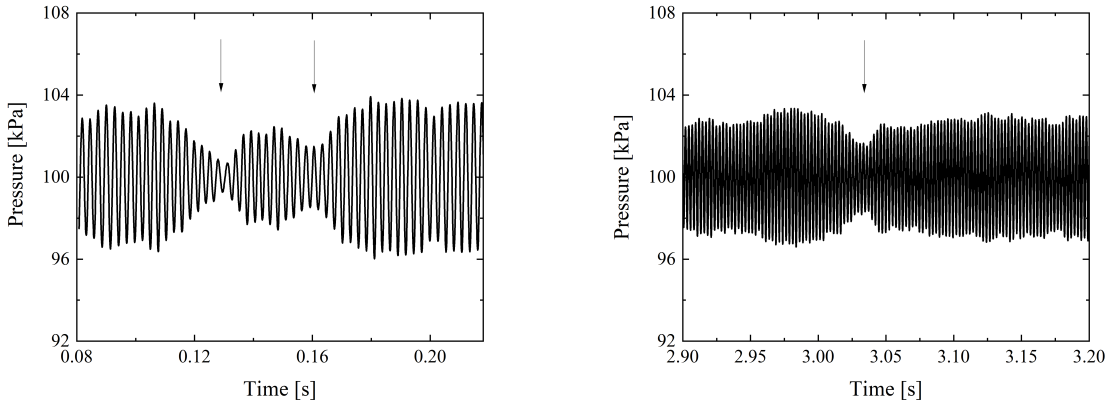

(a) LES

(b) Experiment

Figure 4.7: Time series of pressure at point P (green square symbol in Fig. 4.2) in the combustor during CI from (a) LES and (b) experiment.

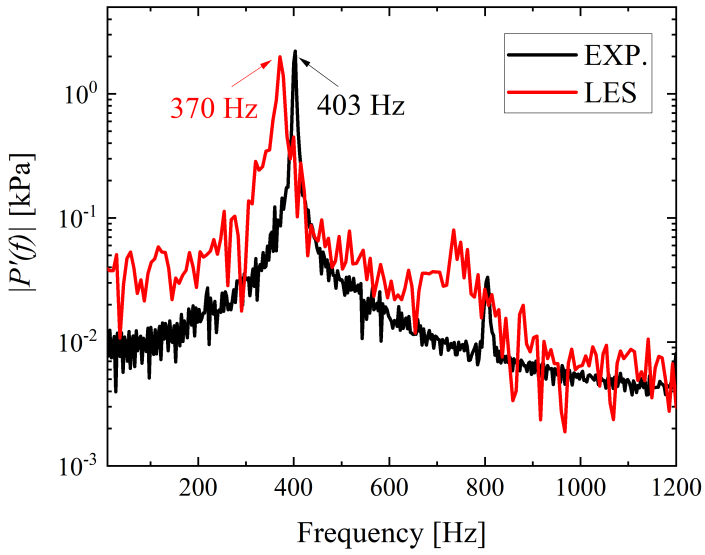

Figure 4.8: Comparison of the power spectra of pressure oscillations between experimental data [5, 6] and LES prediction.

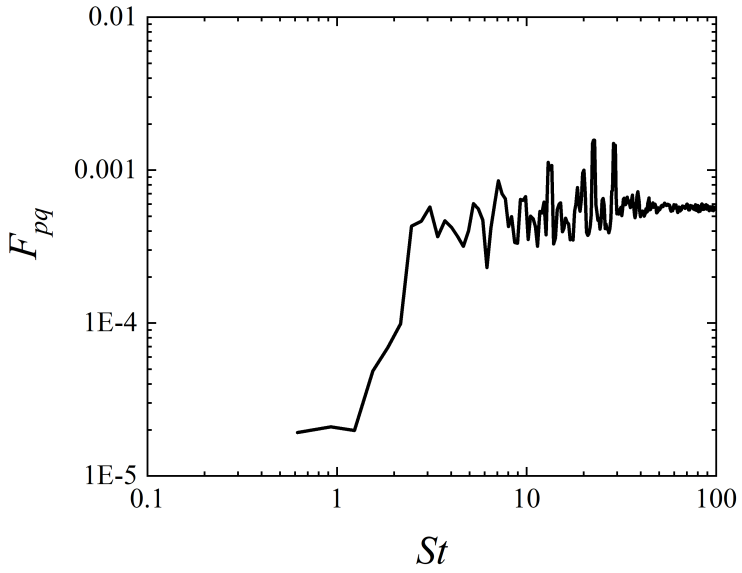

Figure 4.9: Acoustic flame transfer function F_{pq} versus flame Strouhal number, $St = \omega L_f/u_o$, where ω is wave number, L_f is mean flame height, and u_0 is time averaged axial velocity using the data obtained from the LES.

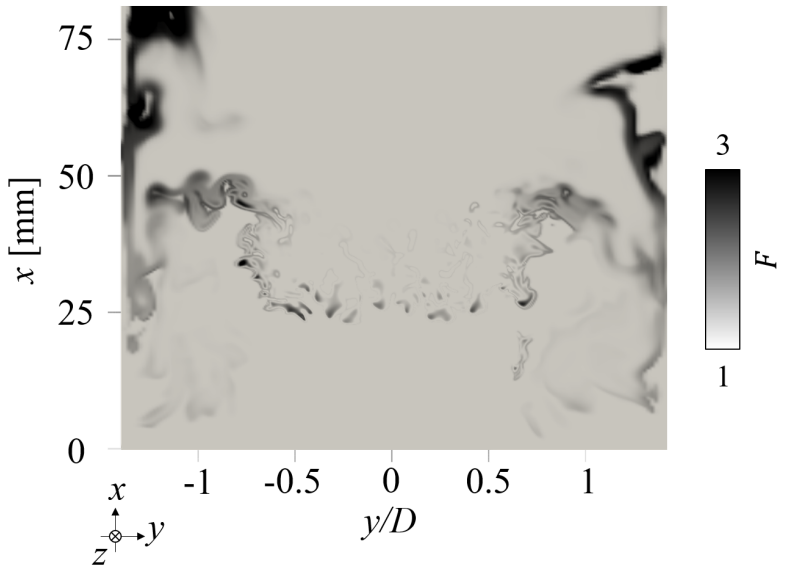

Figure 4.10: Instantaneous distribution of thickening factor, F, on the $x-y$ plane ($z = 0$ mm) obtained from the LES.

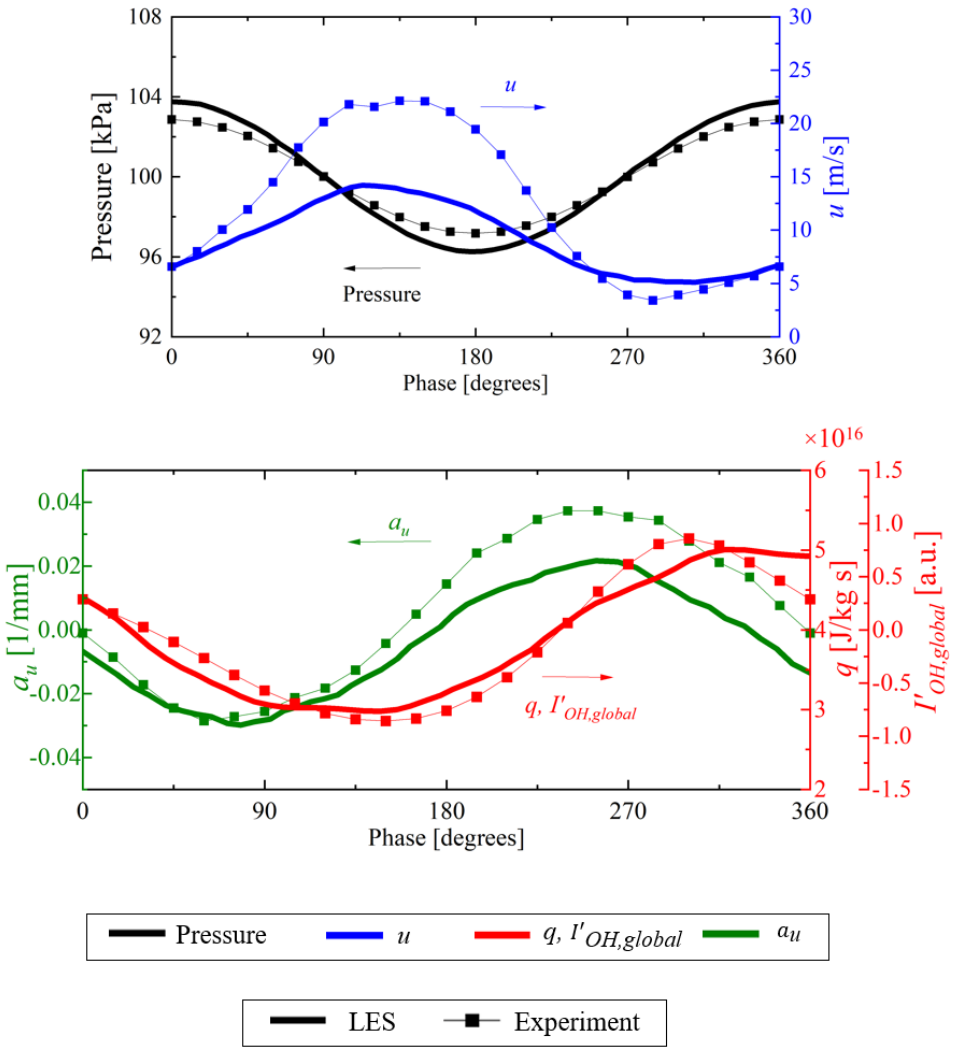

Figure 4.11: Comparison of the instantaneous fluctuations in LES and the phase-averaged fluctuations in Experiment of pressure at point P (green square symbol in Fig. 4.2), axial velocity, u, at point V (yellow triangular symbol in Fig. 4.2), total heat release rate, q which is substituted for global OH* chemiluminescence intensity, $I_{OH}, global$ in the experiment, and normalized axial-stretch rate of axial velocity, a_u, near the injector exit in the combustor.

4.3.2 Flame-flow dynamics

In this section, the correlation of pressure oscillation and heat release rate fluctuation is investigated, and it is discussed with flame and flow fluctuations.

Figure 4.12 shows the local Rayleigh Index (RI) distribution on the $x-y$ plane calculated from the LES data. This local RI is expressed by the following equation.

$$RI = \frac{1}{t_s} \int \frac{P'q'}{P_{ave}q_{ave}} dt \tag{4.11}$$

Here, P' and q' represent the fluctuations in pressure, P, and heat release rate, q, respectively. P_{ave} and q_{ave} represent the time-averaged values, and t_s represents the sampling time. This index is used to visualize the regions of space in which the pressure oscillations and heat release rate fluctuations are highly correlated. The high positive local RI is found to be mainly distributed in regions denoted by 20 mm $< x <$ 50 mm and $0.4 < |y/D| < 1.3$ (circled in white in Fig. 4.12), and no significant positive or negative correlation is observed in the other regions. The same distribution of correlation mode was also obtained using the dynamic mode decomposition (DMD) analysis. To explain this local RI distribution and to discuss flame fluctuation behaviors, Fig. 4.13 shows the phase-averaged values of Y_{OH} on the $x-y$ plane at various phases ($\theta = 0°$, 45°, 90°, 135°, 180°, 225°, 270°, 315°) obtained from the LES in comparison with experimental results. These experimental figures of Abel-deconvoluted OH* chemiluminescence were adapted from "A new pattern of flame/flow dynamics for lean-premixed, low-swirl hydrogen turbulent jet flames under thermoacoustic instability", T. Shoji, S.Tachibana, T. Suzuki, Y. Nakazumi, and T. Yokomori, Proc. Combust. Inst. 38, 2835-2843, Copyright Elsevier (2021). The Y_{OH} distribution shows that the flame has an inverted conical shape around the phase $\theta = 0°$; this is a typical flame structure of stable low-swirl flames. However, the flame structure transitions as the phase progresses, and around the phase $\theta = 180°$, the flame structure is flat in the upstream part of the flame at $x \approx 25$ mm and $|y/D| < 0.5$. Then, the flame structure returns to an inverted conical shape as the phase advances further, and this change in the flame structure is repeated periodically. The periodic fluctuation between the inverted conical flame and the flat flame was also

observed experimentally [5, 6], but this periodic transition of the flame structure was not observed in the other paper which also targeted the combustion instability in the low-swirl combustor [45]. At the phase $\theta = 0°$, when the pressure is maximum, the flame propagates radially toward the combustor's lateral wall, and the heat release rate becomes high in the region surrounded by the green dotted line shown in Fig. 4.13, and as mentioned above, the local RI exhibits high positive values in the same regions. In summary, since the velocity fluctuations do not perfectly match the experimental result, the flame fluctuations are also weaker than in the experiment. However, similar fluctuation phenomena are observed, such as the appearance of inverted conical flames and flat flames.

Such transitions in the flame structure are attributed to changes in the velocity field inside the combustor. Therefore, Fig. 4.14 shows the phase-averaged velocity magnitude distribution on the $x - y$ plane for each phase obtained from the LES. Under steady operating conditions (i.e., without CI), the low-swirl inflow spreads radially outward with respect to the streamwise direction. However, under CI, the direction of inflow inside the combustor can deflect radially inward in the region 0 mm $< x <$ 25 mm around the phase $\theta = 270°$, and the inflow velocity is slower than the other phases. As the phase advances toward $\theta = 90°$, a fast flow directed radially outward with respect to the streamwise direction is introduced into the combustor from the injector. Thereafter, the flow velocity distribution transitions to a slow and inward-deflected flow again. This is a switching phenomenon of low-swirl flow under strong CI conditions, which was also observed in the experiment [5, 6], but was also not observed in the other paper which also targeted the combustion instability in the low-swirl combustor [45].

Furthermore, To examine the flame and inflow fluctuations in the CI in more detail, the fluctuations of the premixed gas supply from the injector are an essential factor, but it is superfluous to the main contents; therefore, the characteristics of inflow from the swirler to the flame surface are investigated in Appendix.

A brief summary of this section is that the flame periodically transitions between the inverted conical flame and the flat flame, and it is attributed to the switching phe-

nomenon under the CI, namely the outward and inward deflections of the inflow. These flame transitions and inflow switching phenomena are unique to this combustor configuration.

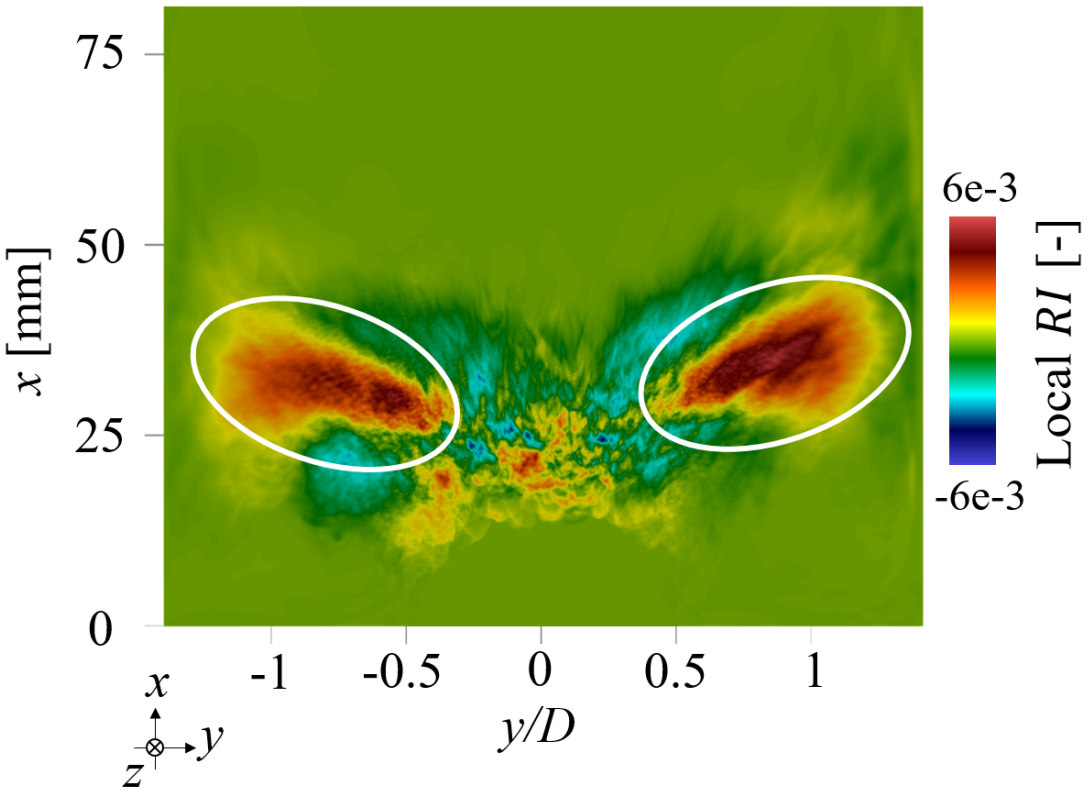

Figure 4.12: Distribution of local Rayleigh Index, RI, on the $x-y$ plane ($z = 0$ mm) calculated from the LES data.

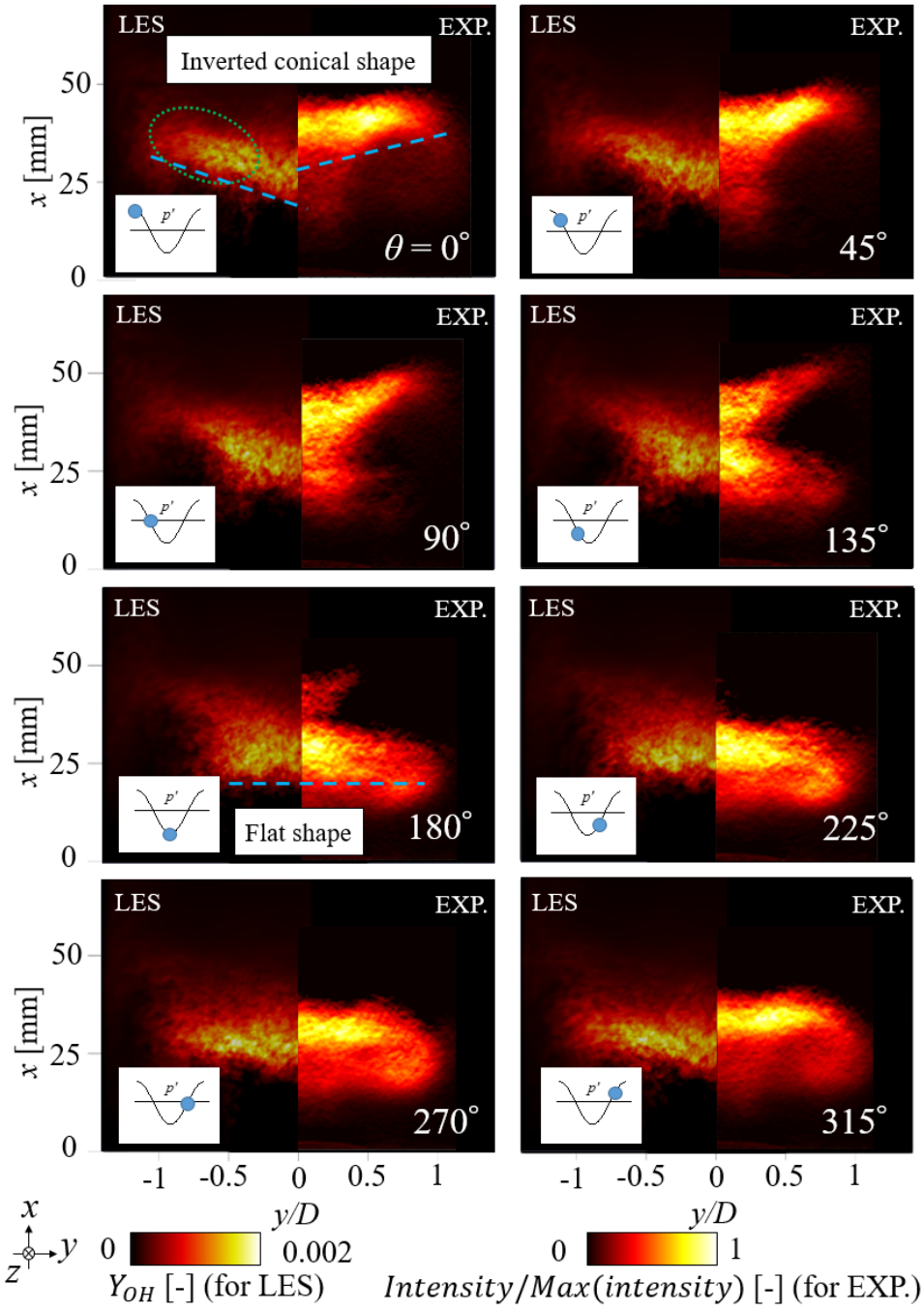

Figure 4.13: Sequential images of the phase-averaged distribution of the mass fraction of OH, Y_{OH} on the $x-y$ plane ($z = 0$ mm) at various phases with phase-averaged Abel-deconvoluted OH* chemiluminescence images from experimental results [5, 6]. (Switching between the inverted conical and flat flame.)

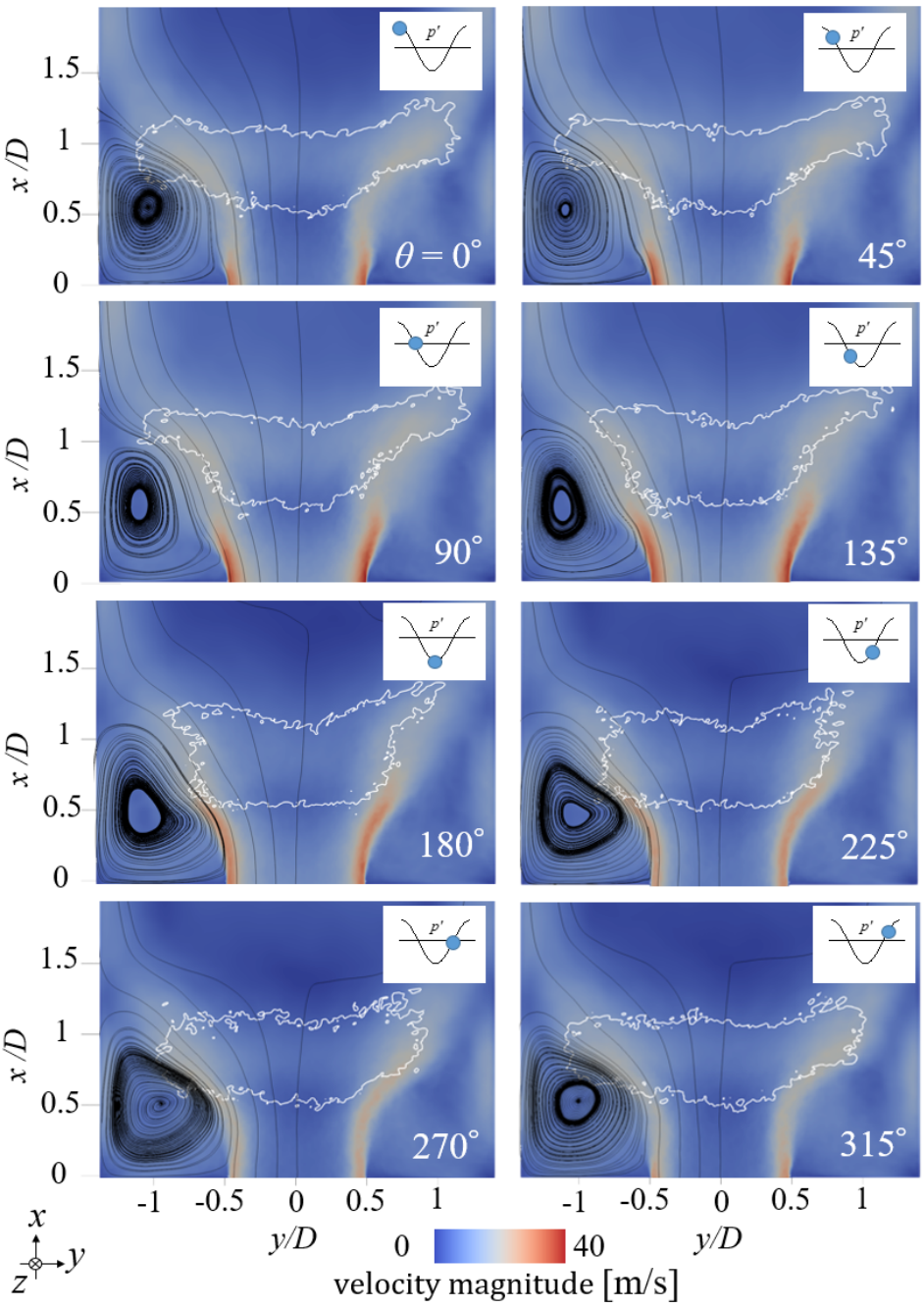

Figure 4.14: Sequential images of the phase-averaged distribution of the velocity magnitude on the $x-y$ plane ($z = 0$ mm) at various phases obtained from the LES. The white contours denote 20 % of the maximum value of Y_{OH}, and the flow directions are represented by black lines. (Switching between the outward and inward deflections of inflow.)

4.3.3 Flow switching phenomenon

As mentioned in the previous section, the pressure oscillates strongly under CI, and this affects the time variation of the velocity, namely the outward and inward deflections of the inflow to the combustor, the so-called flow switching phenomenon. To investigate the flow transitions inside the combustor, it is necessary to know the inflow transition inside the inlet channel, and the transitions such as the acceleration and deceleration of inflow depend on the pressure gradient in the inlet channel. Therefore, to understand the time variation of the axial pressure distribution, Fig. 4.15 shows the phase-averaged pressure distribution in the streamwise direction at different phases obtained from the LES. In this figure, the positions α, β, and γ correspond to the positions indicated in Fig. 4.2. The amplitude of the pressure oscillations is found to be the largest around the swirler inlet (position α), which is the antinode of the oscillations, and its wavelength is about 3/4 of the length of the entire system comprising the injector and combustor, which is consistent with the estimation in the experiment [5, 6]. Moreover, these positions of node and antinode are similar to those in the different study of the combustion instability in the low-swirl combustor [45] in which the antinode sits upstream of the inlet exit and node is positioned at the end of the combustor.

The pressure gradient in the inlet channel fluctuates and has positive and negative values, which accelerates and decelerates the inflow. This fluctuating inflow affects the recirculating flow at the ORZ, and this subsequently affects the deflections of the inflow to the combustor. To examine the fluctuations of recirculating flow, Fig. 4.16 shows the sequential images of the phase-averaged distribution of the streamline in ORZ colored by the radial velocity, v, on the $x-y$ plane ($z = 0$ mm) at various phases obtained from the LES. The scale and shape of the recirculating flow vary in tune with the pressure oscillation. When focusing on the distribution at around $\theta = 90°$, the major recirculating flow exists in the ORZ, and the shape of the recirculating flow is axially larger compared with the distributions at the other phases. Consequently, the radial velocity around the injector exit is relatively slow and has a small effect on the deflection of the inflow around this phase. Therefore, it forms the outwardly deflected inflow, which is observed in the

LSC with a stable operation. On the other hand, when focusing on the distribution at around $\theta = 270°$, the major recirculating flow shifts upstream and forms a radially larger recirculating flow compared with the distributions at the other phases. This distribution of recirculating flow makes the radial velocity faster in a broad region around the injector exit (0 mm $< x <$ 10 mm and $0.5 < |y/D| < 1.4$ (circled in black in Fig. 4.16)) and the inflow deflect inwardly with respect to the streamwise direction.

In addition to the effect of the recirculating flow, the pressure distribution in the radial direction appears to be involved. Figure 4.17 shows the phase-averaged radial distributions of pressure at $x = 5$ mm deducted by the pressure at $y/D = 1$ at different phases obtained from the LES. Once a resonant pressure oscillation occurs inside the combustor, the radial pressure distribution is not homogeneous, especially at the streamwise positions, such as at $x = 5$ mm, which are close to the injector exit. At phase $\theta = 0°$, the pressure around the combustor axis is higher than that around $y/D = 1$, and at $\theta = 180°$, the pressure around the combustor axis is lower than that around $y/D = 1$. Hence, at $\theta = 0°$, the negative radial pressure gradient induces the outward deflection of the inflow, and at $\theta = 180°$, the positive radial pressure gradient induces the inward deflection of the inflow.

Considering these effects mentioned above, the radial velocity must fluctuate, so the phase-averaged radial distributions of radial velocity at $x = 5$ mm at each phase obtained from the LES are shown in Fig. 4.18. Here, note that the phase difference between the oscillations of pressure and velocity is 90°. Thus, the velocity characteristics at phase $\theta = 90°$ can be analyzed using the pressure distribution at phase $\theta = 0°$. At phase $\theta = 90°$, the radial gradient of radial velocity, dv/dr, in the region $-0.5 < y/D < 0.5$ has a positive value, and it means that the flow is radially deflected outward, which is influenced by the fluctuation of recirculating flow and radial pressure distribution at phase $\theta = 0°$. In contrast, at phase $\theta = 270°$, dv/dr in the region $-0.5 < y/D < 0.5$ has a negative value, and this means that the flow is radially deflected inward.

In short summary, this section explores the unique switching phenomenon of the inflow, and it is found that the fluctuations of recirculating flow in the ORZ and of the

radial pressure gradient have effects on the outward and inward deflections of the inflow. When the recirculating flow is strong and the radial pressure gradient is positive, the inflow points inward, and when the recirculating flow is weak and the radial pressure gradient is negative, the inflow points outward.

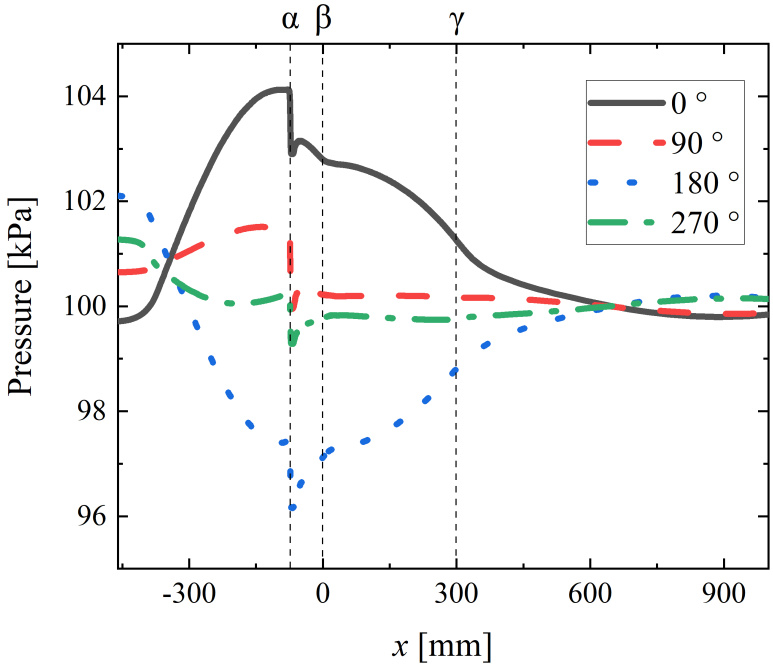

Figure 4.15: Phase-averaged streamwise distributions of pressure at (y, z)=(0 mm, 0 mm) at $\theta = 0°, 90°, 180°, 270°$ obtained from the LES. Positions (α, β, γ) correspond to those indicated in Fig. 4.2.

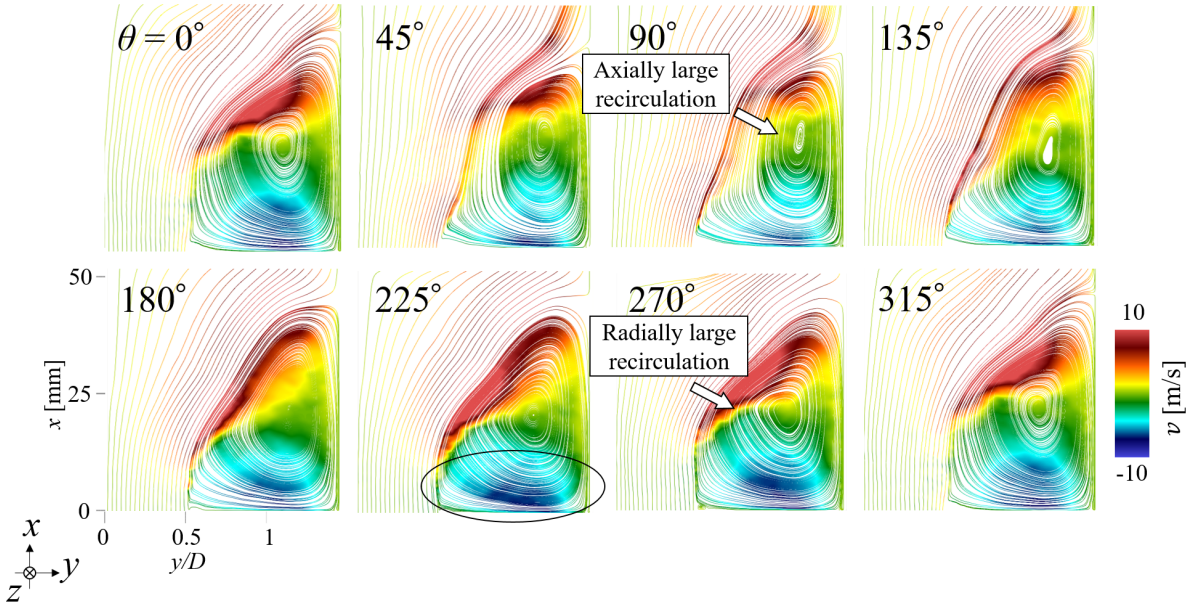

Figure 4.16: Sequential images of the phase-averaged distribution of streamline in the ORZ colored by radial velocity, v, on the $x - y$ plane ($z = 0$ mm) at various phases obtained from the LES. (Fluctuation of recirculating flow.)

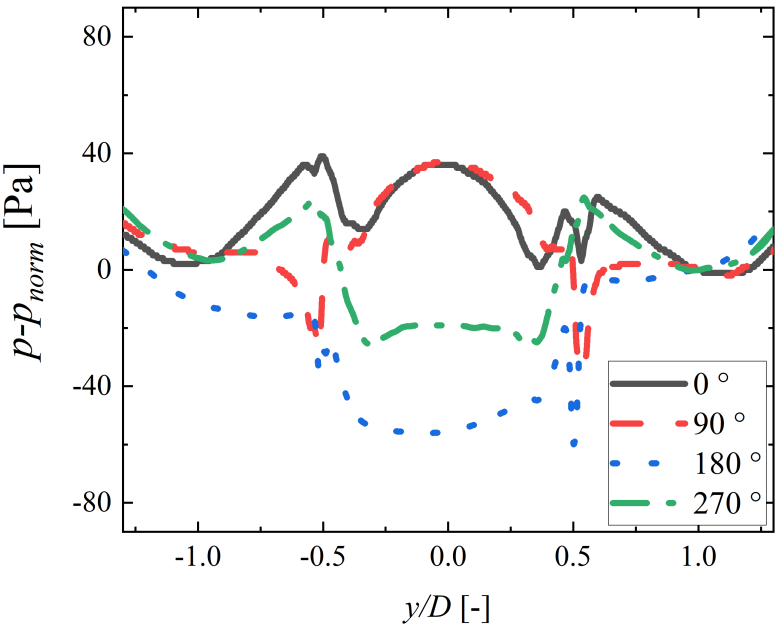

Figure 4.17: Phase-averaged radial distributions of pressure, p, deducted by the pressure at $y/D = 1$, p_{norm}, at $\theta = 0°, 90°, 180°, 270°$ at $(x, z) = (5$ mm, 0 mm) obtained from the LES. (Fluctuation of radial pressure gradient.)

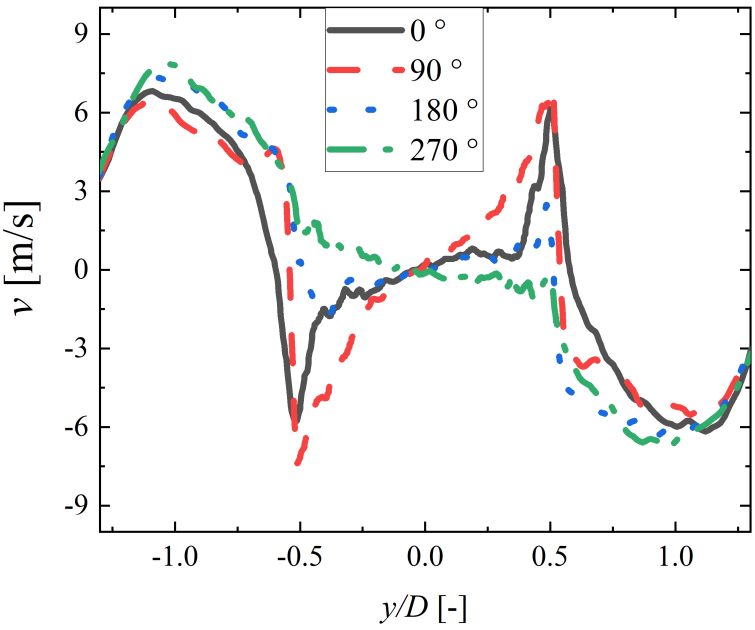

Figure 4.18: Phase-averaged radial distributions of radial velocity, v, at $\theta = 0°, 90°, 180°, 270°$ at $(x, z) = (5 \text{ mm}, 0 \text{ mm})$ obtained from the LES.

4.3.4 Instantaneous decay of pressure oscillations

The instantaneous decays of pressure oscillations, as observed in Fig. 4.7 (indicated by the two black arrows), are discussed in detail. A comparison of the flame structures between the time duration when the amplitude of pressure oscillations is strong, and the time instance when the pressure oscillation amplitude declines sporadically is performed. Figure 4.19 shows the flame represented by an isosurface of temperature at 1400 K in the LSC obtained from the LES, which is colored in blue, at the time instance of $t = 0.1246$ s when the pressure oscillation amplitude is sporadically weakened. The flame structure when the pressure oscillates violently has already been presented in Fig. 4.4. When pressure oscillations sporadically decay, although the flame is lifted, it locally extends upstream in the areas circled in white.

To investigate the effect of such localized upstream flame propagation on the oscillatory phenomena, Fig. 4.20 shows the instantaneous Y_{OH} distributions on the $x-y$ plane at different phases obtained from the LES during the time period when the pressure oscillation amplitude is sporadically weakened. In this figure, it is once again confirmed that the flame locally extends upstream in the areas circled by white dotted lines. In addition, judging from the flame fluctuation phenomenon, when strong pressure oscillations occur in the combustor, the flame structure periodically transitions between the inverted conical shape and the flat shape, as shown in Fig. 4.13, whereas when the amplitude of the pressure oscillations is weak, the flame structure transition is not observed at any phase. This is because the localized upstream extension of the flame stabilizes the flame structure and prevents its violent fluctuations, thereby causing the flame to always be present in the areas outlined by the green dotted lines in Fig. 4.20. This results in a weakening of the correlation between pressure oscillations and heat release rate fluctuations in these regions where the local RI would otherwise be high under strong CI conditions (i.e., drastic flame fluctuations).

To investigate the timing of the occurrence of this sporadic flame extension during the strong pressure oscillation, Fig. 4.21 shows the LES result of the time series of pressure and the mass fraction of OH integrated spatially, $Int.(Y_{OH})$, over the combustor volume

ranging from $x = 0$ mm to $x = 17$ mm, which is the upstream region of the flame, when pressure oscillates strongly and when the pressure oscillations instantaneously decay. In the time interval with the strong pressure oscillation, $Int.(Y_{OH})$ oscillates in phase with the pressure oscillation, and at the phase when the pressure becomes maximum, $Int.(Y_{OH})$ also has a maximum value. On the other hand, in the time interval with weak pressure oscillation, at some time instances, $Int.(Y_{OH})$ spikes up and becomes much higher than other time instances, as pointed by the black arrows, which indicate the existence of the eminent flame extension to the upstream. Moreover, the spikes of $Int.(Y_{OH})$ oscillation lag the pressure oscillation peaks compared with the other peaks of $Int.(Y_{OH})$. To understand the impact of the flame extension on the coupling between the pressure oscillations and the heat release rate fluctuations, the total heat release rates are also shown in Fig. 4.21. After the first spike of $Int.(Y_{OH})$, the phase difference between the pressure oscillations and the fluctuations of heat release rate increases, suggesting a decoupling of these two fluctuations. Moreover, after the second spike of $Int.(Y_{OH})$, the heat release rate does not fluctuate in synchrony with the pressure oscillations, which induces the pressure oscillation to decay more.

Furthermore, in the process of instantaneous decay of pressure oscillation, the pressure oscillation is considered to deviate from the resonant mode of the combustor. Therefore, to investigate the mode shift, wavelet analysis is employed. Here, as the wavelet type, Morlet is used, and the wave number is set to 10. Figure 4.22 shows the time series of the pressure oscillation and its frequency. As predicted, when pressure instantaneously decays, as pointed out by a black arrow, the pressure oscillation frequency becomes lower compared with the resonant frequency, 370 Hz. As a result, the pressure oscillation decays, but once the pressure oscillation frequency gets back to the resonant frequency, the amplitude of the pressure oscillation becomes stronger again.

All in all, without the flame extension, the incoming unburned premixed gas is entrained in the oscillating lifted flame, and the phase difference between pressure and heat release rate becomes such that the RI increases, thus maintaining combustion oscillation. However, with the flame extension, combustion occurs further upstream, and the phase

difference between pressure and heat release rate changes, resulting in a smaller RI and the inability to generate enough energy to maintain the thermoacoustic. This is because the localized upstream extension of the flame stabilizes the flame structure and prevents its violent fluctuations. This localized flame extension in the upstream direction can occur at any time, but whether or not the reactions occur actively enough in the upstream regions to enable the localized upstream flame propagation and stabilization of the fluctuations of the flame structure is primarily determined by various factors, including the amount of hot gas entrained locally toward the combustor axis, amount of unburned premixed gas coming into contact with the hot gas, and local flow-field conditions.

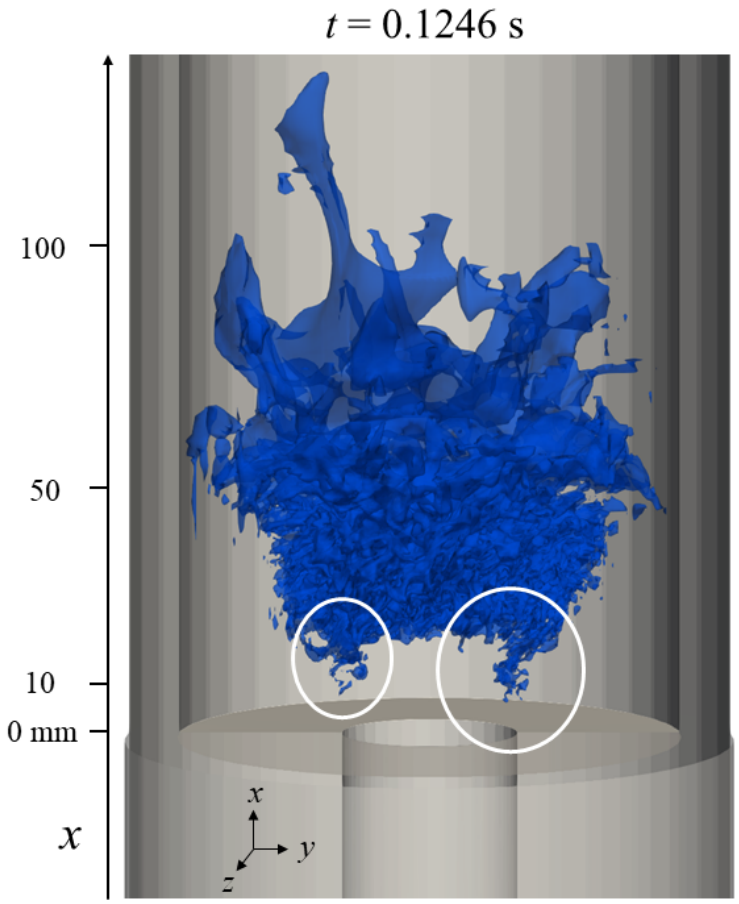

Figure 4.19: Instantaneous 3D distribution of the isosurface of temperature at 1400 K (colored in blue) at the phase when the flame propagates upstream obtained from the LES. (Instantaneous flame's upstream extension.)

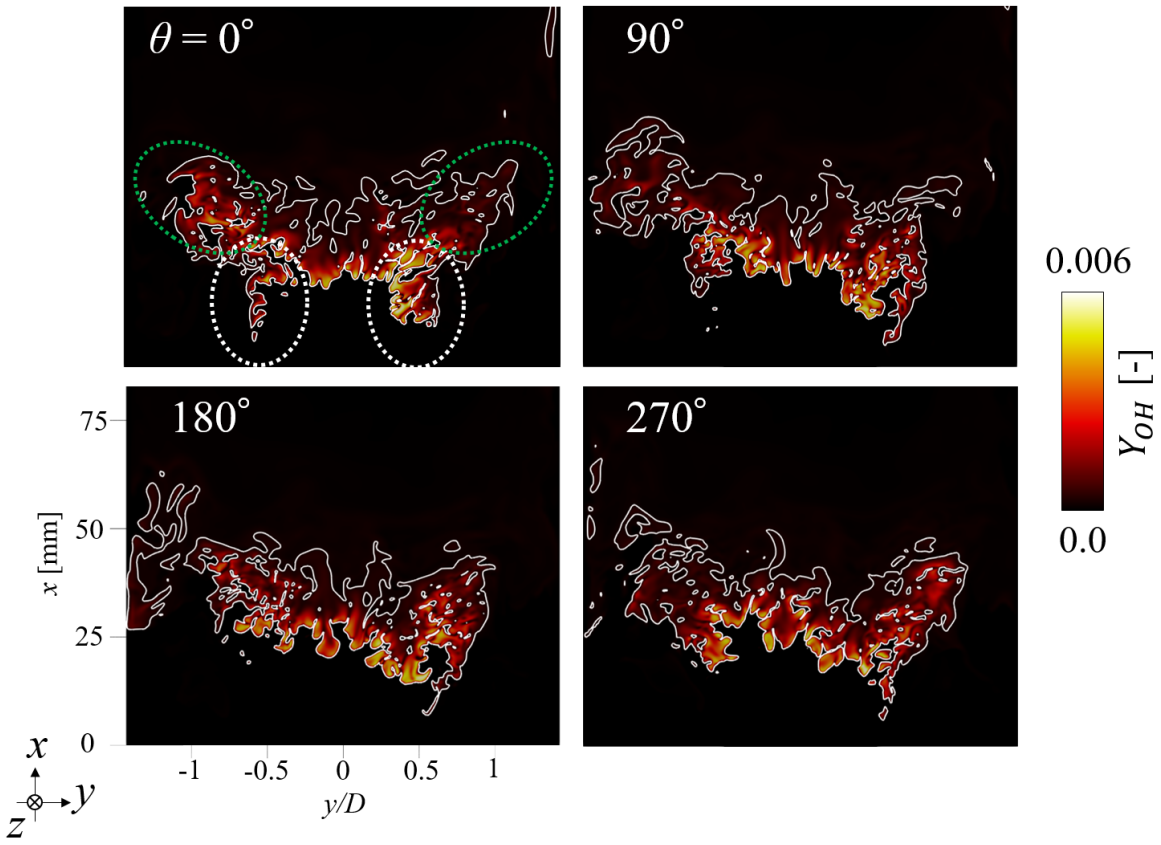

Figure 4.20: Instantaneous distributions of the mass fraction of OH, Y_{OH} on the $x-y$ plane ($z = 0$ mm) at $\theta = 0°, 90°, 180°, 270°$ obtained from the LES when the flame propagates to upstream. The white contours of 5 % of the maximum value of Y_{OH} are also shown in this figure

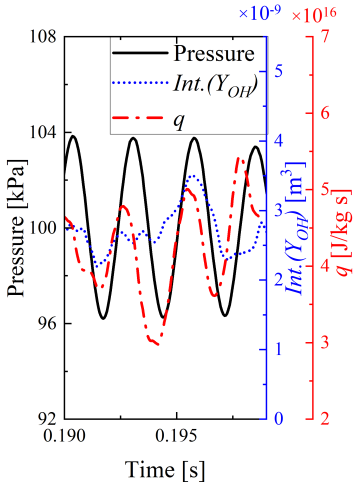

(a) With strong pressure oscillations

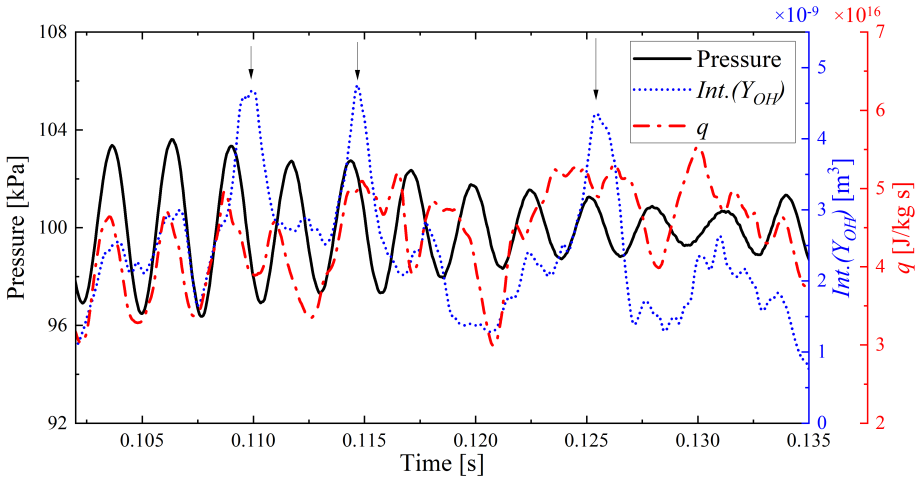

(b) With sporadic decay of pressure oscillations

Figure 4.21: Short time series of pressure at point P (green square symbol in Fig. 4.2), integral of the mass fraction of OH upstream of combustor, $Int.(Y_{OH})$, and total heat release rate, q obtained from the LES (a) with strong pressure oscillations and (b) with sporadic decay of pressure oscillations. (Timing of the flame's upstream extension.)

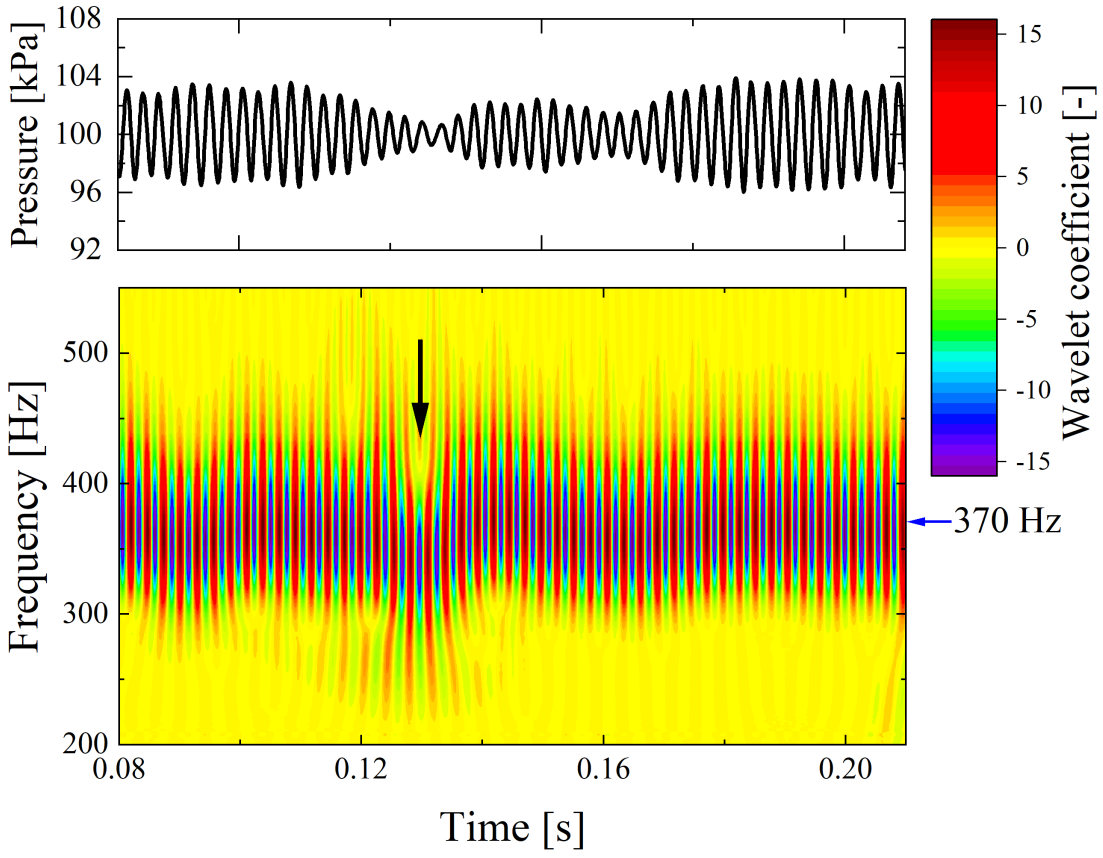

Figure 4.22: Time series of the pressure oscillation and its frequency obtained by the wavelet analysis using the data obtained from the LES. (Frequency shift during the pressure oscillation decay.)

4.4 Conclusions

In this chapter, the mechanism of flame-flow dynamics of a lean-premixed hydrogen flame in a low-swirl combustor (LSC) under combustion instability was investigated in detail using LES, which considered the swirler assembly in the upstream region (i.e., injector). As a combustion model, a dynamically thickened flame model [17–21] with a detailed chemical reaction model consisting of 9 chemical species and 20 reactions [23] was employed. The configurations of the combustor and injector were the same as those in the experiment [5, 6]. The swirl number of the swirler in the injector was set to be about 0.39, the bulk velocity in the injector channel was 15 m/s, the pressure was 0.1 MPa, the length of the combustor was 300 mm, and the equivalence ratio was 0.39. The main results of this study are summarized as follows.

1. The present LES predicts the combustion instability phenomena observed in the experiment [5, 6]. Namely, the pressure inside the LSC strongly oscillates, and the pressure oscillations' frequency and intensity are in quantitatively good agreement with that in the experiment [5, 6]. Moreover, although the pressure oscillations sporadically exhibit temporal declines in amplitude, they are not fully damped but recover again. Furthermore, a unique behavior, which was first confirmed in the experiment [5, 6], such as the periodic transitions between the inverted conical flame structure and the flat flame structure, is similarly observed.

2. The periodic transitions between the inverted conical flame structure and flat flame structure are caused by the outward and inward deflections of the inflow, which is comprehensively associated with the fluctuation of the recirculating flow behavior in the region near the combustor wall, the pressure gradient in the radial direction inside the combustor, and the flow behavior in the upstream injector channel. Specifically, the inverted conical flame is formed by the outward deflection of the inflow with a faster velocity, which pushes the flame in the radially outer region downstream. On the other hand, the flat flame is formed by the inward deflection of the inflow with slower velocity, which allows the flame in the radially outer

region to propagate upstream.

3. The sporadic decay of pressure oscillations mentioned in conclusion 1 appears when the pressure oscillations and heat release rate fluctuations temporally decouple. This temporal decoupling is caused by the aperiodic flame transformation, namely, the flame temporally and locally propagates toward the upstream region close to the rim of the injector, which makes the flame stable.

4.5 Appendix: Delay time of inflow

As mentioned above, the fluctuations of the premixed gas supply from the injector are an essential factor. In this study, the particle tracking method is employed to capture the inflow characteristics, and the trajectory and the delay time, which denote the travel time of a particle, are investigated.

The following procedure is applied as the particle tracking method. Approximately 5000 particles are placed spatially homogeneously on the $y-z$ plane ($x = -80$ mm) upstream of the swirler in the injector tube at phase $\theta = 0°$. Each particle convects with the velocity of the premixed gas downstream. This procedure is applied as the post-process of the LES, and these particles do not affect the turbulent combustion field. The delay time, τ_{-80}, is estimated as the required time to come to certain positions from $x = -80$ mm. In this analysis, the delay time of particles at $x = -40$ mm, $x = 0$ mm, and on the flame surface is investigated. The flame surface is defined as the position of 5 % of the maximum OH mass fraction ($Y_{OH,5\%} = 3 \times 10^{-4}$). The required time for a particle to come to a certain position is measured only when the particle reaches the position, and thus, it can be presumed that all particles which are used to calculate the delay time are in the unburnt gas. In the experiment, a similar analysis was conducted, but the delay time was estimated as the travel time from $x = 0$ mm to the flame surface, because no data was available in the injector channel. Therefore, to compare the LES results with the experimental results, τ_0 is also calculated using this LES data.

Figure 4.23 shows the initial distribution and sequential images of particles with the

flame surface represented by the blue isosurfaces, which denote the 5 % of the maximum OH mass fraction ($Y_{OH,5\%} = 3 \times 10^{-4}$). The colors of particles represent the initial radial distance from the combustor axis at $x = -80$ mm, r_{-80}. As this figure shows, the particles convect downstream and flow into the combustor. Some particles are trapped and do not move on the wall surface due to the presumption of the non-slip wall, but the number of trapped particles is not so significant that it can derail the discussion. Most particles that flow into the combustor spread in a radially outward direction and pass through the flame surface, but different particle motions are observable among the particles from different initial positions.

To investigate the various particle motions, Fig. 4.24 shows the scatter plot of delay time, τ_{-80}, at $x = -40$ mm, $x = 0$ mm, and on the flame surface, and τ_0. In this figure, the wall position, W.P., is depicted with a black line. As this figure shows, the delay time from $x = -80$ mm to $x = -40$ mm is almost the same among the radial locations, but the delay time from $x = -80$ mm to $x = 0$ mm is longer around the center axis of the combustor than that at the peripheral of the injector ($|r/D| \approx 0.5$). This is attributed to the velocity distribution in the injector channel, in which the velocity at the center axis is slower than the peripheral of the injector.

On the other hand, the distribution of delay time on the flame surface from $x = -80$ mm is considerably different from the other axial positions. The delay time is longer around the center axis of the combustor, and it becomes the shortest around $r/D = 0.5$ and increases at the region $r/D > 0.5$. At the region $r/D > 0.5$, as pointed out by two red arrows, the distribution is split into two parts, which means that the particles go through the flame surface not constantly but periodically, even though the particles enter the flame surface constantly in the other regions. This periodic entry of particles, which consequently represents the supply of the unburnt premixed gas to the flame surface in the ORZ, $r/D > 0.5$, makes the local RI larger at this region, as shown in Fig. 4.12, and the constant entry around the center axis makes the local RI smaller. For the two split distributions at $r/D > 0.5$ pointed out by the two red arrows in Fig. 4.24(c), this time difference is almost the same as the time for a single cycle of pressure

oscillation ($\approx$ 2.7 ms), and the underlying phenomena are tightly connected with the thermal-acoustic coupling. Further, the first distribution of the two split distributions at $r/D > 0.5$ ($\tau_{-80} \approx 6$ ms) mainly consists of red particles, which means that particles originally in the peripheral region of the injector go through the flame surface first, and the second distribution of the two split distributions at $r/D > 0.5$ ($\tau_{-80} \approx 8$ ms) also consists of yellow and green particles, which means that particles originally in the center region of the injector go through the flame surface at the next cycle after the cycle when the particles originally at the peripheral region of the injector go through the flame surface. These characteristics are also confirmed in Fig. 4.23. In the first cycle, the yellow and green particles are yet to pass through the flame surface at $r/D > 0.5$, but the red particles move toward the flame surface as indicated by white arrows with the vortex as shown in Fig. 4.14. In the second cycle, the yellow and green particles which have flown into the central region in the combustor are transferred radially outward in the combustor, as indicated by black arrows, and they pass through the flame surface at $r/D > 0.5$. However, a relatively small amount of green particles are distributed $r/D > 0.5$ in the second cycle, and the green particles at $r/D < 0.5$ have a wider range of delay time, which represents the small effect of the premixed gas originally in the center region of the injector on the CI.

In addition to the above discussion, a comparison with the experiment is performed. When the delay time on the flame surface is calculated with particles originating from $x = 0$ mm, the delay time, τ_0, becomes minimum around $r/D = 0.5$. This is similar to the experimental results [6]. However, contrary to the trend of the time delay from $x = -80$ mm, τ_{-80}, most particles go through the flame surface at the same delay time. This is because when the delay time is measured from the time at the $x = 0$ mm, the residence time of particles inside the injector channel cannot be captured. Therefore, to investigate the different inflow characteristics under the CI in this configuration, it is indispensable to consider the fluctuations of flow inside the injector.

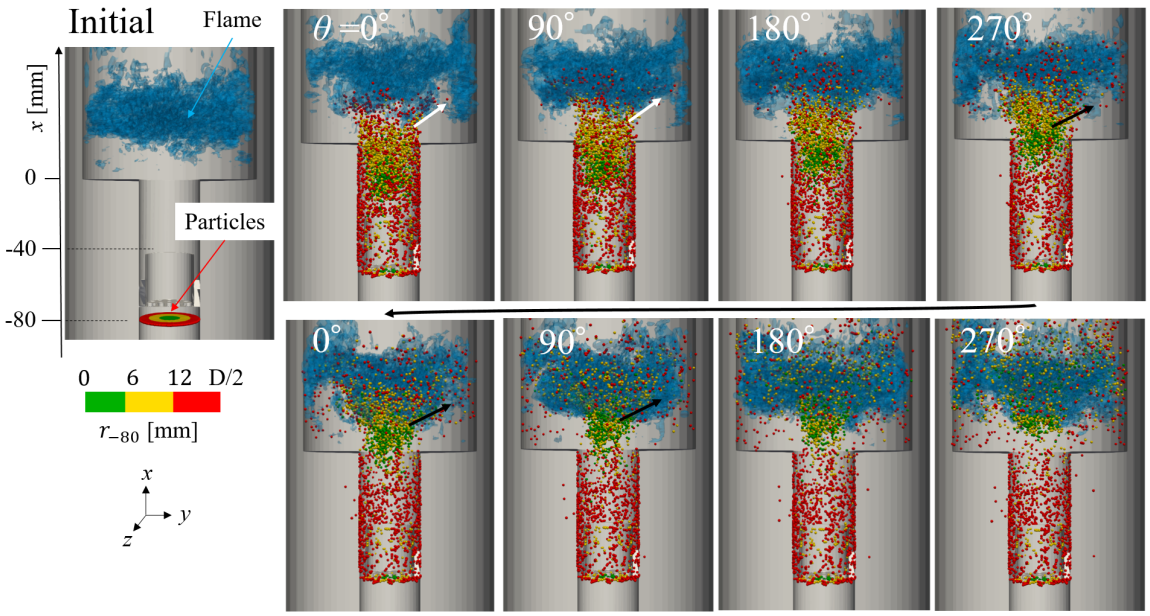

Figure 4.23: Initial distribution and sequential images of particles for calculating the delay time, τ. The blue isosurfaces denote the 5 % of the maximum OH mass fraction ($Y_{OH,5\%} = 3 \times 10^{-4}$) and all particles are colored by the initial radial distance from the combustor axis at $x = -80$ mm, r_{-80}.

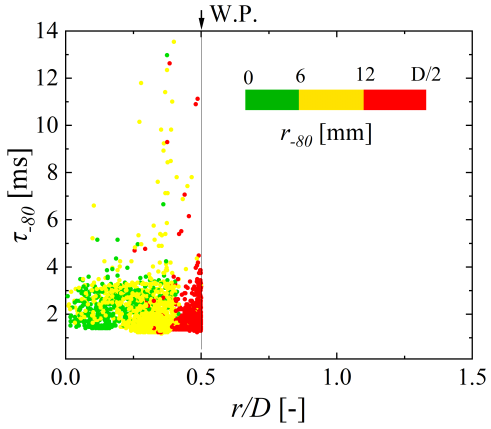

(a) To $x = -40$ mm from $x = -80$ mm

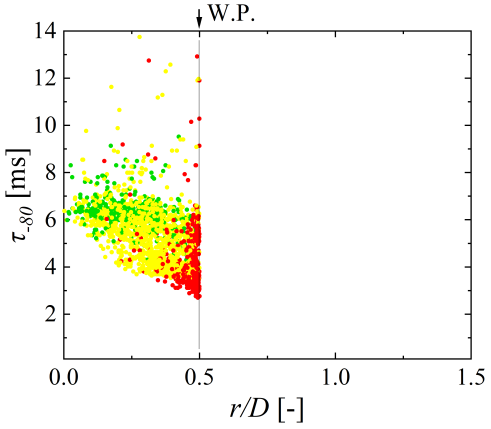

(b) To $x = 0$ mm from $x = -80$ mm

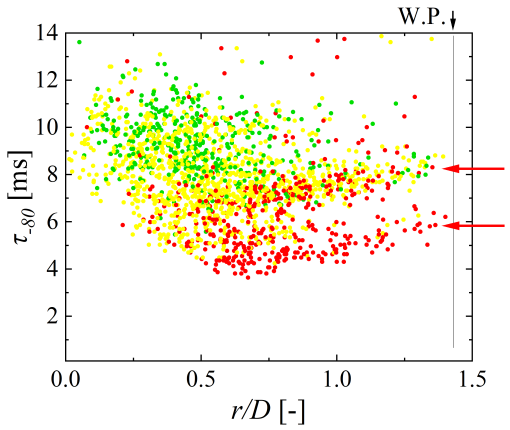

(c) To flame surface from $x = -80$ mm

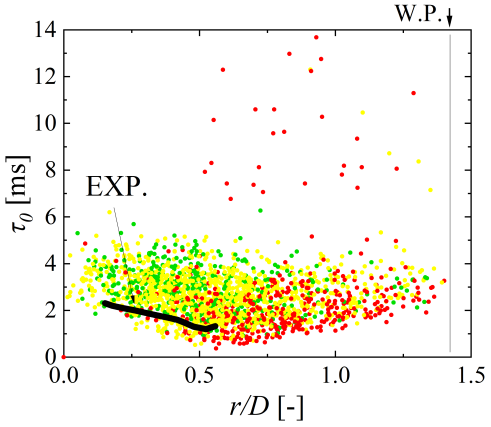

(d) To flame surface from $x = 0$ mm with experimental data [6]

Figure 4.24: Comparison of the scatter plots of delay time, τ, (a) to $x = -40$ mm from $x = -80$ mm, (b) to $x = 0$ mm from $x = -80$ mm, (c) to flame surface from $x = -80$ mm, and (d) to flame surface from $x = 0$ mm with experimental data [6]. The subscript of τ denotes the axial reference position of the delay time, and the radial wall position, W.P., is also depicted with plots. All particles are colored by the initial radial distance from the combustor axis at $x = -80$ mm, r_{-80}.

References

[1] F. Culick, M. Heitor, and J. Whitelaw. *Unsteady combustion*. Springer Science & Business Media, 1996.

[2] M. Zhu, A. Dowling, and K. Bray. Self-excited oscillations in combustors with spray atomizers. *Journal of Engineering for Gas Turbines and Power*, 123:779–786, 2001.

[3] J.-Y. Lee, E. Lubarsky, and B. Zinn. "Slow" active control of combustion instabilities by modification of liquid fuel spray properties. *Proceedings of the Combustion Institute*, 30:1757–1764, 2005.

[4] M. de la Cruz García, E. Mastorakos, and A. Dowling. Investigations on the self-excited oscillations in a kerosene spray flame. *Combustion and Flame*, 156:374–384, 2009.

[5] T. Shoji, S.Tachibana, T. Suzuki, Y. Nakazumi, and T. Yokomori. A new pattern of flame/flow dynamics for lean-premixed, low-swirl hydrogen turbulent jet flames under thermoacoustic instability. *Proceedings of the Combustion Institute*, 38:2835–2843, 2021.

[6] T. Shoji, S.Tachibana, Y. Nakazumi, R. Fujii, J. Masugi, and T. Yokomori. Detailed unsteady dynamics of flame-flow interactions during combustion instability and its transition scenario for lean-premixed low-swirl hydrogen turbulent flames. *Proceedings of the Combustion Institute*, 39:4741–4750, 2022.

[7] K. Moon, Y. Choi, and K. Kim. Experimental investigation of lean-premixed hydrogen combustion instabilities in a can-annular combustion system. *Combustion and Flame*, 235:111697, 2022.

[8] B. Franzelli, E. Riber, L. Gicquel, and T. Poinsot. Large eddy simulation of combustion instabilities in a lean partially premixed swirled flame. *Combustion and Flame*, 159(2):621–637, 2012.

[9] S. Tachibana, K. Saito, T. Yamamoto, M. Makida, T. Kitano, and R. Kurose. Experimental and numerical investigation of thermo-acoustic instability in a liquid-fuel aero-engine combustor at elevated pressure: Validity of large-eddy simulation of spray combustion. *Combustion and Flame*, 162(6):2621–2637, 2015.

[10] T. Kitano, K. Kaneko, R. Kurose, and S. Komori. Large-eddy simulations of gas- and liquid-fueled combustion instabilities in back-step flows. *Combustion and Flame*, 170:63–78, 2016.

[11] J. Li, Y. Xia, A. S. Morgans, and X. Hanc. Numerical prediction of combustion instability limit cycle oscillations for a combustor with a long flame. *Combustion and Flame*, 185:28–43, 2017.

[12] C. Kraus, L. Selle, and T. Poinsot. Coupling heat transfer and large eddy simulation for combustion instability prediction in a swirl burner. *Combustion and Flame*, 191:239–251, 2018.

[13] A. Pillai, J. Nagao, R. Awane, and R. Kurose. Influences of liquid fuel atomization and flow rate fluctuations on spray combustion instabilities in a backward-facing step combustor. *Combustion and Flame*, 220:337–356, 2020.

[14] L. Yuanzhe, L. P. nad W. Zhuopu, A. Wen, and G. Yu. Large eddy simulation of combustion instability in a subcritical hydrogen peroxide/kerosene liquid rocket engine: Intermittency route to period-2 thermoacoustic instability. *Physics of Fluids*, 35, 2023.

[15] R. Cheng, D. Yegian, M. Miyasato, G. Samuelsen, C. Benson, R. Pellizzari, and P. Loftus. Scaling and development of low-swirl burners for low-emission furnaces and boilers. *Proceedings of the Combustion Institute*, 28:1305–1313, 2000.

[16] R. Cheng, D. Littlejohn, P. Strakey, and T. Sidwell. Laboratory investigations of a low-swirl injector with h2 and ch4 at gas turbine conditions. *Proceedings of the Combustion Institute*, 32:3001–3009, 2009.

[17] J.-P. Légier, T. Poinsot, and D. Veynante. Dynamically thickened flame LES model for premixed and non-premixed turbulent combustion. *Proceedings of the summer program*, 157–168, 2000.

[18] F. Charlette, C. Meneveau, and D. Veynante. A power-law flame wrinkling model for LES of premixed turbulent combustion Part I: non-dynamic formulation and initial tests. *Combustion and Flame*, 131(1):159–180, 2002.

[19] P. A. Strakey and G. Eggenspieler. Development and validation of a thickened flame modeling approach for large eddy simulation of premixed combustion. *Journal of Engineering for Gas Turbines and Power*, 132(7):071501, 2010.

[20] F. Proch and A. M. Kempf. Numerical analysis of the Cambridge stratified flame series using artificial thickened flame LES with tabulated premixed flame chemistry. *Combustion and Flame*, 161(10):2627–2646, 2014.

[21] A. Rittler, F. Proch, and A. M. Kempf. LES of the Sydney piloted spray flame series with the PFGM/ATF approach and different sub-filter models. *Combustion and Flame*, 162(4):1575–1598, 2015.

[22] O. Colin, F. Ducros, D. Veynante, and T. Poinsot. A thickened flame model for large eddy simulations of turbulent premixed combustion. *Physics of Fluids*, 12:1843, 2000.

[23] J. A. Miller and C. T. Bowman. Mechanism and modeling of nitrogen chemistry in combustion. *Progress in Energy and Combustion Science*, 15:287–338, 1989.

[24] V. Moureau, C. Bérat, and H. Pitsch. An efficient semi-implicit compressible solver for large-eddy simulations. *Journal of Computational Physics*, 226(2):1256–1270, 2007.

[25] T. Kitano, T. Tsuji, R. Kurose, and S. Komori. Effect of pressure oscillations on flashback characteristics in a turbulent channel flow. *Energy & Fuel*, 29:6815–6822, 2015.

[26] J. Nagao, A. Pillai, T. Shoji, S.Tachibana, T. Yokomori, and R. Kurose. Numerical investigation of wall effects on combustion noise from a lean-premixed hydrogen/air low-swirl flame. *Physics of Fluids*, 35:014109, 2022.

[27] R. Kai, T. Tokuoka, J. Nagao, A. Pillai, and R. Kurose. Les flamelet modeling of hydrogen combustion considering preferential diffusion effect. *International Journal of Hydrogen Energy*, 48:11086–11101, 2023.

[28] F. Williams. *Combustion Theory*. The Benjamin/Cummings Publishing Company, 1985.

[29] A. Ern and V. Giovangigli. *Multicomponent Transport Algorithms*. Springer, 1994.

[30] R. J. Kee, J. A. Miller, and T. H. Jefferson. CHEMKIN: A general-purpose, problem-independent, transportable, FORTRAN chemical kinetics code package. (SAND80-8003), 1980.

[31] P. Moin, K. Squires, W. Cabot, and S. Lee. A dynamic subgrid-scale model for compressible turbulence and scalar transport. *Physics of Fluids*, 3(11):2746–2757, 1991.

[32] C. Pierce and P. Moin. A dynamic model for subgrid-scale variance and dissipation rate of a conserved scalar. *Physics of Fluids*, 10(12):3041–3044, 1998.

[33] A. Pillai, S. Inoue, T. Shoji, S. Tachibana, T. Yokomori, R. Awane, and R. Kurose. Investigation of combustion noise generated by an open lean-premixed h2/air low-swirl flame using the hybrid les/ape-rf framework. *Combustion and Flame*, 245:112360, 2022.

[34] R. Kurose. In-house code FK^3, available at. http://www.tse.me.kyoto-u.ac.jp/members/kurose/link_e.php, 2022. [accessed 15 May 2023].

[35] T. Kawamura, H. Takami, and K. Kuwahara. Computation of high reynolds number flow around a circular cylinder with surface roughness. *Fluid Dynamics Research*, 1:145–162, 1986.

[36] G.-S. Jiang and C.-W. Shu. Efficient implementation of weighted eno schemes. *Journal of Computational Physics*, 126:202–228, 1996.

[37] M. Day, S. Tachibana, J. Bell, M. Lijewski, V. Beckner, and R. Cheng. A combined computational and experimental characterization of lean premixed turbulent low swirl laboratory flames ii. hydrogen flames. *Combustion and Flame*, 162:2148–2165, 2015.

[38] J. Bell, R. Cheng, M. Day, and I. Sheperd. Numerical simulation of lewis number effects on lean premixed turbulent flames. *Proceedings of the Combustion Institute*, 31:1309–1317, 2007.

[39] J. Bell, M. Day, and M. Lijewski. Simulation of nitrogen emissions in a premixed hydrogen flame stabilized on a low swirl burner. *Proceedings of the Combustion Institute*, 34:1173–1182, 2013.

[40] S. Schlimpert, S. Koh, K. Pausch, M. Meinke, and W. Schröder. Analysis of combustion noise of a turbulent premixed slot jet flame. *Combustion and Flame*, 175:292–306, 2017.

[41] R. Rajaram and T. Lieuwen. Acoustic radiation from turbulent premixed flames. *Journal of Fluid Mechanics*, 637:357–385, 2009.

[42] K. Pausch, S. Schlimpert, S. Koh, J. Grimmen, and W. Schröder. The effect of flame thickening on the acoustic emission in turbulent combustion. *22nd AIAA/CEAS Aeroacoustics Conference*, 2016.

[43] Y. Hardalupas and M. Orain. Local measurements of the time-dependent heat release rate and equivalence ratio using chemiluminescent emission from a flame. *Combustion and Flame*, 139:188–207, 2004.

[44] C. Panoutsos, Y. Hardalupas, and A. Taylor. Numerical evaluation of equivalence ratio measurement using OH* and CH* chemiluminescence in premixed and non-premixed methane-air flames. *Combustion and Flame*, 156:273–291, 2009.

[45] P. Therkelsen, J. Portillo, D. Littlejohn, S. Martin, and R. Cheng. Self-induced unstable behaviors of CH4 and H2/CH4 flames in a model combustor with a low-swirl injector. *Combustion and Flame*, 160:307–321, 2013.

Nomenclature

c_p	: Specific heat capacity [J/(K kg)]	θ	: Phase [$\circ$]
D	: Diffusion coefficient [m^2/s]	$\boldsymbol{u}$	: Velocity [m/s]
E	: Efficiency function [-]	Y	: Mass fraction [-]
F	: Flame thickening factor [-]	λ	: Thermal conductivity [W/(m K)]
h	: Enthalpy [J/kg]	ρ	: Density [kg/m^3]
Ω	: flame sensor [-]	$\dot{\omega}$	: Reaction rate [mol/s]
P	: Pressure [Pa]		
q	: Heat release rate [J/s]	**Subscripts**	
R	: Gas constant [J/(K mol)]	*comb*	: Combustion
RI	: Local Rayleigh Index [-]	h	: Enthalpy
$\boldsymbol{\sigma}$	: SGS stress tensor [N/m^2]	k	: Species k
T	: Temperature [K]	t	: Turbulent diffusion

Chapter 5

LES/APE-RF of combustion noise in a low-swirl combustor

5.1 Introduction

In this chapter, the effects of wall surfaces on combustion noise of a lean-hydrogen flame in a low-swirl combustor are investigated.

Among studies on combustion noise, Shoji *et al.* [1] have conducted an experimental study of combustion noise from lean-premixed hydrogen low-swirl flames at the Japan Aerospace Exploration Agency (JAXA). In that study, the combustion noise characteristics of open lifted flames were investigated. The study reported that, in the absence of the wall, the combustion noise spectrum of the flame is characterized by sharp peaks [1]. However, in practical combustion devices, the flame is usually confined and interacts with wall surfaces of the combustion device. Moreover, there is an urgent demand for energy-efficient gas turbine combustors powered by hydrogen combustion (since it is a clean fuel) for the realization of net-zero climate strategies. Such combustors will be downsized to achieve higher power densities, meaning they will be compact, which will increase flame-wall interaction and its influence on the combustion-generated noise. This combustion noise modulation by the wall surface has not yet been thoroughly investigated. This is due to the fact that analyzing combustion noise characteristics with the

wall effects through experiments alone is quite difficult because of limitations in measuring the spatiotemporal variations of physical properties owing to restricted access within experimental setups and the capabilities of the experimental techniques themselves.

On the other hand, in numerical simulations of combustion noise, not only can the detailed flow field be evaluated, but it is also possible to identify which physical phenomenon has a dominant effect on the acoustic field. Recently, the hybrid CFD/CAA approach, which couples Computational Fluid Dynamics (CFD) and Computational Aero-Acoustics (CAA) simulations, is attracting attention for numerically investigating combustion noise [2–4]. Some studies employ Large-eddy Simulation (LES) for CFD and solution of the Acoustic Perturbation Equations for Reacting Flow (APE-RF) in the CAA simulation [5, 6], calling this method the hybrid LES/APE-RF approach. There are some studies that only employ a compressible LES for the combustion noise simulation [7], but the configuration of the combustion system is quite simple such as a 1D propagating flame.

To capture the acoustic perturbations in the far field using only a compressible LES with an acceptable computational cost, it is necessary to deploy a fine mesh in and around the flame region, and a coarser mesh in the far field region, implying that grid stretching needs to be implemented in the far field of the LES domain. However, such grid stretching can easily cause dissipation and dispersion of the propagating acoustic perturbations, thereby severely undermining the accuracy of the acoustics computations. A straightforward way to avoid these issues is to use a fine mesh in the far field regions as well, but this would drastically increase the total number of grid points in the LES domain and this coupled with the small time step size of a compressible LES (dictated by the smallest mesh spacing in the CFL criterion) would make the computational cost exorbitant. Furthermore, to accurately capture the acoustic perturbations and wave propagation over long propagation distances, higher-order spatial and temporal discretization schemes that are almost free of numerical dissipation, dispersion and anisotropy are needed [8]. For these reasons, the use of a compressible LES alone for combustion noise analysis using a large computational domain extending up to the far

field is extremely costly and difficult.

However, the hybrid LES/APE-RF approach mentioned above, is an accurate and computationally efficient alternative in which the turbulent reacting flow field is predicted using LES in a relatively smaller computational domain (containing the acoustic source region) with a fine grid, while the CAA simulation is performed on a coarser grid spanning a larger acoustic domain to simulate acoustic wave propagation all the way up to the far field [5, 6, 9]. As an example of the study employing the hybrid LES/APE-RF approach, Schlimpert *et al.* [10], applying the approach to a slot burner, examined the validity of this approach and the combustion noise characteristics. Furthermore, Pillai and co-investigators studied the combustion noise from a turbulent spray flame [11] and an open lean-premixed hydrogen/air low-swirl flame [9] using the hybrid LES/APE-RF approach. However, no studies have yet clearly formulated the wall boundary conditions using the hybrid LES/APE-RF approach, and the effects of walls on the combustion noise have not been fully examined.

Therefore, the purpose of this study is to apply the hybrid LES/APE-RF approach to a lean-premixed gaseous hydrogen/air low-swirl turbulent jet flame with a wall plate placed beside it and to clarify the effects of the wall on the combustion noise characteristics. Here, the reason only a single wall plate is placed by the flame is to solely investigate the change of the flame fluctuation arising from the wall plate and the accompanying combustion noise modulation by avoiding the coupling between acoustic fluctuations and the flame, which commonly occurs in confined systems and results in thermo-acoustic instabilities. Firstly, the wall boundary conditions pertaining to the APE-RF system are formulated to account for acoustic reflection from the wall. Then, the applicability of the present approach is evaluated by comparing the Sound Pressure Level (SPL) spectra computed using the hybrid LES/APE-RF approach with those measured in the experiments, which have been extended from the original work on the flame without the wall [1] to that with the wall very recently, and the effects of the wall plate on the modulation of combustion-generated noise are investigated in detail. In the discussion, to identify the effect of the wall plate on the combustion noise, almost all

the results of the case with the wall plate are accompanied by those of the open flame configuration without a wall plate.

5.2 Numerical methods

5.2.1 Governing equations (LES)

The Flamelet Generated Manifold (FGM) method is employed as a turbulent combustion model to make the computational cost feasible. The governing equations for the LES with the FGM method are the Favre-filtered conservation equations of mass, momentum, mixture fraction, and progress variable. These equations are solved with the semi-implicit solver proposed by Moureau *et al.* [12].

$$\frac{\partial \overline{\rho}}{\partial t} + \nabla \cdot (\overline{\rho}\widetilde{\boldsymbol{u}}) = 0 \tag{5.1}$$

$$\frac{\partial \overline{\rho}\widetilde{\boldsymbol{u}}}{\partial t} + \nabla \cdot (\overline{\rho}\widetilde{\boldsymbol{u}}\widetilde{\boldsymbol{u}}) = -\nabla \overline{p} + \nabla \cdot \boldsymbol{\tau} \tag{5.2}$$

$$\frac{\partial \overline{\rho}\widetilde{Z}}{\partial t} + \nabla \cdot (\overline{\rho}\widetilde{Z}\widetilde{\boldsymbol{u}}) = \nabla \cdot \overline{\rho} D_Z \nabla \widetilde{Z} + \nabla \cdot \boldsymbol{q}_Z \tag{5.3}$$

$$\frac{\partial \overline{\rho}\widetilde{C}}{\partial t} + \nabla \cdot (\overline{\rho}\widetilde{C}\widetilde{\boldsymbol{u}}) = \nabla \cdot \overline{\rho} D_C \nabla \widetilde{C} + \nabla \cdot \boldsymbol{q}_C + \overline{\rho}\widetilde{\dot{\omega}_c} \tag{5.4}$$

where $\bar{}$ denotes the mean value of the physical quantity within the grid scale for filtered LES and $\tilde{}$ denotes the Favre-filtered values. Z is the mixture fraction of fuel and oxidizer, and C is the progress variable of reaction defined as the sum of the mass fractions of the combustion products ($C = Y_{\mathrm{H_2O}} + Y_{\mathrm{OH}}$). ρ is the density, $\boldsymbol{u}$ is the velocity, and p is the pressure. D_Z and D_C are the diffusion coefficients of the mixture fraction Z and the progress variable of reaction C, respectively, given by $D_Z{=}D_C{=}\lambda/\rho c_p$, assuming the Lewis number is unity. Here λ is the thermal conductivity and c_p is the specific heat capacity. $\boldsymbol{\tau}$ is the SGS stress term, and $\boldsymbol{q}_Z$ and $\boldsymbol{q}_C$ are the SGS terms, obtained by using

the Dynamic Smagorinsky model [13, 14]. Also, $\dot{\omega}_C$ is the reaction rate of C. In the FGM method, physical quantities such as mass fractions of each chemical species at each position and the reaction rate are extracted from a database called Flamelet Library. In the LES with FGM, the reference parameters are the mixture fraction $\widetilde{Z}$, the progress variable of reaction $\widetilde{C}$, and the variance of the progress variable $\widetilde{C''^2}$, which is to account for changes of physical quantities between relatively coarse LES grid resolution. This $\widetilde{C''^2}$ is obtained by the following equation.

$$\widetilde{C''^2} = \alpha \Delta^2 (\nabla \widetilde{C})^2, \tag{5.5}$$

where Δ is the filter width. Also, $\alpha = 0.1$ is the model coefficient, which is given by the previous study [15].

5.2.2 Flamelet library

In the process of Flamelet Library generation, 1D laminar premixed flame propagation of various equivalence ratios ϕ is solved and the obtained flame fragment data is transformed into a 3D space of $\widetilde{Z} - \widetilde{C} - \widetilde{C''^2}$. In this study, 1D calculations were performed for every 0.01 equivalence ratio in the range of $0.27 \leqq \phi \leqq 1.00$. The governing equations for 1D laminar premixed flame propagation are as follows.

$$\frac{d(\rho u)}{dx} = 0, \tag{5.6}$$

$$\rho u \frac{dY_k}{dx} = -\frac{dj_k}{dx} + \dot{m}_k, \tag{5.7}$$

$$\rho u c_p \frac{dT}{dx} = \frac{d}{dx}\left(\lambda \frac{dT}{dx}\right) - \sum_k c_p j_k \frac{dT}{dx} - \sum_k h_k \dot{m}_k, \tag{5.8}$$

where j_k is the diffusion flux of mass and $\dot{m}_k$ is the mass production rate of chemical species k. FlameMaster [16] is used in this 1D flame calculation. The detailed chemical reaction mechanism used in this study is proposed by Miller et al. [17] consisting of 20 chemical species and 73 reaction equations. The number of points in the Flamelet Library is 100 points in the $\widetilde{Z}$ and $\widetilde{C}$ directions and 50 in the $\widetilde{C''^2}$ direction.

5.2.3 Governing equations (APE-RF)

The APE-RF consists of the following continuity, momentum, and energy equations [5, 6].

$$\frac{\partial \rho'}{\partial t} + \nabla \cdot (\rho' \overline{\boldsymbol{u}} + \bar{\rho} \boldsymbol{u}') = q_{c,rf}, \tag{5.9}$$

$$\frac{\partial \boldsymbol{u}'}{\partial t} + \nabla \left(\overline{\boldsymbol{u}} \cdot \boldsymbol{u}' \right) + \nabla \left(\frac{p'}{\bar{\rho}} \right) = \boldsymbol{q}_{m,rf}, \tag{5.10}$$

$$\frac{\partial p'}{\partial t} - \bar{c}^2 \frac{\partial \rho'}{\partial t} = q_{e,rf}. \tag{5.11}$$

Here, ρ is density, $\boldsymbol{u}$ is velocity, and p is pressure, and they are decomposed into temporal mean components ($\bar{\rho}$, $\bar{\boldsymbol{u}}$, $\bar{p}$) and fluctuating components (ρ', $\boldsymbol{u}'$, p'), and $\bar{c}$ is the mean speed of sound. The subscript, rf, stands for the "reacting flow". In the above equations, the acoustic source terms of continuity, momentum, and energy ($q_{c,rf}, \boldsymbol{q}_{m,rf}, q_{e,rf}$) are derived from the quantities acquired from the LES results [5, 6], and expressed as

$$q_{c,rf} = -\nabla \cdot (\rho' \boldsymbol{u}')' \tag{5.12}$$

$$\boldsymbol{q}_{m,rf} = -(\boldsymbol{\omega} \times \boldsymbol{u})' - \nabla k' + \nabla \left(\frac{p - \bar{p}}{\bar{\rho}} \right) - \left(\frac{\nabla p}{\rho} \right)' + \left(\frac{\nabla \cdot \boldsymbol{\tau}}{\rho} \right)' \tag{5.13}$$

$$q_{e,rf} = -\bar{c}^2 \left[\left(\frac{\bar{\rho}}{\rho} + \frac{p - \bar{p}}{\rho \bar{c}^2} \right) \frac{D\rho}{Dt} - \nabla \cdot (\boldsymbol{u} \rho_e) - \boldsymbol{u} \cdot \nabla \bar{\rho} - \frac{D}{Dt} \left(\frac{p - \bar{p}}{\bar{c}^2} \right) \right] \tag{5.14}$$

where $\boldsymbol{\omega}$ is the vorticity vector (i.e., $\boldsymbol{\omega} = \nabla \times \boldsymbol{u}$), k is the turbulent kinetic energy, $\boldsymbol{\tau}$ is the viscous stress tensor, and ρ_e is the excess density [18] defined as:

$$\rho_e = (\rho - \bar{\rho}) - \frac{(p - \bar{p})}{\bar{c}^2} \tag{5.15}$$

The acoustic source terms $q_{c,rf}$, $\boldsymbol{q}_{m,rf}$, and $q_{e,rf}$, and the mean flow quantities, viz. mean density $\bar{\rho}$, mean velocity $\bar{\boldsymbol{u}}$ and mean speed of sound $\bar{c}$ required for solving the system of APE-RF, are computed from the solution of the LES. These quantities are then mapped from the LES grid onto the CAA grid using a trilinear algorithm [5, 11]. The acoustic source term $q_{e,rf}$ of the pressure-density relation in Eq. (5.11), contains various source mechanisms that excite acoustic waves in combustion noise. In Eq. (5.14)

for the source term $q_{e,rf}$, the substantial time derivative of density $D\rho/Dt$ in the first term on the right-hand side, implicitly describes the effects of heat release rate per unit volume, volumetric expansion caused by non-isomolar combustion, species diffusion, heat diffusion and viscous effects [5, 6]. Thus, the acoustic source term $q_{e,rf}$ contains one of the dominant source mechanisms of combustion noise, i.e., the unsteady heat release. Derivation of the APE-RF system is presented in Bui et al. [19], and a detailed discussion of the acoustic source terms and the various source mechanisms contained in them is available in [5, 6, 19]. In this study, all the acoustic source terms, viz. $q_{c,rf}$, $\boldsymbol{q}_{m,rf}$, and $q_{e,rf}$ and all the source mechanisms contained in them are considered.

5.2.4 Wall boundary conditions for APE-RF

For solving the Navier-Stokes equations, simple wall boundary conditions such as the non-slip wall condition are conventionally used and generally found to be sufficient [20–22]. However, these conditions are not directly applicable to a high-order finite-difference scheme usually employed in CAA simulations, and proper handling of wall boundary

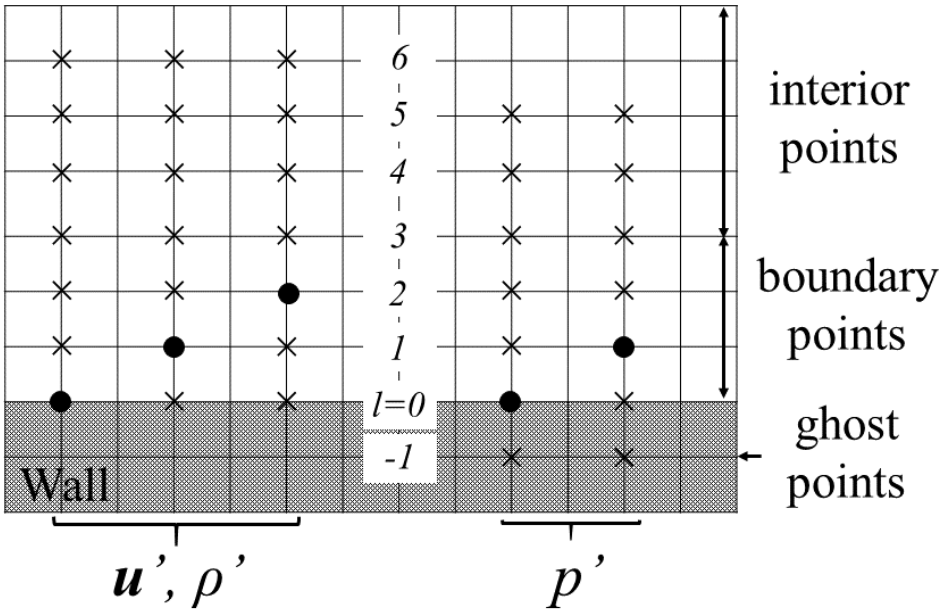

Figure 5.1: Schematic of 7-point stencils for calculation of the spatial difference of perturbation of density, velocity, and pressure using the Ghost points method.

conditions is required. The Ghost points method is an attempt to appropriately describe the wall boundary conditions, such as the reflection of the acoustic wave, by using virtual points inside a wall, which are called ghost points. Note that the values at points inside a wall have no physical meaning, and it is desirable to use as few points as possible to reduce the effect of spurious reflections from a wall. Tam *et al.* [8, 23] proposed a method for imposing appropriate wall boundary conditions in CAA simulations using a single point inside a wall. The schematic diagram of this method is shown in Fig. 5.1. Here, as a high-order finite-difference scheme, the 7-point Dispersion-Relation-Preserving (DRP) scheme [24] is used. To the best of the authors' knowledge, this method has not been implemented in the APE-RF system to consider wall boundary conditions and the resulting acoustic reflections from a wall. Hence, wall boundary conditions pertaining to the APE-RF system are derived below.

Solving the APE-RF system requires the evaluation of spatial derivatives of terms involving perturbation of density, velocity, and pressure. However, in the Ghost points method, the value of the ghost point is used only for the spatial derivative of perturbation pressure. For the calculation of the spatial derivatives of perturbation of velocity and density at three or more grid points away from the wall, the central difference stencil is used. For the boundary points that lie less than three points from the wall (denoted by the full black circles in Fig. 5.1), the calculations are performed using the backward difference stencil that does not include the points inside the wall. The coefficients of the central and backward difference stencils used here are the same as those derived by Tam *et al.* [8, 23]. For the calculation of the derivative of a pressure perturbation term, the backward difference stencil is employed at the point on the wall and one point above the wall (denoted by the full black circles in Fig. 5.1). The difference between the evaluation of a derivative of perturbation pressure and those of derivatives of other terms (i.e., perturbation density and velocity) is whether values at ghost points are used or not. For these calculations, the value of perturbation pressure at the ghost point ($l = -1$) is required; however, the values of ghost points have no physical meaning, so they need to be determined from mathematical relationships to enforce appropriate wall boundary

Table 5.1: Optimized coefficients of central and backward difference stencils for the DRP scheme

$a_{51,5} = 0.048230454,$	$a_{51,4} = -0.28181465,$	$a_{51,3} = 0.768949766,$
$a_{51,2} = -1.388928322,$	$a_{51,1} = 2.147776050,$	$a_{51,0} = -1.084875676,$
$a_{51,-1} = -0.209337622.$		
$a_{60,6} = -0.209337622$	$a_{60,5} = 1.128328861,$	$a_{60,4} = -2.833498741,$
$a_{60,3} = 4.461567104,$	$a_{60,2} = -5.108851915,$	$a_{60,1} = 4.748611401,$
$a_{60,0} = -2.192280339.$		

conditions. The detailed formulation is explained as follows. The conservation equation of perturbation velocity, Eq. (5.10), is discretized using the 7-point DRP scheme, and the equation in the y-direction can be written as

$$\frac{\left(v_0'^{n+1} - v_0'^{n}\right)}{\Delta t} + \frac{1}{\Delta y}\sum_{l=0}^{6} a_{60,l}\left(\bar{u}u_l' + \bar{v}v_l' + \bar{w}w_l'\right) + \frac{1}{\Delta y}\sum_{l=-1}^{5} a_{51,l}\left(\frac{p'}{\bar{\rho}}\right)_l = q_{m,rf,y}. \tag{5.16}$$

Here, u, v, w are speed in each direction and Δy is the grid spacing. l represents the position relative to the wall, and $l = 0$ and $l = -1$ indicate the point just on the wall and the ghost point, respectively. The superscript n represents time steps. The coefficients of various 7-point difference stencils are written as $a_{60,l}$ and $a_{51,l}$, and the subscript of a, such as 60 and 51, refers to the types of backward difference stencils. The detailed coefficient values are available in the other studies [8, 23] and also listed here.

Moreover, supposing that the fluid is viscid, the perturbation velocity $\boldsymbol{u}' = 0$ on the wall surface. By applying these conditions, the value of $p'/\bar{\rho}$ in Eq. (5.16) at the ghost point can be expressed as

$$\left(\frac{p'}{\bar{\rho}}\right)_{-1} = \Big[q_{m,rf,y}\Delta y - \sum_{l=1}^{6} a_{60,l}\left(\bar{u}u_l' + \bar{v}v_l' + \bar{w}w'_l\right) - \sum_{l=0}^{5} a_{51,l}\left(\frac{p'}{\bar{\rho}}\right)_l\Big]/a_{51,-1}. \tag{5.17}$$

The wall boundary conditions for the wall surfaces which are normal to the x- and z-directions can be formulated in a manner similar to Eqs. (5.16) and (5.17).

5.2.5 Domain decomposition method

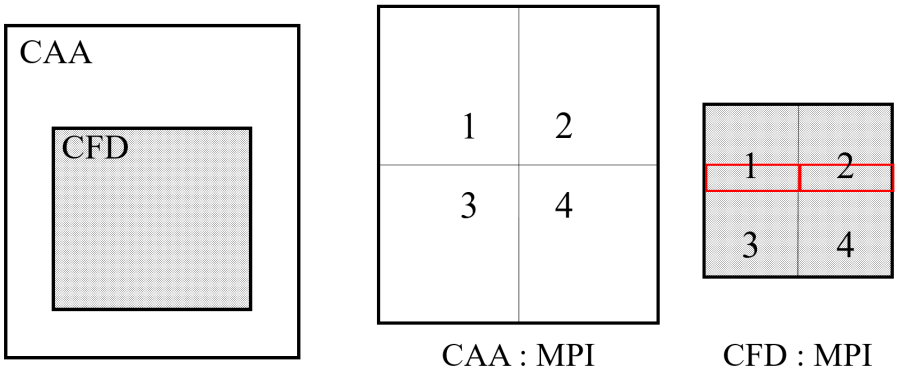

(a) Domain CFD-CAA

(b) MPI-MPI-1

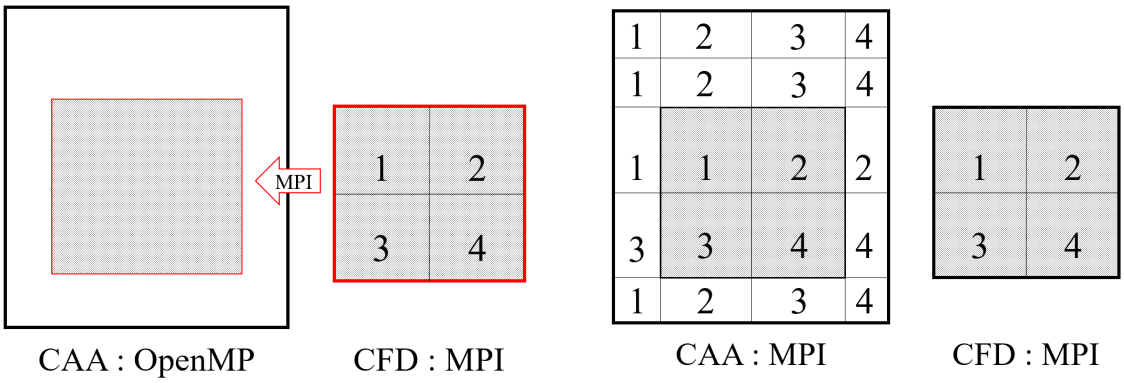

(c) MPI-OpenMP

(d) MPI-MPI-2

Figure 5.2: Schematic of the Domain Decomposition method (DDM) proposed in this study.

In the CFD/CAA approach, there are two individual computational domains for CFD and CAA, and usually, the computational domain of CFD is included in the computational domain of CAA. The conceptual diagram of each domain is shown in Fig. 5.2(a). At each step of the calculation, the acoustic source terms necessary to solve the

acoustic field calculated in the CFD domain must be interpolated into the computational domain of CAA to advance the CAA calculation. Therefore, the interpolation methods of these acoustic source terms and domain decomposition methods for CFD and CAA domains are vital factors that govern the computational speed in parallel computing.

Three domain decomposition methods are compared here. They are named MPI-MPI-1, MPI-OpenMP, and MPI-MPI-2 and shown in Fig. 5.2(b)(c)(d). In this figure, as an example, the domain is decomposed into smaller domains with four processes. The first idea, MPI-MPI-1, is the most simple. Both CFD and CAA domains are decomposed into smaller domains. However, concerning the interpolation of acoustic resources, these values must be sent from the CFD smaller domain to the CAA smaller domain, and when different processes of CFD and CAA cover the same smaller domain, it requires the message passing interface (MPI). Therefore, despite its simple idea, it will be slower and can be intricate in coding. The second one, MPI-OpenMP, tries to solve the complex coding problem. The domain decomposition method for CFD is exactly the same as the one of MPI-MPI-1, but the only single process covers the CAA domain. By doing so, data gathering of acoustic source terms will be simple. However, this method is applicable only when the computational cost of CAA calculation is much smaller than that of CFD. Moreover, there still is an MPI procedure, so it requires some extra time. Last but not least, the method MPI-MPI-2 aims to remove the MPI procedures in the interpolation. In order to do that, the same process must cover the same smaller domain in both CFD and CAA. The domain of CAA covered by CFD domain is decomposed into the same smaller domains of CFD. Usually, the CAA domain is larger than the CFD domain, so the rest of the domain that is yet to be decomposed is allocated to the processes in order. Unlike other methods, each process can have more than one smaller domain in the CAA domain. The drawback of this method is that the coding is complex, and the CAA calculation is inefficient with big parallel computing.

In this study, MPI-MPI-2 is used, and its interpolation speed is 200 times faster than the MPI-OpenMP method.

5.2.6 Computational setup

In the hybrid LES/APE-RF approach, two different domains for the LES and CAA (APE-RF) are necessary [11]. Figure 5.3 shows the computational domains for the LES and CAA (APE-RF). The CAA (APE-RF) domain encompasses the LES domain so that the acoustic field can be analyzed at a farther location. In the experiment, complex components such as a swirler and perforated plates are present upstream of the burner exit [1], but in the LES, only the area downstream of the burner exit is taken into consideration. This assumption could lead to poor reproduction of combustion noise compared with the experimental results, especially at low frequencies [9], but it is necessary to keep the computational cost reasonable. The influence of components upstream of the burner exit is considered through the use of inflow boundary conditions. The boundary conditions are set to have the same mean velocity distribution as in the experiment. In addition to the mean flow, the effect of turbulent fluctuations is considered using a digital filter technique based on Klein *et al.* [25] for pseudo-turbulence generation. The inflow condition is set so that the hydrogen/air unburned premixed gas with a temperature of $T = 300$ K and an equivalent ratio of $\phi = 0.45$ flows into the air. The initial air parameters are set as $T = 300$ K and $p = 0.1$ MPa. The computational domain of the LES extends to 1200 mm $\times$ 750 mm $\times$ 750 mm in each direction of a Cartesian coordinate system, within which the grid consists of 380 $\times$ 430 $\times$ 360 grid points. Moreover, the computational domain of CAA (APE-RF) extends to 800 mm $\times$ 1400 mm $\times$ 1400 mm, within which the grid consists of 300 $\times$ 380 $\times$ 340 grid points. The minimum grid spacings used in the LES grid are $\Delta x = \Delta z = 300$ μm and $\Delta y = 100$ μm. The finest mesh is deployed on the surface of the wall, and the averaged dimensionless wall distance is $\Delta {y_1}^+ \approx 0.66$, and the mesh aspect ratio is three around the wall and unity for the other regions. Concerning the adequacy of the grid size, the integral length scale in the shear layers is of the order of approximately 3 mm, which is calculated in the previous numerical study [9], and the gird spacing around flame and in the shear layers is 300 μmm, so at least ten grid points lie in the integral length scale. The coordinate system sets the x-axis vertically upward and the y- and z-axes horizontally. The center

of the burner exit is set as the origin, and the wall plate with dimensions of 300 mm $\times$ 300 mm $\times$ 5 mm is located at a distance of 29 mm from the origin in the positive y direction. Since no detailed data on wall temperature from the experimental study was obtained, the walls are assumed to be adiabatic and non-permeable, following the study by Pausch *et al.* [26]. This assumption could cause some discrepancies in the numerical simulation results from the experimental results, but judging from the validation results presented in this study, the adiabatic wall assumption seems to be acceptable, at least for the combustion noise analysis. The diameter of the burner exit is set as 35 mm as in the experiment. The non-reflective radiation boundary conditions [27] are applied at the far-field boundaries of the CAA domain, because the APE-RF system does not describe the convection of vorticity and entropy modes [5, 6].

For the LES, the spatial derivative of the convective term in the momentum equation is evaluated with a sixth-order central difference scheme [28] which conserves kinetic energy locally (yields better accuracy for computing turbulent velocity fields), and the WENO scheme [29] is used to estimate those in the transport equations of the scalar quantities because in reacting flows, these scalar quantities undergo sharp jumps across the reaction zones, which resemble to "numerical shocks", so it is necessary to use a numerical scheme capable of appropriately treating such sharp jumps in these scalar quantities encountered in the reacting flow field. For time integration of the convective terms, the third-order Runge–Kutta method is adopted. For APE-RF, spatial derivatives are calculated using the fourth-order DRP scheme [24], and for time integration, the fourth-order alternating Low Dissipation and Low-Dispersion Runge-Kutta scheme in the 5-6 configuration [30] is applied. This DRP scheme is specifically tailored for simulating acoustic perturbations and wave propagation over long distances with minimal dissipation and dispersion.

The LES/APE-RF are performed using the in-house code FK^3-CAA [9, 11, 31, 32], and the simulation time takes approximately 1050 hours in parallel computation using 1024 cores on the CRAY-XC40 supercomputer at the Academic Center for Computing and Media Studies (ACCMS), Kyoto University. In the LES, it takes approximately

0.05 s (simulation time) to generate the initial flow field, following which it takes 0.1 s to calculate the time-averaged quantities, which are needed for CAA simulation, and an additional 0.1 s of the LES/APE-RF simulation (i.e., LES and CAA simulation combined) is conducted for data sampling. The detailed validation of velocity fields using both mean and RMS quantities, and the flame lift of height for the open flame has already been conducted in the previous work [9].

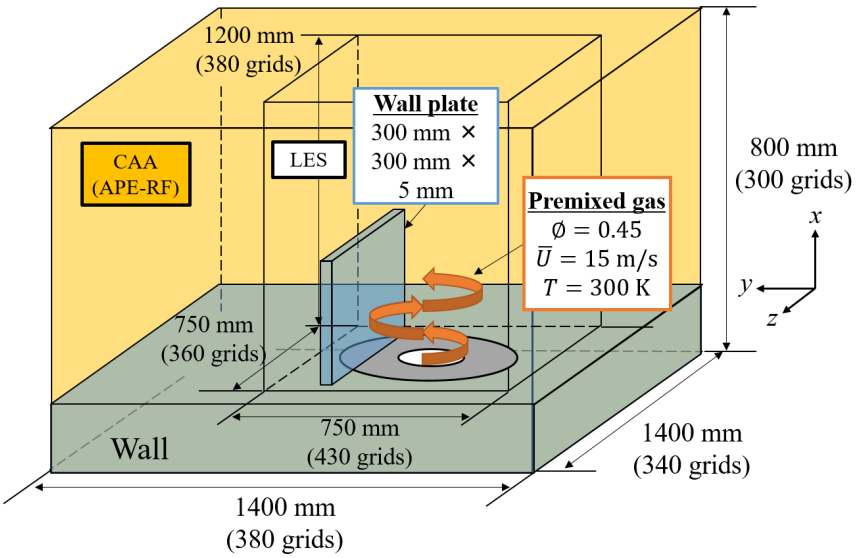

Figure 5.3: Schematic of computational domain and conditions for LES and CAA (APE-RF).

5.3 Results and discussion

5.3.1 Wall plate effect on flame and noise

In order to capture the schematic image of the flame structure obtained by the LES, the three-dimensional isosurface of temperature at 1400 K of the lean-premixed gaseous hydrogen/air low-swirl turbulent jet flame is presented in Fig. 5.4. In the experiment, a lifted flame was observed, which is also reproduced in the LES, judging from the lowest position of the flame. The flame lift-off height predicted by the LES for the case without the wall plate [9, 32] was in acceptably good agreement with the results of Shoji *et al.* [1]. In addition, the flame structure is affected by the presence of the wall and loses its symmetricity in the y-z plane. This asymmetricity is mainly caused by the deformed flow around the wall plate.

Comparison of the velocity field for the case with the wall plate obtained from the LES with that measured in the experiment are presented in the following. Figure 5.5 shows the time-averaged distribution of axial and radial velocity from the experiment and the LES. In the experiment, the flow direction is denoted by the black arrows. As this figure shows, the overall distribution of the velocity field appears to be similar. However, like the case without the wall plate, as compared in the previous work [9], the axial velocity distribution predicted by the LES in the central divergence zone of the swirling hydrogen/air flame has some discrepancy compared with the corresponding experimental data. This discrepancy is attributed to the fact that the turbulent inflow velocity boundary conditions applied at the burner exit in the LES do not completely match with those in the experiment because the complex low-swirl burner geometry situated upstream of the burner exit is excluded from the LES.

Figure 5.6 shows the flame represented by a temperature isosurface at 1400 K and the streamlines of the time-averaged flow velocity for the case without the wall plate and the case with the wall plate. Here, the gas temperature colors the streamlines. The blue curved arrow indicates the swirling direction of the flame. The streamlines in Fig.5.6(a) show that a recirculating flow is formed between the flame and the wall plate.

The swirling motion of the flame drags this strong recirculating flow in the positive z direction, which is then convected downstream as a consequence of being entrained in the mainstream flow of the flame, thereby changing the flame structure drastically in this region. In the case without the wall plate, no recirculating flow is observed around the flame, as shown in Fig.5.6(b), and the flame shape is azimuthally symmetric. Furthermore, when observing the flow temperature (from the velocity streamlines), the temperature becomes high between the flame and the wall plate, and the high-temperature gas flows out to the open region, as shown in Fig. 5.6(a). Consequently, the warmed gas promotes the reaction of the unburnt fuel near the flame base in this region. In order to confirm this phenomenon, the time-averaged temperature distribution in the x-z plane (y = 0 mm) is shown in Fig. 5.7 with the isoline of the heat release rate ($HRR = 8 \times 10^8$ W). In the region where 20 mm $< z <$ 40 mm on this plane of the case with the wall plate, the reaction gets promoted by the swirling hot gas, and the isoline of the heat release rate extends in the negative x-direction around z = 20 mm. On the other hand, around z = -20 mm, the isoline of the heat release rate barely extends in the negative x-direction compared with the distribution around z = 20 mm. Additionally, as Fig. 5.7(b) shows, such a significant extension of the flame to the upstream is hardly observable in the case without the wall plate. Furthermore, to get a rough visual understanding of the acoustic field around such a flame, the instantaneous distribution of perturbation pressure p' must be studied; this distribution is shown in Fig. 5.8. This figure shows that the combustion noise is generated around the flame and propagates roughly spherically from the flame.

Figure 5.9 shows the instantaneous distribution of the perturbation pressure, p' on the $x-y$ plane (z = 0 mm) and the $y-z$ plane (x = 50 mm). As mentioned above, the acoustic wave propagates roughly spherically in the other direction to the wall, but in the direction to the wall, the acoustic wave distribution is deformed. Moreover, judging the figure of the instantaneous distribution of perturbation pressure on the $y-z$ plane, the acoustic wave goes around the wall plate and reaches the back of the wall plate, and the diffraction effect is observed.

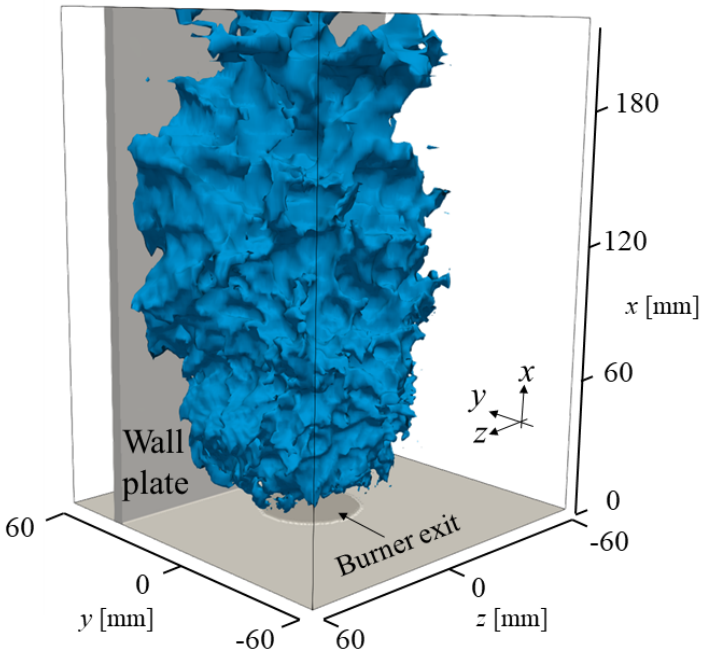

Figure 5.4: Instantaneous distribution of temperature isosurface at 1400 K (colored in blue) from LES/APE-RF.

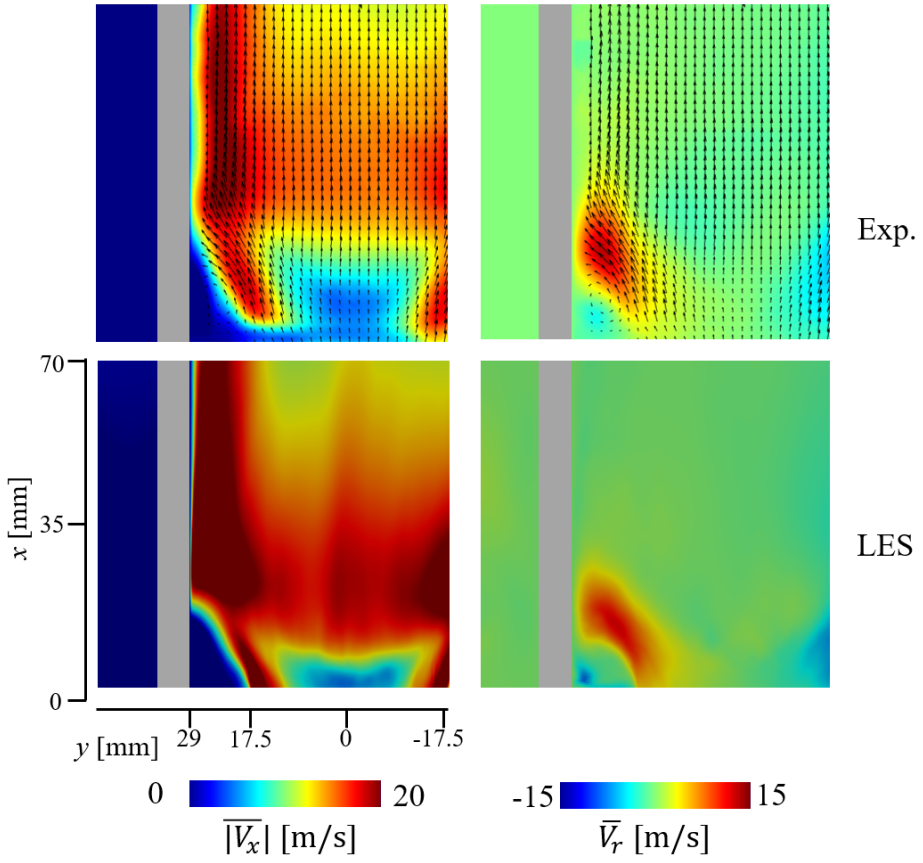

Figure 5.5: Time-averaged distribution of axial and radial velocity, $\bar{V}_x$ and $\bar{V}_r$ from the experiment and LES.

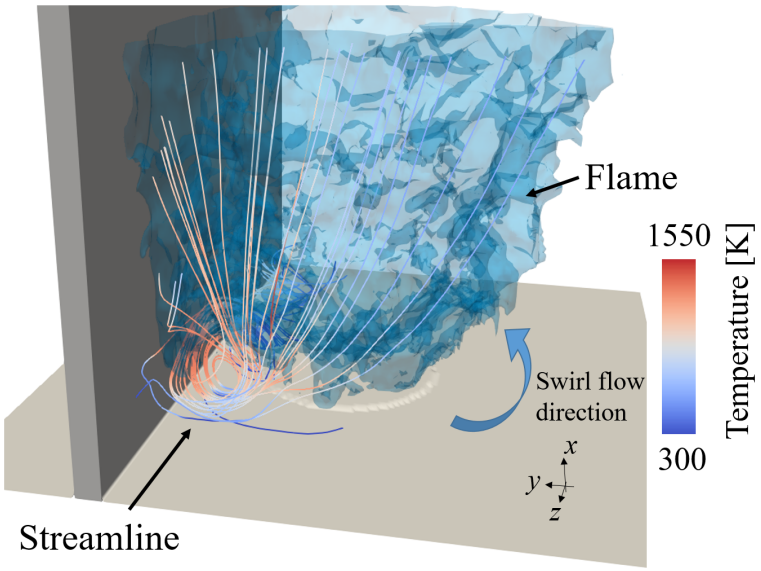

(a) With wall case

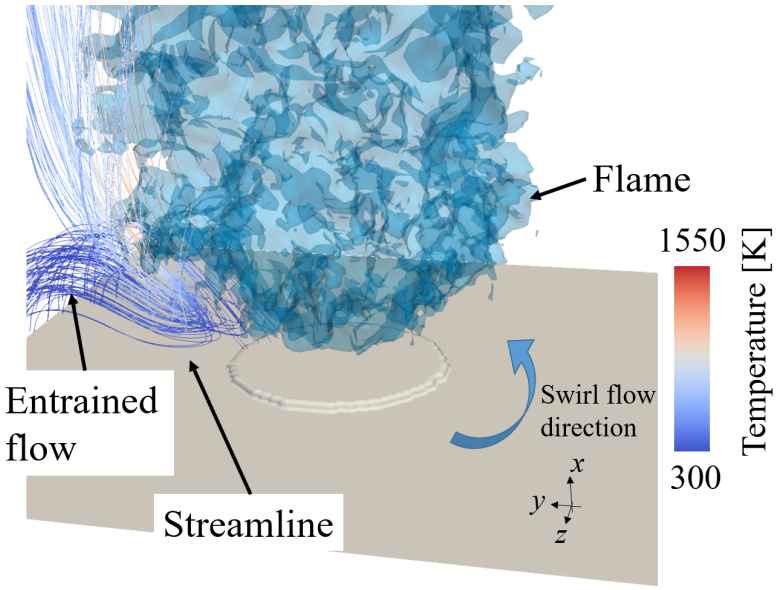

(b) Without wall case

Figure 5.6: Time-averaged streamline distribution (colored by temperature) and instantaneous distribution of temperature isosurface at 1400 K (colored in blue) from LES/APE-RF.

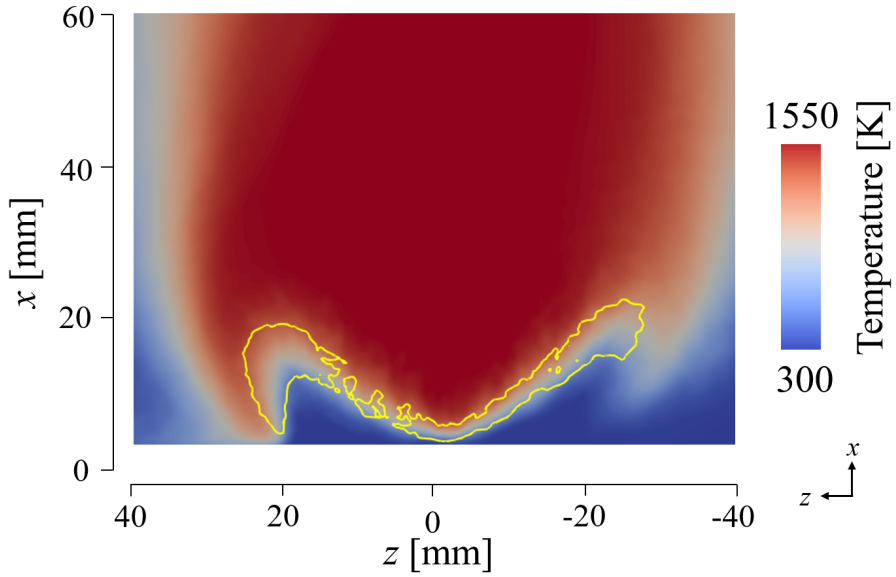

(a) With wall case

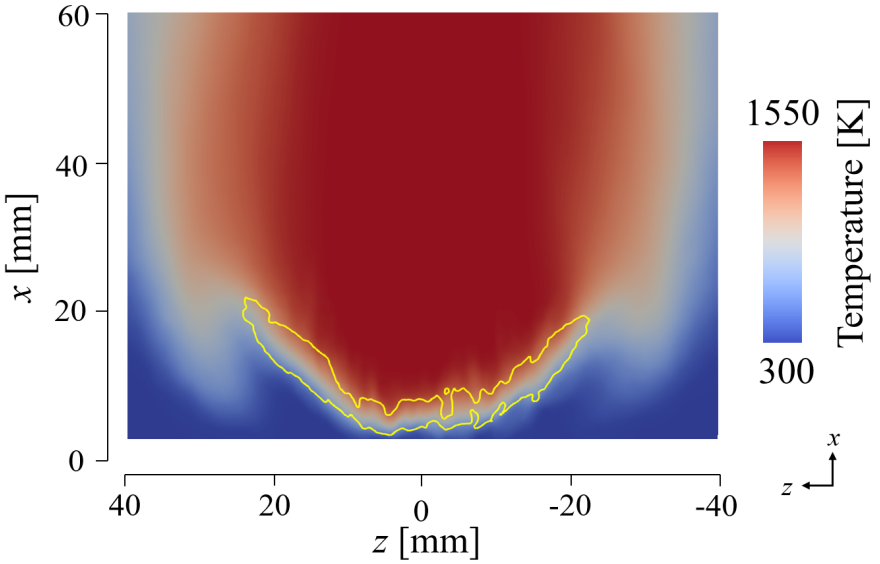

(b) Without wall case

Figure 5.7: Time-averaged streamline distribution (colored by temperature) and instantaneous distribution of temperature isosurface at 1400 K (colored in blue) from LES/APE-RF.

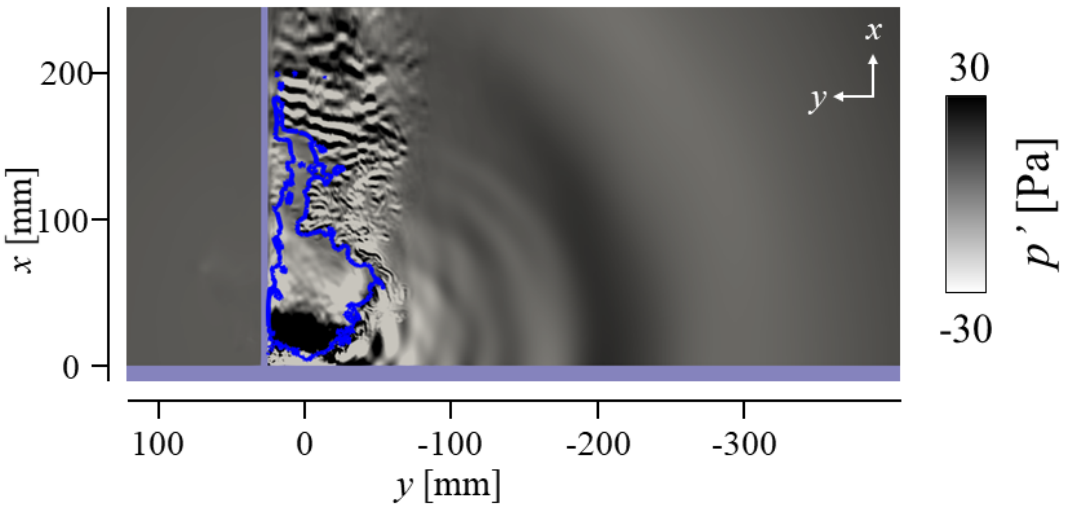

Figure 5.8: Instantaneous distribution of perturbation pressure, p', and temperature isoline at 1400 K (colored in blue) from LES/APE-RF.

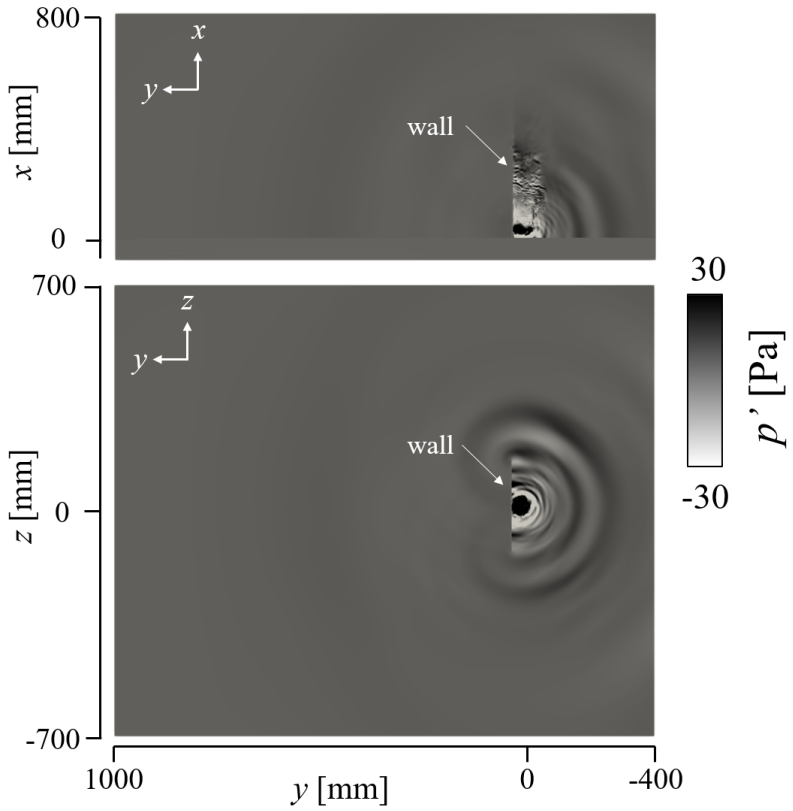

Figure 5.9: Instantaneous distribution of perturbation pressure, p' on $x-y$ plane ($z = 0$ mm) and $y-z$ plane ($x = 50$ mm).

5.3.2 Spectral characteristics of combustion noise

In this section, the effect of placing the wall plate close to the flame on combustion noise is discussed by comparing the SPL spectra obtained from the LES/APE-RF results with the experimental results. Figure 5.10(a) shows the SPL spectra acquired from the LES/APE-RF and experimental measurements at the same position where a microphone is positioned ((x, y, z) = (50 mm, -180 mm, 0 mm)). Here, to consider the effects of the presence of a wall on the SPL, the SPL spectra of both the LES/APE-RF and the experiment without the wall plate are shown in Fig. 5.10(b). In the experiment without the wall plate, a peak in the SPL spectrum was observed at approximately 940 Hz. Although there are some discrepancies in the predicted SPL spectrum, especially in lower frequencies, the LES/APE-RF reproduces the peak reasonably well at approximately 840 Hz. It has been confirmed that this spectral peak is caused by the periodic generation of vortical flame structures in the vicinity of the flame surface in the experiment [1] and the previous LES/APE-RF [9, 32]. Moreover, the discrepancies in the LES/APE-RF results compared to the experimental results are considered to be caused by the lack of detailed modeling of inflow turbulence and the difference in sampling time duration. It is known from the discussion on combustion noise in previous studies [26, 33, 34] that the acoustic mode of the burner or plenum may interact with the flame and influence its dynamics and combustion noise, which can affect the prediction accuracy of the hybrid LES/APE-RF simulation. However, in our experiment, the Low-Swirl Burner (LSB) system, or the entire experimental system for that matter, does not have natural frequencies in the range of the peak frequency (i.e., 940 Hz). Therefore, the acoustic pressure waves at the frequency generated by the flame do not couple with the LSB system's acoustics. Concerning the reproduction accuracy of the combustion noise, the underlying mechanism that generates the peak frequency (840 Hz in the LES and 940 Hz in the experiment) is the same. These peaks are attributed to the periodic flame structure at the shear layer close to the flame which is discussed in the previous study [9]. Hence, even though the prediction accuracy is poor at the lower frequency which could be caused by the effect of exclusion of the inflow region, the discussion of the noise

at peak frequency is valuable in the least. However, in the experiment with the wall plate, the peak that exists in the case without the wall plate is not observed, and the SPL retains a high value from approximately 400 Hz to approximately 800 Hz, which the present LES/APE-RF also reproduces. Thus, while there is some quantitative difference in predicting the SPL frequency distribution, the trends that the SPL peak, which is observed in the case without the wall plate, disappears in the case with the wall plate are qualitatively similar.

Here, whether the sampling time duration to calculate SPL is sufficient for the statistical investigation is confirmed. Figure 5.11 shows the SPL spectra using pressure data of the LES/APE-RF for time intervals of 0.1 s and 0.05 s, which is half of the time interval under each condition with and without a wall plate. This figure shows that the SPL distribution using the pressure data for 0.1 s is almost the same as that with half of the time interval, even though a slight change in the distribution of the SPL is acknowledged for both conditions with the wall plate and without the wall plate. Therefore, the time interval of 0.1 s in the LES/APE-RF is acceptable at least to discuss the effect of the presence of the wall plate on the SPL frequency distribution with several peaks, which has been discussed earlier in this section.

These SPL distributions are significantly impacted by the fluctuation of the heat release rate in a combustion field. The two source elements which primarily affect the SPL are flow fluctuations and heat release rate fluctuations. However, many previous studies have reported that in a combustion noise field around the open flame, the contribution of the fluctuation of the reaction is large enough that the effect of flow fluctuation is almost negligible in the main discussion [5, 6, 10], and the same tendency has been indicated for the combustor in this study as discussed later. Figure 5.12 shows the power spectral density (PSD) of the global heat release rate (obtained from the LES) and the SPL spectrum (obtained from the LES/APE-RF) under both conditions with and without the wall plate. Similar to the SPL spectrum, the PSD of the heat release rate under the condition without the wall plate has a pronounced peak at 840 Hz, where the SPL spectrum also has a peak, indicating that the peak of the SPL spectrum is affected by

the fluctuating phenomena of the heat release rate. The PSD of the heat release rate has high-intensity peaks at 300 Hz and 520 Hz; however, the peaks of the SPL spectrum at these frequencies are much less pronounced than that at 840 Hz even though the PSDs of heat release rate fluctuation at 300 Hz and 520 Hz are bigger than that at 840 Hz, and the reason for this phenomenon is investigated in detail in the next section. Moreover, as shown in the Fig. 5.10(b) in the experiment, that small SPL peak at 300 Hz and 520 Hz is not observed. On the other hand, the PSD of the heat release rate under the condition with the wall plate does not have such a pronounced peak, which is observed under the condition without the wall plate. This trend is the same as that of the SPL frequency distribution with the wall plate, confirming that the SPL distribution is also affected by the heat release rate under the condition with the wall plate. In addition to the above discussion, there are some differences in the qualitative behavior between the spectra of SPL and the PSD of the heat release rate in the high frequency regime for the case with the wall plate, and in the low frequency regime for the case without the wall plate. However, it should also be noted that in this analysis, the spectral distributions of SPL and power spectral density (PSD) of the global heat release rate do not have to match exactly. The fluctuation of the global heat release rate drives the pressure perturbation just around the flame, and this acoustic pressure propagates to the far field. The attenuation of the acoustic pressure does not only rely on global heat release rate fluctuation but also the shape of the flame and the absence or presence of the wall plate.

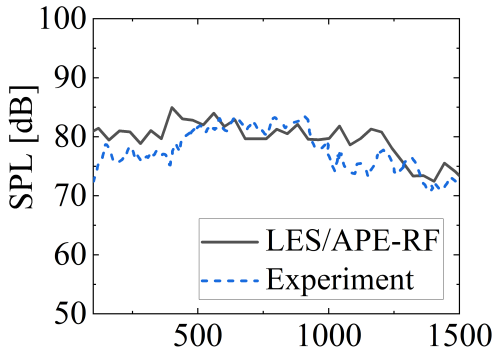

(a) With wall case

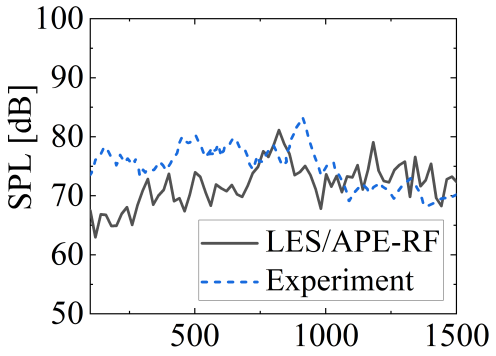

(b) Without wall case

Figure 5.10: Comparisons between LES/APE-RF and experimental [1] Sound Pressure Level (SPL) spectra at the position (x, y, z) = (50 mm, -180 mm, 0 mm), with and without the wall plate.

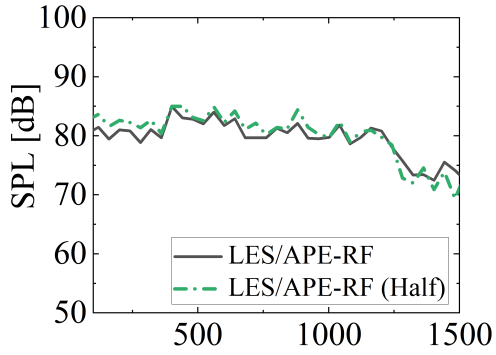

(a) With wall case

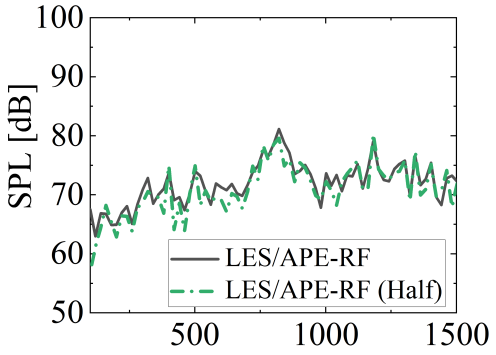

(b) Without wall case

Figure 5.11: Comparisons of Sound Pressure Level (SPL) spectra using data sampled over 2 time intervals (0.1 s and 0.05 s (Half)), with and without the wall plate.

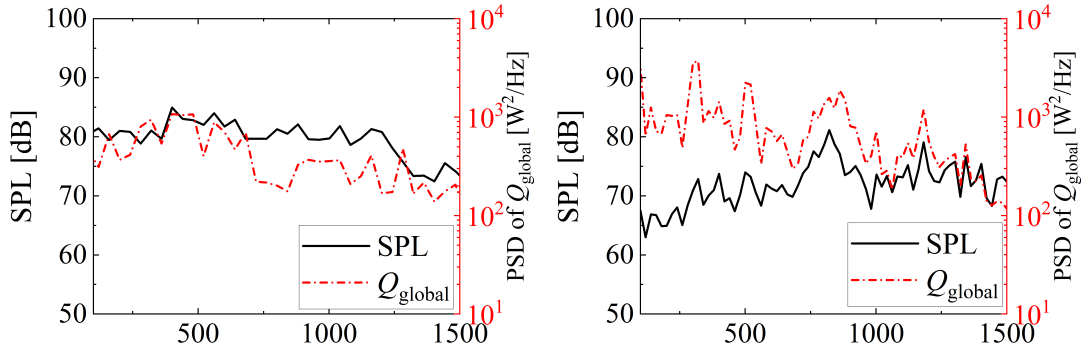

(a) With wall case

(b) Without wall case

Figure 5.12: Comparisons between Sound Pressure Level (SPL) spectra and Power Spectral Density (PSD) of global heat release rate, with and without the wall plate.

5.3.3 Characteristics of propagating sound wave without wall plate

As mentioned in the previous section, the underlying phenomenon that causes the seemingly contradicting results that the PSD of the heat release rate has peaks at 300 Hz and 520 Hz, while the SPL distribution does not have significant peaks at these frequencies under the condition without a wall plate, is investigated. Here, the underlying mechanism is the same among these frequencies; thus, we investigated this phenomenon only at 520 Hz, which has more sampling data. First, to observe the characteristics of sound wave propagation in space in the absence of the wall plate, the SPL radial distributions at the position of $(x, z) = (50 \text{ mm}, 0 \text{ mm})$ at each frequency (520 Hz and 840 Hz) are shown in Fig. 5.13. The position of $y = 0$ mm corresponds to the position of the injector's center axis and flame center. This figure shows that the SPL value steeply decreases from $y = 50$ mm to $y = 100$ mm at both frequencies, and slowly decreases in the $y > 100$ mm region. Moreover, although there is an insignificant difference in the attenuation of the SPL at $y > 100$ mm between frequencies, the SPL at 520 Hz attenuates more steeply than that at 840 Hz in the region from $y = 50$ mm to $y = 100$ mm.

To further investigate the reason for the steep attenuation of the SPL from $y = 50$ mm to $y = 100$ mm, the radial distributions of the time-averaged density and the time-averaged three acoustic source terms $(q_{c,rf}, \boldsymbol{q}_{m,rf}, q_{e,rf})$, which are spatially integrated along the x-direction at each radial position, are shown in Fig. 5.14. All three acoustic source terms have peaks around $y = 25$ mm, and these terms have low values and are almost zero from $y = 50$ mm to $y = 100$ mm, whereas the density changes with a large gradient around $y = 50$ mm. The reason for the peak existence of the acoustic source terms around $y = 25$ mm is owing to the existence of the fluctuating lifted flame surface in the same region. Moreover, the abrupt increase in density around $y = 50$ mm is because there is almost no combustion reaction, and the burned gas and unburned premixed gas are mixed in this region. Thus, the reason for the steep attenuation in SPL from $y = 50$ mm to $y = 100$ mm is that no factor promotes the generation and

propagation of sound waves, and the sound waves are silenced when they pass through the region where it has the high gradient of density. In this figure, the order of magnitude of the acoustic source term, $q_{e,rf}$, which includes the effect of fluctuation of heat release rate, is approximately 10^4 times of the other source terms. This is the reason why only the global heat release rate fluctuation is focused on. Fig. 5.15 shows the attenuation rate of the sound wave to examine the effect of silencing at different frequencies. Here, the attenuation rate is defined as $AT = (SPL_{50} - SPL_{100})/SPL_{50}$, where AT stands for attenuation rate, SPL_{50} represents the SPL value at $y = 50$ mm, and SPL_{100} represents the SPL value at $y = 100$ mm. This figure shows that the attenuation rate is at a minimum at approximately 1000 Hz, and it has a higher value at frequencies lower than 700 Hz. This attenuation rate is considered to be determined by various factors, such as the flame temperature distribution, flame shape, and density distribution, and requires further investigation and data with a long sampling time to be fully clarified. All in all, although the heat release rate fluctuates at 540 Hz, the peak of the SPL at a distance is not so pronounced at the frequency due to the relatively strong silencing effect outside the flame. In addition, the heat release rate fluctuates at 840 Hz, and the SPL peaks at the frequency in a far field because of the relatively weak silencing effect.

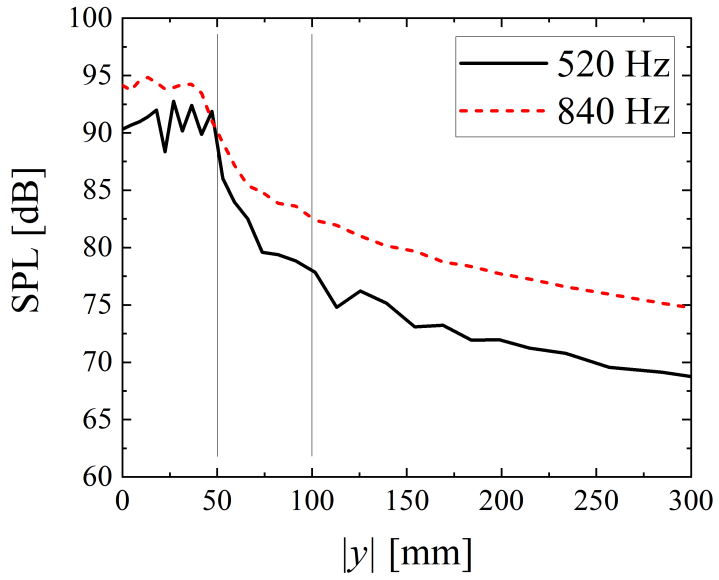

Figure 5.13: Radial distributions of Sound Pressure Level (SPL) at 520 Hz and 840 Hz at $(x, z) = (50 \text{ mm}, 0 \text{ mm})$ without the wall plate.

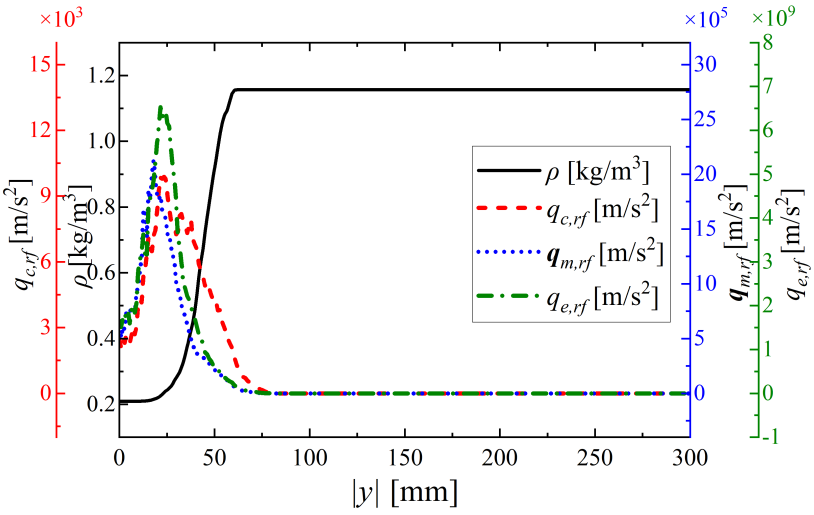

Figure 5.14: Radial distributions of density at each radial position, ρ, and acoustic source terms of continuity, momentum, and energy integrated in the stream-wise direction, $(q_{c,rf}, \boldsymbol{q}_{m,rf}, q_{e,rf})$ without the wall plate.

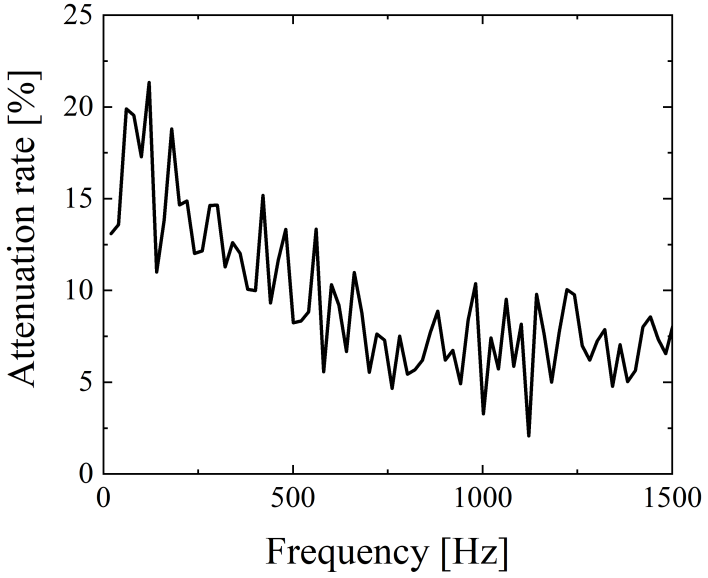

Figure 5.15: Attenuation rate of Sound Pressure Level (SPL) at each frequency without the wall plate.

5.3.4 Characteristics of propagating sound wave with wall plate

The sound silencing effect on the SPL distribution around the flame under the condition with wall plates is also investigated in this section. Figure 5.16 shows the radial distribution of the SPL at 520 Hz and 840 Hz at the position of (x, z) = (50 mm, 0 mm) under the condition with the wall plate. The difference in attenuation from y = 50 mm to y = 100 mm among each frequency is insignificant when the wall plate is present near the flame compared to the case without the wall plate. In addition, Fig. 5.17 shows the attenuation rate at each frequency for the case with the wall plate, which is calculated using the identical definition of the attenuation rate for the case without the wall plate. This figure shows no significant difference in the attenuation rate at each frequency, which is a different trend from the case without the wall plate. This change in the propagation characteristics of sound waves at different frequencies is assumed to be due to the sizeable anisotropic effect of the physical phenomena caused by placing the wall plate near the flame.

First, to comprehend the anisotropicity of the propagating sound waves caused by placing the wall plate, Fig. 5.18 shows the azimuthal SPL distribution at the position of (x, r) = (50 mm, 180 mm). Here, r is the radial distance from the center axis of the injector, and the SPL distributions for two frequencies (520 Hz, 840 Hz) with and without the wall plate are compared. The wall plate position is in a 0-degree direction in this figure. Without the wall plate, the SPLs at the two frequencies are evenly distributed over all azimuthal angles, whereas with the wall plate, the propagation of sound waves behind the wall plate is significantly weaker than at other angles. In addition, the sound waves propagate more strongly in the direction perpendicular to the wall plate (180 degrees) than in the direction parallel to the wall plate (90 degrees and 270 degrees). Specifically, the existence of the wall plate does not only simply change the flame shape but also creates a directionality in the propagation of sound waves, resulting in a less diminutive silencing effect in a specific direction (180 degrees) under the condition with the wall plate than under the condition without the wall plate.

Furthermore, the SPL value is slightly higher in a 270-degree direction than in a

90-degree direction at 840 Hz under the condition with the wall plate. This result indicates that there is anisotropy in the propagation of sound waves even in the parallel direction to the wall plate. It can be presumed that the flame fluctuation's anisotropy affects the sound propagation's anisotropy; thus, the azimuthal distribution of the heat release rate fluctuation should be presented for more discussion. However, the shorter statistical time interval of 0.1 s used in this study than that of 5 s used in the experiment may be insufficient to perform spectral analysis of the local heat release rate to analyze the anisotropic flame fluctuation. Therefore, sufficient data are necessary to acquire a definite correlation between the PSD of the heat release rate and the SPL. For the current situation, it is difficult to conduct such a long simulation owing to the lack of computational resources; this analysis will be conducted in future research.

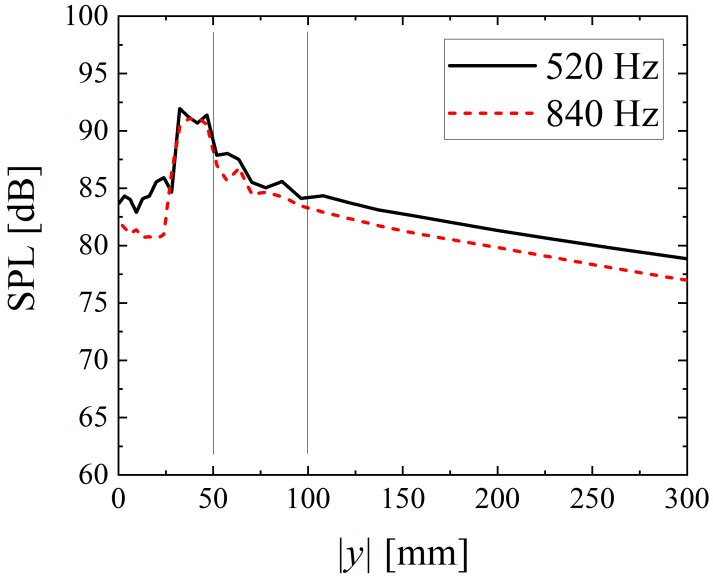

Figure 5.16: Radial distributions of Sound Pressure Level (SPL) at 520 Hz and 840 Hz at $(x, z) = (50 \text{ mm}, 0 \text{ mm})$ with the wall plate in y-negative direction.

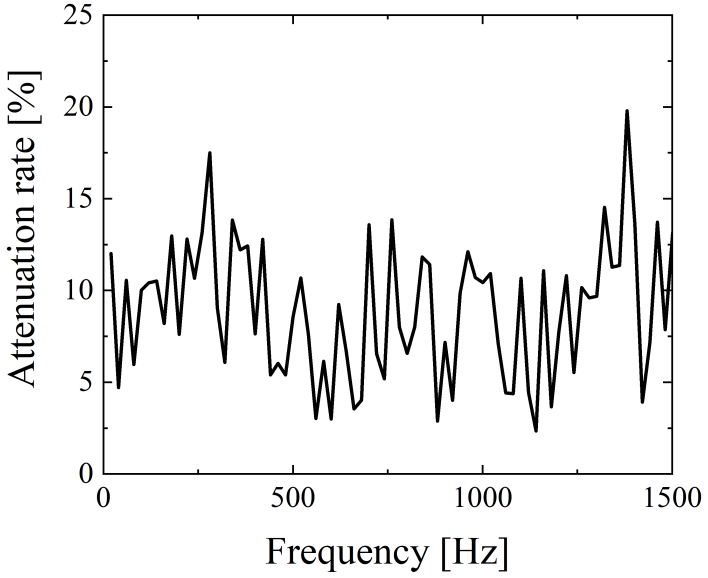

Figure 5.17: Attenuation rate of Sound Pressure Level (SPL) at each frequency with the wall plate.

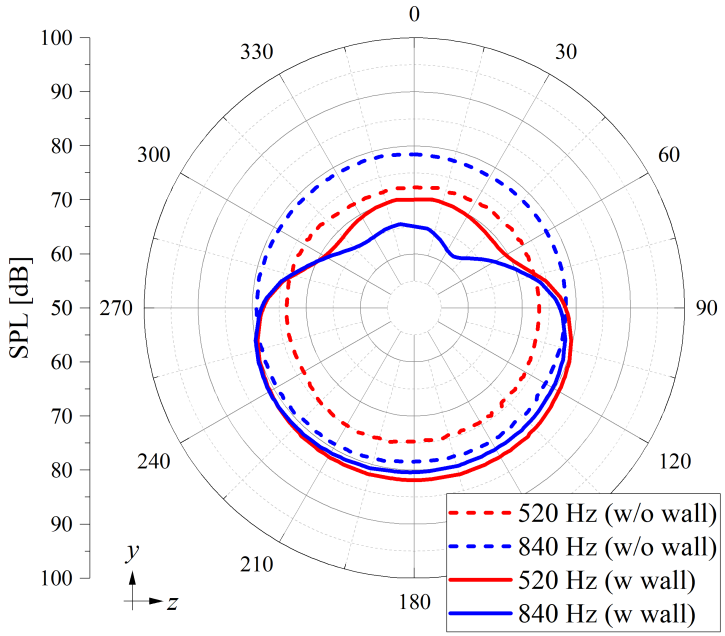

Figure 5.18: Comparison of azimuthal distributions of Sound Pressure Level (SPL) at 520 Hz and 840 Hz with and without the wall plate at the position of $(x, r) = (50$ mm, 180 mm).

5.4 Conclusions

In this study, the hybrid LES/APE-RF approach was used to analyze the combustion noise characteristics of a lean-premixed gaseous hydrogen/air low-swirl turbulent jet flame with a wall plate beside it. The reproductivity of the present approach was evaluated by comparing the Sound Pressure Level (SPL) spectrum computed using the hybrid LES/APE-RF approach with that measured in the experiment. Furthermore, the cause of the changes in the distribution of the SPL was also investigated. Since combustion noise is strongly related to the fluctuation of the heat release rate, the Power Spectral Density (PSD) of the heat release rate within the combustion field was investigated.

The SPL spectrum showed that, although a specific peak was observed in the case without the wall plate, this peak disappeared when the wall plate was placed by the flame, and the SPL became nearly constant within a specific frequency band in both the experiment and the LES/APE-RF. These results verified that the hybrid LES/APE-RF approach adopted in this study could reasonably reproduce the phenomena observed in the experiment, confirming the validity of these methods. Moreover, the absence of a single periodic oscillation of heat release rate in the condition with the wall plate was the main reason for the disappearance of the SPL peaks at specific frequencies. This periodic oscillation was observed without the wall plate but was not prominent with the wall plate due to the inhibition of flame oscillation. This inhibition was caused by the change in flame structure, which is attributed to the interaction of the wall plate with the flow.

Furthermore, the interaction between the wall plate and the flow caused anisotropy in the flame shape and acoustic field. Regarding the acoustic field, sound propagation was weakest behind the wall plate and strongest in the direction where no wall plate exists, which is the other side of the wall plate when viewed from the center of the flame. The results of this study suggested that the anisotropy of the acoustic field was due to the change in the heat release rate oscillation behavior brought about by the change in the flame shape due to the wall plate. However, it was not rigorously proven in this study, and the detailed discussion is a subject for future research, as it requires more

data and is not fully feasible at this time. All in all, the characteristics of the combustion noise at the far field are affected not only by the overall oscillation of the heat release rate of the flame but also by the anisotropic sound propagation.

References

[1] T. Shoji, Y. Iwasaki, K. Kodai, S. Yoshida, S. Tachibana, and T. Yokomori. Effects of flame behaviors on combustion noise from lean-premixed hydrogen low-swirl flames. *AIAA J.*, 58:4505–4521, 2020.

[2] M. Ihme, H. Pitsch, and D. Bodony. Radiation of noise in turbulent non-premixed flames. *Proceedings of the Combustion Institute*, 32:1545–1553, 2009.

[3] M. Ihme and H. Pitsch. On the generation of direct combustion noise in turbulent non-premixed flames. *International Journal of Aeroacoustics*, 11:25–78, 2012.

[4] F. Flemming, A. Sadiki, and J. Janicka. Investigation of combustion noise using a LES/CAA hybrid approach. *Proceedings of the Combustion Institute*, 31:3189–3196, 2007.

[5] T. P. Bui, W. Schröder, and M. Meinke. Numerical analysis of the acoustic field of reacting flows via acoustic perturbation equations. *Computers& Fluids*, 37:1157–1169, 2008.

[6] T. P. Bui, M. Ihme, W. Schröder, and H. Pitsch. Analysis of different sound source formulations to simulate combustion generated noise using a hybrid LES/APE-RF method. *International Journal of Aeroacoustics*, 8:95–124, 2009.

[7] A. Ghani and T. Poinsot. Flame quenching at walls: A source of sound generation. *Flow, Turbulence and Combustion*, 99:173–184, 2017.

[8] C. K. Tam. Computational aeroacoustics: Issues and methods. *AIAA J.*, 33:1788–1796, 1995.

[9] A. Pillai, S. Inoue, T. Shoji, S. Tachibana, T. Yokomori, R. Awane, and R. Kurose. Investigation of combustion noise generated by an open lean-premixed H2/air low-swirl flame using the hybrid LES/APE-RF framework. *Combustion and Flame*, 245:112360, 2022.

[10] S. Schlimpert, S. Koh, K. Pausch, M. Meinke, and W. Schröder. Analysis of combustion noise of a turbulent premixed slot jet flame. *Combustion and Flame*, 175:292–306, 2017.

[11] A. L. Pillai and R. Kurose. Combustion noise analysis of a turbulent spray flame using a hybrid DNS/APE-RF approach. *Combustion and Flame*, 200:168–191, 2019.

[12] V. Moureau, C. Bérat, and H. Pitsch. An efficient semi-implicit compressible solver for large-eddy simulations. *Journal of Computational Physics*, 226(2):1256–1270, 2007.

[13] P. Moin, K. Squires, W. Cabot, and S. Lee. A dynamic subgrid-scale model for compressible turbulence and scalar transport. *Physics of Fluids*, 3(11):2746–2757, 1991.

[14] C. Pierce and P. Moin. A dynamic model for subgrid-scale variance and dissipation rate of a conserved scalar. *Physics of Fluids*, 10(12):3041–3044, 1998.

[15] M. Chrigui, J. Gounder, A. Sadiki, A. R. Masri, and J. Janicka. Partially premixed reacting acetone spray using LES and FGM tabulated chemistry. *Combustion and Flame*, 159:2718–2741, 2012.

[16] H. Pitsch. Flamemaster: A C++ computer program for 0D combustion and 1D laminar flame calculations. Technical report, 1998.

[17] J. A. Miller and C. T. Bowman. Mechanism and modeling of nitrogen chemistry in combustion. *Progress in Energy and Combustion Science*, 15:287–338, 1989.

[18] D. G. Crighton, A. P. Dowling, J. E. Ffowcs Williams, M. Heckl, and F. G. Leppington. *Modern Methods in Analytical Acoustics*. Springer, 1992.

[19] T. P. Bui, W. Schröder, and M. Meinke. Acoustic perturbation equations for reacting flows to compute combustion noise. *International Journal of Aeroacoustics*, 6:335–355, 2007.

[20] T. Kitano, K. Kaneko, R. Kurose, and S. Komori. Large-eddy simulations of gas- and liquid-fueled combustion instabilities in back-step flows. *Combustion and Flame*, 170:63–78, 2016.

[21] A. L. Pillai, J. Nagao, R. Awane, and R. Kurose. Influences of liquid fuel atomization and flow rate fluctuations on spray combustion instabilities in a backward-facing step combustor. *Combustion and Flame*, 220:337–356, 2020.

[22] R. Kai, A. L. Pillai, U. Ahmed, N. Chakraborty, and R. Kurose. Analysis of the evolution of the surface density function during premixed v-shaped flame-wall interaction in a turbulent channel flow at $Re_\tau = 395$. *Combustion Science and Technology*, 1–27, 2022.

[23] C. K. Tam and Z. Dong. Wall boundary conditions for high-order finite-difference schemes in computational aeroacoustics. *Theoretical and Computational Fluid Dynamics*, 6:303–322, 1994.

[24] C. K. W. Tam and J. C. Webb. Dispersion-relation-preserving finite difference schemes for computaional acoustics. *Journal of Computational Physics*, 107:262–281, 2005.

[25] M. Klein, A. Sadiki, and J. Janicka. A digital filter based generation of in flow data for spatially developing direct numerical or large eddy simulations. *Journal of Computational Physics*, 186:652–665, 2003.

[26] K. Pausch, S. Herff, and W. Schröder. Noise sources of an unconfined and a confined swirl burner. *Journal of Sound and Vibration*, 475:115293, 2020.

[27] C. Bogey and C. Bailly. Three-dimensional non-reflective boundary conditions for acoustic simulations: Far field formulation and validation test cases. *Acta Acustica united with Acustica*, 88:463–471, 2002.

[28] Y. Morinishi, T. Lund, O. Vasilyev, and P. Moin. Fully conservative higher order finite difference schemes for incompressible flow. *Journal of Computational Physics*, 143:90–124, 1998.

[29] T. Titarev and E. Toro. WENO schemes based on upwind and centred TVD fluxes. *Computers& Fluids*, 34:705–720, 1993.

[30] F. Q. Hu, M. Y. Hussaini, and J. L. Manthey. Low-dissipation and low-dispersion Runge-Kutta schemes for computational acoustics. *Journal of Computational Physics*, 124:177–191, 1996.

[31] R. Kurose. In-house code FK^3, available at. http://www.tse.me.kyoto-u.ac.jp/members/kurose/link_e.php, 2022. [accessed 15 May 2023].

[32] A. L. Pillai, S. Inoue, T. Shoji, S. Tachibana, T. Yokomori, and R. Kurose. Combustion noise generated by an open lean-premixed low-swirl hydrogen flame: A hybrid CFD/CAA study. 13th Asia-Pacific Conference on Combustion (2021).

[33] S. Herff, K. Pausch, H. Nawroth, S. Schlimpert, C. Paschereit, and W. Schröder. Impact of burner plenum acoustics on the sound emission of a turbulent lean premixed open flame. *International Journal of Spray and Combustion Dynamics*, 12:1756827720956906, 2020.

[34] K. Pausch, S. Herff, F. Zhang, H. Bockhorn, and W. Schröder. Noise sources of lean premixed flames. *Flow, Turbulence and Combustion*, 103:773–796, 2019.

Nomenclature

c	: Sound speed [m/s]	$q_{e,rf}$	: Energy source term [Pa/s]
C	: Progress variable [-]	$q_{c,rf}$	: Continuity source term [kg/(m$^3 \cdot$ s)]
c_p	: Specific heat capacity [J/(K kg)]	$\boldsymbol{q}_{m,rf}$	: Momentum source term [m/s^2]
D	: Diffusion coefficient [m^2/s]	ρ	: Density [kg/m^3]
h	: Specific Enthalpy [J/kg]	T	: Temperature [K]
j	: Diffusion flux of mass [kg/(m^2·s)]	t	: Time [s]
$\dot{m}$	: Mass production rate[kg/s]	$\boldsymbol{\tau}$	: SGS stress [Pa]
$\dot{\omega}$	: Reaction rate [s^{-1}]	$\boldsymbol{u}$	: Velocity [m/s]
p	: Pressure [Pa]	Y	: Mass fraction [-]
Q	: Heat release rate [J/s]	Z	: Mixture fraction [-]

Chapter 6

Conclusions

6.1 Summary and conclusions

This study targeted three topics, namely the combustion instability in the back step combustor, combustion instability in the confined low-swirl combustor, and combustion noise in the unconfined low-swirl combustor. In order to examine the combustion instability behavior in lean combustion with liquid fuel, the equivalent ratio was varied from 0.6, 0.8, to 1.0 in a kerosene-fueled back step combustor, and its effect on the combustion instability was investigated. A numerical simulation was also performed on a hydrogen-fueled low-swirl combustor to study in detail the peculiar oscillation phenomenon that Shoji et al. discovered in this combustion instability [1, 2]. Finally, to examine the effect of wall surfaces alone on combustion noise, a wall was placed near the flame in a hydrogen-fueled low-swirl combustor, which was identical to the combustor of combustion instability described above.

In Chapter 3, which explored the combustion instability in a back step combustor, the amplitude of the pressure oscillation was found to fluctuate temporarily at the equivalence ratio of 0.6, and its tendency was different from that observed under combustion instability, keeping a certain amplitude of pressure oscillation for $\Phi = 0.8$ and 1.0. In order to investigate the time variations of the correlation pressure and heat release rate, a new index "*Time Gap*" was proposed and confirmed as useful. By using *Time Gap*,

it was elucidated that when the phase difference between pressure and heat release rate was decreased, the pressure oscillation was increased, and vice versa.

In Chapter 4, which explored the combustion instability in a low-swirl combustor, it was found that the performed LES, which took the consideration of the complex shape of the swirler, was able to predict the combustion instability observed in the experiment [1, 2], including the unique behaviors, which was first confirmed in the experiment [1, 2]. Moreover, although the pressure oscillations sporadically exhibited temporal declines in amplitude, they were not fully damped and recovered again. Furthermore, a unique behavior, which was first confirmed in the experiment [1, 2], such as the periodic transitions between the inverted conical flame structure and flat flame structure, was similarly observed. The sporadic decay of pressure oscillations appeared when the pressure oscillations and heat release rate fluctuations temporally decoupled. This temporal decoupling was caused by the aperiodic flame transformation; namely, the flame temporally and locally propagated toward the upstream region close to the rim of the injector, which made the flame stable.

In Chapter 5, the combustion noise in a low-swirl combustor was explored. The SPL spectrum without a wall plate had a specific peak, but this peak disappeared when the wall plate was placed by the flame, and the SPL became nearly constant within a specific frequency band in both the experiment and the LES/APE-RF. Moreover, the absence of a single periodic oscillation of heat release rate in the condition with the wall plate was found to be the main reason for the disappearance of the SPL peaks at specific frequencies. This periodic oscillation was observed without the wall plate, but was not prominent with the wall plate due to the inhibition of flame oscillation. This inhibition was caused by the change in flame structure, which was attributed to the interaction of the wall plate with the flow.

6.2 Suggestions for future research

Conducting research into the following areas could extend the progress made in the current study.

1. In Chapter 3, the effects of the equivalence ratio on combustion instability were investigated, and the fuel was injected 5 mm upstream from the back step. In Lean Premixed Prevaporized (LPP) combustion, the fuel will be injected further upstream, and the effect of mixing fluctuation can be more significant than the case targeted in this study, as discussed in Chapter 2. The exploration of this effect will provide beneficial insights into the development of sophisticated LPP combustors. In addition, the effect of sustainable aviation fuel (SAF) on combustion instability is worth noting, considering its probability of usage as a fuel for the achievement of a net zero CO_2 society [3]. Moreover, the detailed process of the atomization of liquid fuel is not considered in this study. However, especially under the condition of combustion instability, the variation of atomization is presumed to affect the fuel consumption [4, 5], and thus, the consideration of the detailed process of the atomization of liquid fuel is also a future plan.

2. In Chapter 4, the combustion instability in the lean-hydrogen low-swirl combustor was investigated. Here, the fuel was lean-hydrogen, so the dynamically thickened flame model used as the combustion model in this study had a possibility of not precisely replicating the preferential diffusion. The preferential diffusion significantly affects the burning velocity, and could eventually affect the flame fluctuation frequency [6]. In order to explore these effects, changing the grid resolution to reduce the effect of the dynamically thickened flame model, employing the adapted mesh refinement not to use the dynamically thickened flame mode, and developing the new dynamically thickened flame model are the options.

3. In Chapter 5, the wall effects on combustion noise in the lean-hydrogen low-swirl combustor were explored. However, due to the lack of computational resources, the

statistical frequency analysis was not employed in the analysis of the local flame region. With much longer computational times, the LES data will make it possible to fully elucidate the effects of local flame fluctuation on the combustion noise in a far field. Moreover, in this study, a single wall plate was deployed near the flame, so the effect of interactions between the flame and several walls was not investigated. Therefore, changing the number, position, size, and shape of the wall plate will be an intriguing parametric study. Furthermore, this study targets the analysis of the direct combustion noise (which is mainly caused by the heat release rate fluctuations), but in a real combustor, indirect combustion noise (which is caused by inhomogeneities of entropy, mixture, and vorticity) can play an important role of noise generation. Hence, exploring the effect of indirect combustion noise will provide invaluable insight into combustion noise analysis.

References

[1] T. Shoji, S.Tachibana, T. Suzuki, Y. Nakazumi, and T. Yokomori. A new pattern of flame/flow dynamics for lean-premixed, low-swirl hydrogen turbulent jet flames under thermoacoustic instability. *Proceedings of the Combustion Institute*, 38:2835–2843, 2021.

[2] T. Shoji, S.Tachibana, Y. Nakazumi, R. Fujii, J. Masugi, and T. Yokomori. Detailed unsteady dynamics of flame-flow interactions during combustion instability and its transition scenario for lean-premixed low-swirl hydrogen turbulent flames. *Proceedings of the Combustion Institute*, 39:4741–4750, 2022.

[3] J. Xing, Z. An, Y. Zhang, and R. Kurose. Reduced reaction mechanisms for sustainable aviation fuel (saf): isoparaffinic alcohol-to-jet synthetic paraffinic kerosene (atj-spk) and its blends with jet a. *Energy and Fuels*, 37:12274–12290, 2023.

[4] J. Wen, Y. Hu, A. Nakanishi, and R. Kurose. Atomization and evaporation process of liquid fuel jets in crossflows: A numerical study using eulerian/lagrangian method. *International Journal of Multiphase Flow*, 129:103331, 2020.

[5] J. Wen, Y. Hu, T. Nishiie, J. Iino, A. Masri, and R. Kurose. A flamelet LES of turbulent dense spray flame using a detailed high-resolution VOF simulation of liquid fuel atomization. *Combustion and Flame*, 237:1117412, 2022.

[6] R. Kai, T. Tokuoka, J. Nagao, A. Pillai, and R. Kurose. LES flamelet modeling of hydrogen combustion considering preferential diffusion effect. *International Journal of Hydrogen Energy*, 48:11086–11101, 2023.